Electrical Characterization of Cluster Devices

A thesis submitted in partial fulfilment
of the requirements for the Degree of

Doctor of Philosophy in Physics
at the
University of Canterbury

by

Abdul Sattar

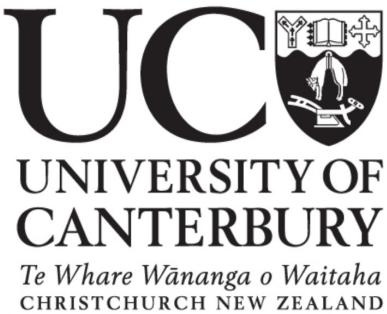

Department of Physics and Astronomy
University of Canterbury
2011

Abstract

The aim of the study presented in this thesis is to explore the electrical and physical properties of films of tin and lead clusters. Understanding the novel conductance properties of cluster films and related phenomenon such as coalescence is important to fabricate any cluster based devices.

Coalescence is an important phenomenon in metallic cluster films. Due to coalescence the morphology of the films changes with time which changes their properties and could lead to failure in cluster devices. Coalescence is studied in Sn and Pb cluster films deposited on Si_3N_4 surfaces using Ultra High Vacuum (UHV) cluster deposition system. The conductance of the overall film is linked to the conductance of the individual necks between clusters by simulations. It is observed that the coalescence process in Sn and Pb films follows a power law in time with an exponent smaller than reported in literature. These results are substantiated by the results from previous experimental and Kinetic Monte Carlo (KMC) simulation studies at UC.

Percolating films of Sn show unique conductance properties. These films are characterized using various electrode configurations, applied voltages and temperatures. The conductance measurements are performed by depositing clusters on prefabricated gold electrodes on top of Si_3N_4 substrates. Sn cluster films exhibit a variety of conductance behaviours during and after the end of deposition. It is observed that the evolution of conductance during the onsets at percolation threshold is dependent on the film morphology. Samples showing difference responses in onset also behave differently after the end of deposition. Therefore all samples were categorized according to their onset behaviour.

After the end of deposition, when a bias voltage is applied, the conductance of Sn films steps up and down between various well-defined conductance levels. It is also observed that in many cases the conductance levels between which these devices jump are close to integral multiples of the conductance quantum. There are many possible explanations for the steps in conductance. One of the explanations is formation and breaking of conducting paths in the cluster films by electric field induced evaporation and electromigration respectively. The stepping behaviour is similar to that in non-volatile memory devices and hence very interesting to explore due to potential applications.

Contents

List of Figures

List of Tables

Chapter 1

Introduction

Since semiconductor transistors replaced bulky vacuum tubes, the size of computers has reduced and their processing power has increased every year. The size of electronic circuitry is reducing due to improvements in fabrication techniques and availability of better tools. This miniaturization trend was first observed by Gordon E. Moore in 1965 [1].

So far technological advancements have been able to keep up with Moore's law [2]. But now chip features are reaching a size as small as 45 nm [3] where both economic and technical limitations are making it impossible to shrink the chips further with current fabrication techniques [4, 5]. The time has arrived where a technological breakthrough is required instead of mere evolution. At the nanometer scale, properties of materials are governed by quantum laws which have to be understood and utilized in order to continue the advancements in microelectronics.

This thesis explores novel electrical properties of cluster[1] films which could ultimately lead us towards fabrication of new devices. Before discussing the details of current work this chapter provides a general introduction to nanotechnology, clusters and cluster films, in order to shine some light on the issues that will be discussed in the rest of the thesis. A layout of thesis giving an overview of the content of each chapter is included at the end.

[1]Note: Term cluster in this thesis refers to cluster of atoms. Clusters are also referred some time as nanoclusters in the literature.

1.1 Nanotechnology

All structures with at least one dimension less than 100 nm can be classified as nanostructures [6] and the technology which deals with such small structures is called nanotechnology. In the latter half of the twentieth century advances in chemical processes like lithography [7, 8] and electron microscopy have made it possible to fabricate devices using nanostructures [9, 10]. With the help of tools like the scanning tunnelling microscope it is even possible to manipulate single atoms [11].

During the ongoing rapid growth of nanotechnology, numerous device fabrication tools and techniques have emerged. In general all these fabrication techniques used in nanotechnology can be divided into two fundamental categories i.e. top down and bottom up. In top down techniques nanostructures are formed out of larger structures. Examples of top down techniques are photolithography, electron beam lithography and focused ion beam lithography. Structures with dimensions down to few nanometers can be formed using top down techniques. In bottom up techniques, atom or molecules are used as building blocks, and structures with dimensions ranging from few nanometer to a few hundred nanometer can be fabricated [12, 13].

So far top-down techniques such as photolithography have been used in the microelectronics industry for Integrated Circuits (IC) fabrication due to high reliability and cost effectiveness. On the other hand, bottom up techniques have been proved useful to fabricate much smaller structures (compared to top-down techniques) with novel properties. However to utilize the unique properties of these structure we need a bridge between the micro and macro world. Therefore bottom up techniques are usually needed to be coupled with top down techniques to produce real world applications.

Photolithography along with di-block copolymer self assembly techniques [14] and templated self assembly of cluster nanowires are examples of combination of top down and bottom up techniques [15]. Clusters with sizes $\sim$ 10 nm could be used as a bridge between top down and bottom up techniques, and are further discussed below.

1.2 Clusters and Nanoparticles

Clusters are aggregates of atoms with a size that can range from a few angstroms to large enough to have bulk properties [16]. Molecules such as proteins can also have thousands of atoms but they are not classified as clusters. Since in general, molecules usually have fixed constitutions whereas cluster can vary in size and composition [17].

Clusters are gaining a lot of interest in the scientific community due to their unique properties. Clusters are interesting because they exhibit quantum behaviour and unique size dependent properties, along with the ease of manipulation. Due to their intermediate size clusters can be considered as a bridge between individual atoms and the micro-world, making them suitable for various nano and microelectronics applications [18]. Clusters have proven a great help understanding finite size effects and quantum phenomenon in fundamental physics.

Examples of size dependent behaviour include:

1) Size dependence of melting point : Due to high surface area to volume ratio the melting point of clusters is different from that of the bulk of same material. Cohesive energy (holding atoms in a cluster) decreases as bigger ratio of atoms reside on the surface compare to the bulk hence resulting in melting point depression [19, 20, 21].

2) Size dependence of T_c : Variations in the critical temperature T_c for transition of conductor to superconductor is another size dependent effect exhibited by clusters. In most cases the T_c decreases with decrease of the cluster size [22, 23, 24] with some exception of aluminium thin films and nanoparticles where T_c increases [25, 26].

As the size of the particles becomes smaller quantum mechanical principles play a more important role in defining the physical properties. With decrease in size the clusters start acting like quantum dots which show variations in band gap and electron localization effects with changes of few Å in their size [27].

In short it can be said that clusters could not only provide a test bench to explore quantum mechanical phenomena but also have many applications in the field of material science, opto-electronics, gas sensing and drug delivery [17].

1.3 Cluster Production

Nanoparticles have been synthesized in colloids since Romans, when glass workers used them for tinting pottery and window glasses [2]. In the past half century, synthesis of nanoparticles and clusters has gain a renewed interest because of their peculiar properties as discussed in the previous section.

Clusters can be produced by various physical and chemical methods [28]. Inert Gas Aggregation (IGA) has various advantages over its counter parts such as liquid chemical based processes. In an IGA source the clusters are produced by a condensation like process in an inert gas environment. Clusters are formed in an inert gas environment and have little risk of contamination compared to that in wet chemical methods [29]. Moreover the size and other properties of clusters can be controlled by varying different readily changeable parameters [30]. Also a high deposition rate and continuous cluster production make the IGA technique promising for applications [31, 30, 18, 32].

The IGA cluster source used during the experiments presented in this thesis is further discussed in Chapter 2. The experiments focus on percolating cluster film properties, such as coalescence and conductance. To understand the behaviour and properties of these films, a brief introduction to percolation theory is given in the following section.

1.4 Percolation Theory

Consider rain drops falling and making small wet spots on the floor. In the beginning each new drop will fall in an empty space and the probability of spots overlapping older spots will be low. However with the passage of time the probability of new drops overlapping old ones will increase as the floor surface becomes more and more covered with wet spots. With the increase in surface coverage the overlapping spots will first start small clumps. These clumps will grow with the surface coverage forming bigger and bigger connected networks. After reaching a certain surface coverage a network is formed extending from one end of the floor to the other. Such networks are called percolating networks and the minimum coverage, above which the probability of forming percolating networks for infinite system is one, is called the percolation threshold. Figure 1.1 shows a 2D square lattice. Here Figure 1.1(a) shows site coverage of 33% which is well below the

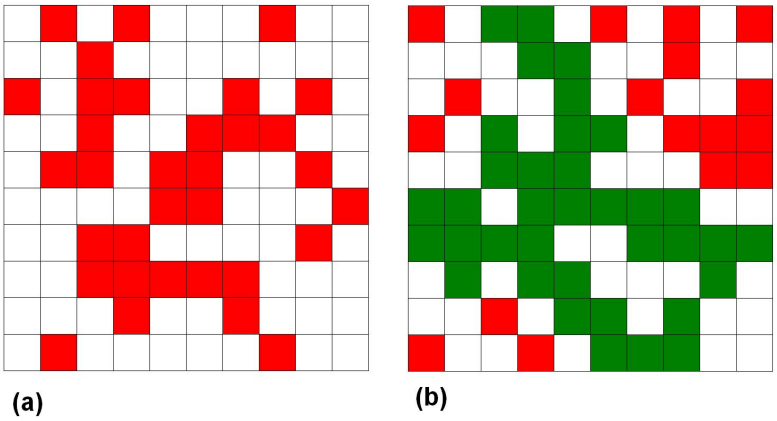

Figure 1.1: (a) Coverage P=33% less than critical percolation threshold P_c (59.3%). (b) Coverage P=63% less than critical percolation threshold P_c (59.3%).

critical percolation threshold P_c for 2D lattice i.e. 59.3%. It is can be seen that occupied cites are grouping together to form small networks. On the other hand Figure 1.1(b) represents a site coverage of 63% which is higher than P_c and we can see networks of occupied cites spanning from one end of lattice to the other. Further details about percolation theory can be found in reference [33].

Percolation theory was first introduced in 1957 by Broadbent and Hammersley. They presented a lattice model to describe fluid flow through a porous material. It was shown that there will be no flow of fluid under certain concentration of the holes in porous materials [34]. In 1972 Kirkpatrick [35] extended percolation theory to describe conduction of random resistor networks. The normalized conductance of these networks was found to be sharply defined and was only dependent on the dimensions of the lattice.

Percolation theory can be applied to wide range of physical systems and is highly relevant to the cluster films discussed in this thesis. The deposition of clusters on a surface between prefabricated electrodes using an IGA source can be understood by the analogy of the rain drops-floor system explained above. Below the percolation threshold incoming clusters only form isolated islands or clumps and such films are not electrically conducting. But above the percolation threshold the cluster films become conducting due to the formation of percolating paths.

1.5 Percolating Cluster Films

Percolating films of clusters are very interesting due to their unusual conductance behaviour and related potential applications such as gas sensors [32, 16]. In the past couple of decades a lot of efforts have been focused on developing gas sensors for various gases[36, 37, 38, 39]. The Resistance of tin cluster films with oxide shell are proven to be dependent on ambient gas concentrations [36]. The resistance of films varies because of the release or trapping of the electrons due to reduction or oxidation process on oxide shell around cluster surfaces. High area to volume ratio of cluster films makes them ideal for the gas sensing applications. Recently at UC the devices fabricated using percolating films of tin oxide clusters have been successfully demonstrated as hydrogen and ammonia gas sensors [40].

Resistance switching behaviour is another interesting phenomenon observed in cluster films [41]. Also in certain cases these cluster films produce Random Telegraphic Noise (RTN) [41]. Previously at UC, Natali [42] and Gourley [41] have observed that the conductance of cluster films shows step-wise variation due applied voltage. This step behaviour is interesting because of its memristor like properties and possible applications (see Section 4.2).

In devices based on cluster films, the interactions between individual clusters are of prime importance. Clusters interact whenever they come into contact with each other. Clusters have a tendency to merge together and form bigger clusters in a process called coalescence. On the other hand nanowire like structures based on these clusters could also disintegrate due to the processes like Rayleigh instability [43]. Studies of these physical properties of clusters would not only increase our basic understanding of these fundamental phenomena but also will pave the path for applying them in real world applications. Study of coalescence in cluster films is further discussed in Chapter 3 which explores the problem by an experimental approach in conjunction with simulations at UC [44, 45].

1.6 Thesis Layout

This thesis aims to explore coalescence and electrical conductance of cluster films. In previous sections an effort has been made to provide basic information about the broad topic of the thesis and to introduce the main research questions that will be dealt with in subsequent chapters. The layout of rest of the thesis is given

below.

To begin, in Chapter 2 information about the equipment and method used during the experiments is provided. Also the details about the substrates, materials, analysis tools and techniques are introduced. Terms and symbols are also defined which will be used in the rest of the thesis.

In the previous section we have briefly discussed the importance of coalescence in cluster films. In Chapter 3 current investigation on coalescence in Sn and Pb percolating cluster films is presented which is an extension of the previous work done on coalescence at UC in recent years. The results are compared to past studies to provide a wider picture.

Chapter 4 explores the electrical properties of Sn cluster films. In the beginning a literature survey about memristors and previous work at UC is provided which is followed by cluster source characterization and experimental results. Over two hundred samples having various film morphologies were investigated. Most of the analysis section focuses on investigations of step-wise changes in conductance and possible explanations of the phenomenon.

Chapter 5 is a continuation of studies of electrical properties explored in the previous chapter. The chapter begins with a review of general transport theory in condensed matter followed by investigations of temperature effects on the conductance of Sn cluster films. The conductance steps discussed in Chapter 4 is also revisited and is analyzed at different temperatures. At the end of the chapter a collective conclusion of Chapter 4 and Chapter 5 is presented to sum up the investigations on conductance of Sn cluster films. Some suggestions for future work are also included at the end.

Chapter 2

Experimental Techniques

This chapter discusses the details of the experimental setup. In the beginning a detailed description of the deposition system is provided. Later sections give description of the substrate preparation and cleaning. This section also contains a brief introduction to the lithographic techniques used for metal contact formation on top of substrates. Subsequent sections contain information about the analysis equipment and techniques such as scanning and transmission electron microscopy. In the end a brief discussion about cluster film coverage measurements and percolation is included.

2.1 Deposition system

During the experiments presented in this thesis the deposition system with a magnetron sputter source was used to deposit tin (Sn) and lead (Pb) clusters. The deposition system also has a facility to mass select and analyze the clusters in situ [30]. A snapshot of this deposition system is shown in Figure 2.1. Clusters formed in the source were carried from the sputter head to the deposition chamber by the argon (Ar) gas flow. These clusters are then deposited on a Si_3N_4 substrate with prefabricated gold (Au) contact pads. The conductance of the cluster film was measured during and after deposition. The diameter of the clusters was controlled by changing source conditions such as gas flow rate, aggregation length and sputter power. The built in mass analyser [46] was used to analyse the cluster size distribution. The vacuum in the deposition chamber was maintained around 10^{-6} Torr during the deposition to avoid oxidation of the metallic clusters produced.

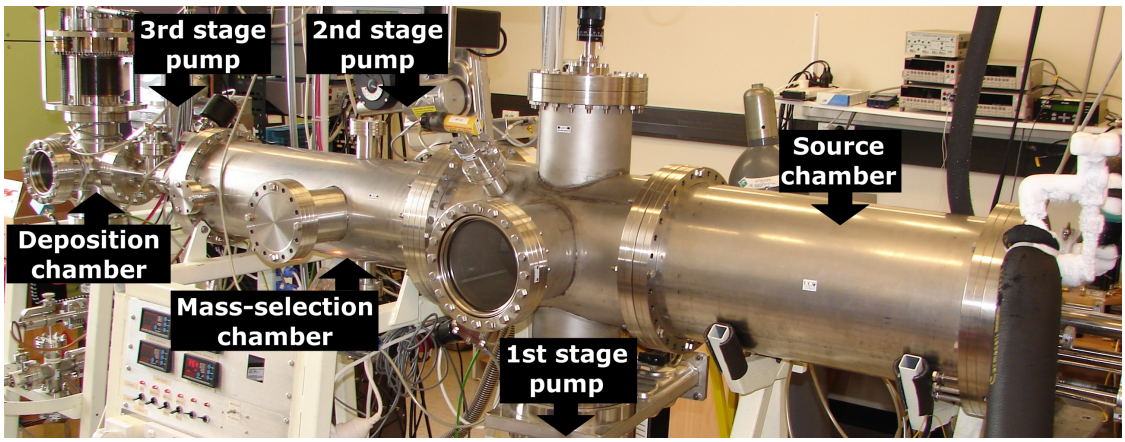

Figure 2.1: An ultra high vacuum compatible cluster deposition system [30].

2.1.1 Vacuum System

All experiments were performed in vacuum conditions with pressures $\sim 10^{-5}$ Torr for the source chamber and $\sim 10^{-6}$ Torr for the deposition chamber. Various types of vacuum pumps, e.g. roots pump, turbo molecular pumps and rotary pumps, were employed for creating a vacuum. A brief introduction to the pumps is given in following sections. In the deposition system, a continuous flow of inert gases like argon and helium is required for the formation of clusters. It is not possible to maintain a good vacuum while having a continuous flow of these gases at ~ 100 sccm [1]. Vacuum system can be divided into three modules each being pumped by a separate pump. The first module is pumped by a roots pump which takes out most of the gas used in source chamber (Section 2.1.2). The second and third modules are pumped by two separate turbo pumps to get rid of any residual gas being carried with the cluster beam or being degassed from the chamber surfaces.

Rotary Pumps

Rotary pumps are used for rough vacuum ($\sim\ 1 \times 10^{-3}$ Torr) and are also used for backing and fore-pumping purposes for the turbo molecular pumps and the roots pumps. Rotary pumps use mechanical techniques to suck gases from the inlet and expel them to the outlet of the pump. Usually the gases are trapped in some cavity formed between a moving part like a gear, piston, lobe, screw or vanes and the static part of the pump. These moving parts then compress the gases and then

[1] sccm: Standard (temperature and pressure) Cubic Centimetre per Minute

throw them to the outlet of the pump. Some of these pumps use oil lubricants to reduce the friction between the moving parts. Such pumps should be used with oil filters at their inlets to minimize any contamination of oil which is back streaming into the vacuum chamber from the pump [47].

Roots Vacuum Pump

Roots pumps are used for pumping large volumes of gas quickly and efficiently and help maintain low to medium quality vacuum. Roots pumps are positive displacement lobe pumps, in which gas is compressed and compelled out due to two-lobe structures rotating at high speed. The structure and the rotation of the lobes generate a low pressure on one side which helps remove the gases out of the chamber and high pressure on the other side which help pushing the gases to the inlet of a backing rotary pump which then pushes these gases out to the atmosphere [47].

Turbo Molecular Pumps

Turbo molecular pumps work using the principal of momentum transfer. These pumps consist of multiple spinning and stationary parts called rotors and stators. Rotors are turbine like blades spinning at high rpm[2]. The gas molecules entering from the inlet collide with the lower face of the rotor's tilted blades and gain momentum. A relatively higher pressure builds up between the rotor and the stator blades due to the relative motion. This pressure value rises between each subsequent stage till it reaches the inlet pressure of a backing rotary pump. Turbo molecular pumps are capable of producing very high vacuum $\sim 10^{-10}$Torr [48].

2.1.2 Source Chamber

The source chamber consists of a magnetron sputter head, a liquid nitrogen cooling system, a nozzle and a skimmer[3] (see Figure 2.2). The magnetron sputter source is discussed in detail in Section 2.1.3.

Ar/He gases are supplied to the back of the source and subsequently flow out of the source chamber through a nozzle which opens into an interconnecting stage

[2]Revolutions Per Minute

[3]A cone shaped nozzle which skims gas accompanied by the particle beam coming out of the nozzle of the source head.

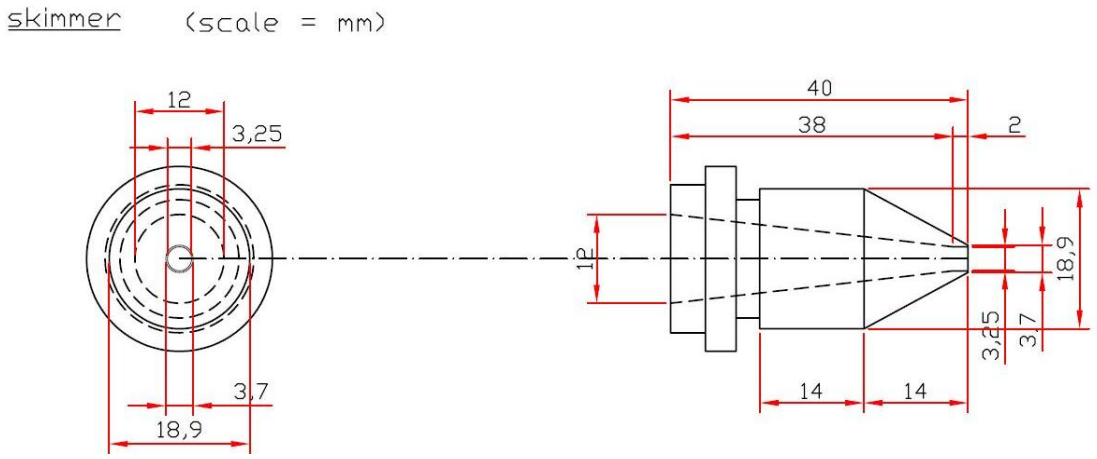

Figure 2.2: A detailed diagram of a skimmer.

between source chamber and the mass selection chamber (see Section 2.1.4). This stage is pumped by a roots pump backed up by a rotary pump (Section 2.1.1). These pumps take most of the gas fed to the system while the clusters coming out of the nozzle with high momentum are able to continue their journey to the mass selection stage through a skimmer [49]. A detailed technical diagram of a skimmer is shown in Figure 2.2. The interconnecting stage between source chamber and mass selection chamber not only helps maintaining good vacuum in the subsequent pumping stages but also helps form a beam of clusters. The beam of clusters travels all the way to substrates in the deposition chamber after traveling a distance of around one metre.

The alignment of the nozzle and the skimmer is of primary importance to carry the good sizes and number of the clusters to the next stage. For alignment there are two control knobs available at the back end of the source chamber which can be rotated in order to move the nozzle in diagonal directions in a plane perpendicular to the skimmer. The source chamber and the nozzle cannot be fixed permanently because of the slight movement due to the cooling effect of liquid nitrogen fed to the cooling jacket around the sputter head. It was observed that any leak during the cooling, only at certain temperature, is an indication of leak in the flexible bellows used for liquid nitrogen transport to the source cooling jacket.

Due to the shape of the nozzle and the pressure difference before and after the nozzle, clusters come out forming a cone shape jet with an axial distribution having heaviest clusters near the axis and the lighter ones spread out. Hence, slightest misalignment can change the net mass going through the skimmer but also can

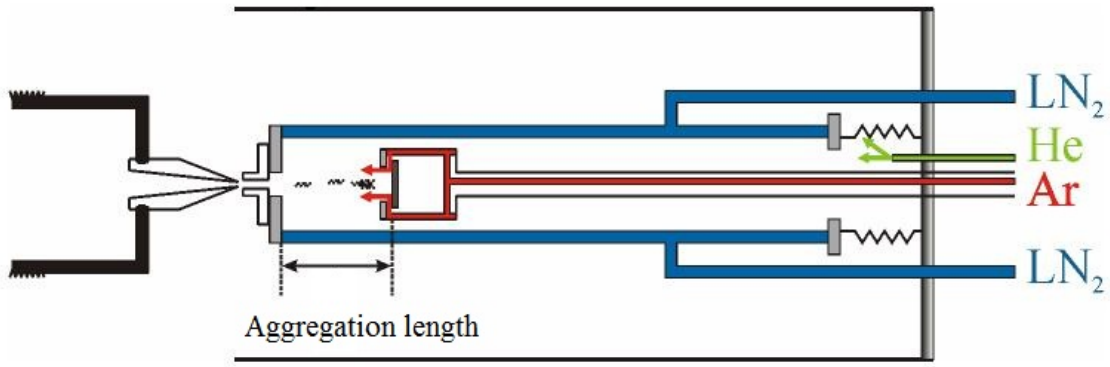

Figure 2.3: A schematic of a magnetron sputter source chamber [53].

affect the size distribution of the clusters. An iris assembly is also available as an alternative to the nozzle whose aperture can be changed from outside the system.

2.1.3 Magnetron Sputter Source

The production of the clusters starts with magnetron sputtering [50] which uses an electric discharge to break down the inert gases in the source chamber. A DC bias is used to produce the plasma near the surface of the metallic target serving as a cathode. The positive ions of inert gas atoms gain velocity in an applied electric field and bombard the target surface due to its negative polarity. A permanent magnet attached on the back of the target produces a magnetic field that traps any secondary electrons produced during the gas ionization due to the original discharge or due to the bombardment of inert gas ions on the surface of the target. These electrons move in helical trajectories near the surface of the target under the influence of the magnetic field and cause more ionization and thus enable plasma creation at lower pressures. This ionic bombardment transfers energy to the surface atoms of the target and cause them to sputter out of the surface if the total energy transferred is more than the binding energy of the atoms [51]. For a surface atom it is three times the surface binding energy and is approximately equal to the heat of sublimation [52]. To avoid melting, the target is cooled down by water running through the copper pipes attached to the back of the target. Liquid nitrogen was also used in the system and the running water prevents freezing of the O-ring on the back of the target head which could lead to a leak in the system.

After these atoms are sputtered into the space between the target and the

nozzle of the source chamber, they start to coalesce and form nanoclusters. The process of coalescence is supported by the momentum transfer to the ambient inert gas/gases which are argon (Ar) and helium (He) in our case. The sputter head is covered by a liquid nitrogen jacket which helps the formation of nanoclusters by cooling the ambient gas. A continuous supply of liquid nitrogen is maintained through a 160 litre liquid nitrogen Dewar attached to the source chamber.

The diameter of the nanoclusters can be varied by changing various parameters of the source chambers including Ar/He ratio, flow rate, aggregation length (see Figure 2.3) and the sputter power. The details of how these factors affect the cluster size distribution are discussed in 4.4.1.

2.1.4 Mass Selection Chamber

A mass selection system is installed in the intermediate pumping stage between source chamber and the deposition chamber. The clusters coming out of the source chamber enter the mass selection chamber via a skimmer of 3.25 mm diameter opening (Figure 2.2). This chamber can be used to analyze the mass distribution of the clusters and can also be used as a mass selection apparatus.

The design is based on the Von Issendorff and Palmer mass filter [54]. The mass selection system consists of four plates parallel to the trajectory of the clusters (see Figure 2.4). The skimmer is aligned with the space between plate 1 and plate 2. Plates 2 and 3 have holes in them to allow passage for the clusters directed in vertical direction by an applied voltage pulse on plate 1.

All ionized clusters gain kinetic energy while they are between plate 1 and plate 2 due to the potential applied on plate 1. The heavier clusters gain less velocity compare to lighter clusters during the first pulse applied between plate 1 and 2. After gaining velocity in vertical direction clusters pass through the holes in plate 2 and enter a field-free region between plate 2 and 3. After moving through the field free region with no acceleration the clusters enter the region between plate 3 and 4 where a second voltage pulse is applied which is equal in magnitude but opposite in sign to the first pulse. The clusters between plate 3 and 4 decelerate due to the applied field and lose their vertical component of velocity gained due to the first pulse.

The resolution of the mass filter depends on the size of the aperture of the exit hole at the end of the mass analyzer, and the selected ion mass depends on the

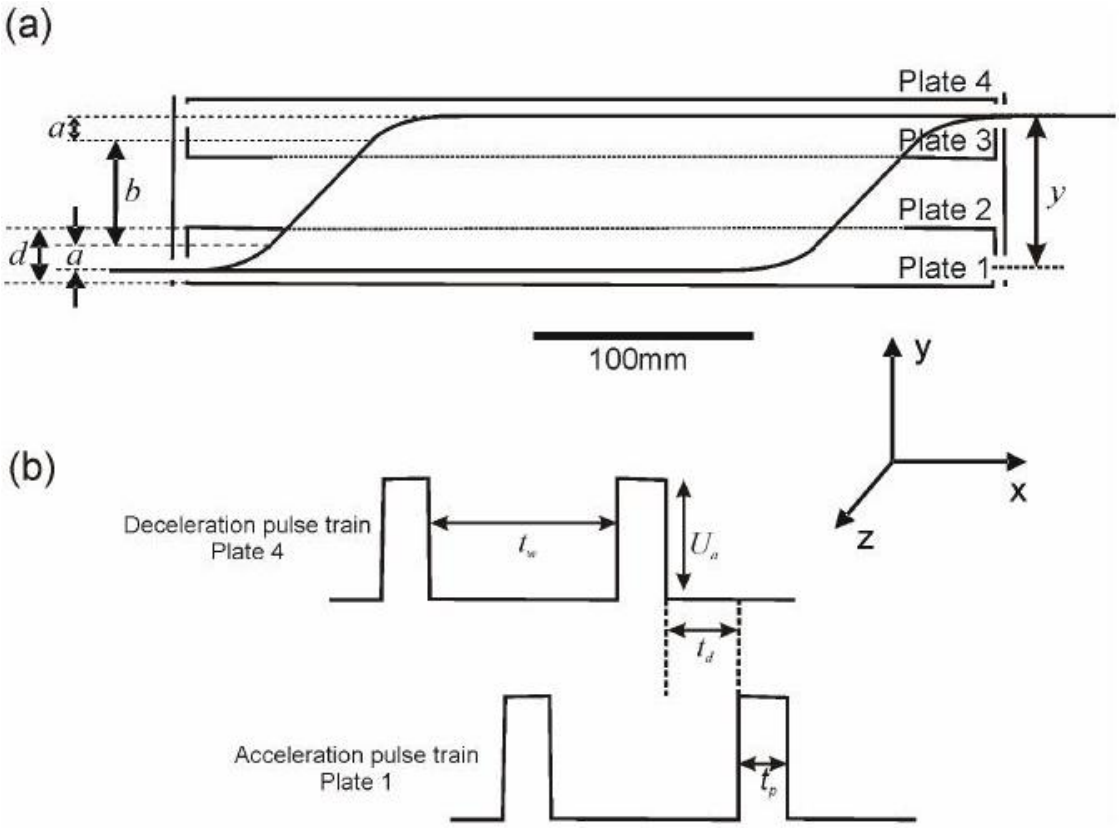

Figure 2.4: (a) Schematic of von Issendorff and Palmer mass filter, where a is the distance covered by the ions with acceleration under the applied voltage U_p and b represent the distance travelled by the ions without acceleration. (b) Applied pulse voltages timing, where t_p is the pulse width and the t_d is the delay between the acceleration pulse and the deceleration pulse [53].

time of flight between the end of the first pulse and the beginning of the second pulse (t_d) and the pulse width (t_p) shown in Figure 2.4. The values t_d and t_p are defined by the following equations:

$$t_p = 2a/\sqrt{2eU_p/m} \tag{2.1}$$

$$t_d = b/\sqrt{2eU_p/m} \tag{2.2}$$

Where a is the lateral distance covered by the ions of mass m during the acceleration under the applied voltage U_p and b is the distance travelled by the ions without acceleration. Further details about the mass analyser can be found in [53].

2.1.5 Deposition Chamber

After passing through the mass selection chamber, the clusters reach the deposition chamber where they are deposited on desired substrates attached to the sample holder (discussed in the next section). The deposition chamber is smaller in volume compared to the mass analyzer and the source chamber and is pumped by a dedicated turbo pump. The smaller volume helps create and maintain a better vacuum. The deposition chamber is equipped with a Sycon Instruments STM-100/FM film thickness monitor (FTM). Also it has a window to allow alignment of the substrate holder and an ionization gauge to monitor the vacuum (Figure 2.5). The substrate holder and cryostat assembly are attached to a flexible coupling on the top of deposition chamber which helps moving the substrate holder in and out of the cluster beam while maintaining ultra high vacuum.

2.1.6 Sample holder

A specialised sample holder with capacity of holding three contacted samples at the same time is attached inside the deposition chamber. Each sample place for holding a sample has ten wires attached to it with flexible pins which act as electrical contacts to the substrate for any in-situ electrical measurements. The sample holders have an integrated cold finger and a heater assembly (explained in Section 2.1.7).

A computer controlled data acquisition system backed by NIDAQ[4] cards and the Lab View graphic user interface is used to record data being generated during

[4]National Instruments Data Acquisition Card

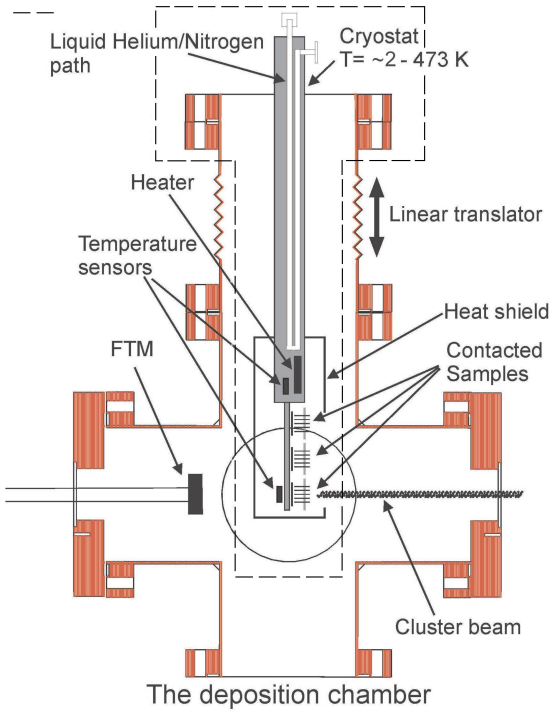

Figure 2.5: A schematic of deposition chamber and sample holder. The attached cryostat/cold finger is shown within the dashed boundary[53].

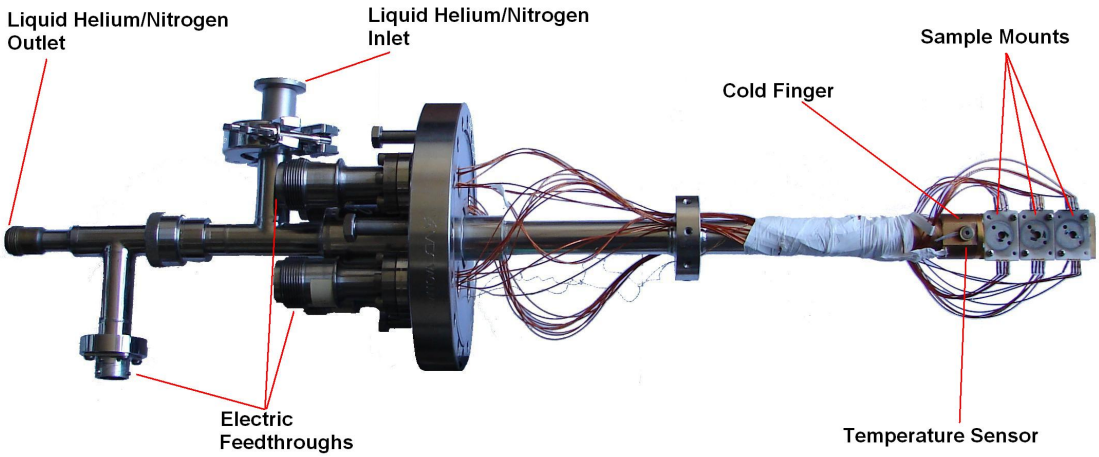

Figure 2.6: A photograph of sample holder.

the experiments. Stable current source, voltage supplies and electrometers make the electronic system capable of producing clean data with a minimum noise. Current, voltage and temperature can be recorded simultaneously [41].

2.1.7 Cryostat

A Janis^{TM}research cryostat, model ST-400 is attached to the deposition chamber chamber as shown in Figure 2.5. The cryostat assembly helps controlling the sample temperature. The cryostat is capable of cooling down the attached samples to a minimum ~ 2 K using liquid helium and heat them up above room temperature using a heater coil attached to the cold finger. To monitor and control the temperature, i.e. maintaining it at certain value or sweeping it up or down, a temperature sensor[5] and a temperature controller[6] is connected to the cryostat cold finger. To cool down the system, a siphon is attached to the cold finger which enables transferring the liquid helium out of the Dewar to the inlet of the cold finger. The outlet of the cold finger is attached to a rotary pump through a gas flow controller valve, which can help reduce the pressure in the finger below atmospheric pressure and hence help further reduce the boiling point of the liquid Helium. The pressure in the cold finger can be controlled by controlling the total in-flux and out-flux of the liquid helium. The influx is controlled by a needle valve attached to the transfer tube and the outflow is controlled by the gas flow controller valve attached to the outlet of the cold finger. A schematic of cold finger and the cryostat assembly is shown in the Figure 2.7.

2.2 Materials

Disk shaped targets with diameter of 50 mm and 6 mm thickness were used in the sputter source. The target consisted of 99.999% pure tin/lead with a polished surface. Figure 2.8 shows the Sn target used in the experiments, a ring like sputtered area is clearly visible. Tin and lead were used as sputter target to produce clusters in the experiments. A brief introduction to these metals is given the following text.

[5]Lakeshore DT-670B-SD diode temperature sensor
[6]Cryogenic Control Systems Inc. model 32

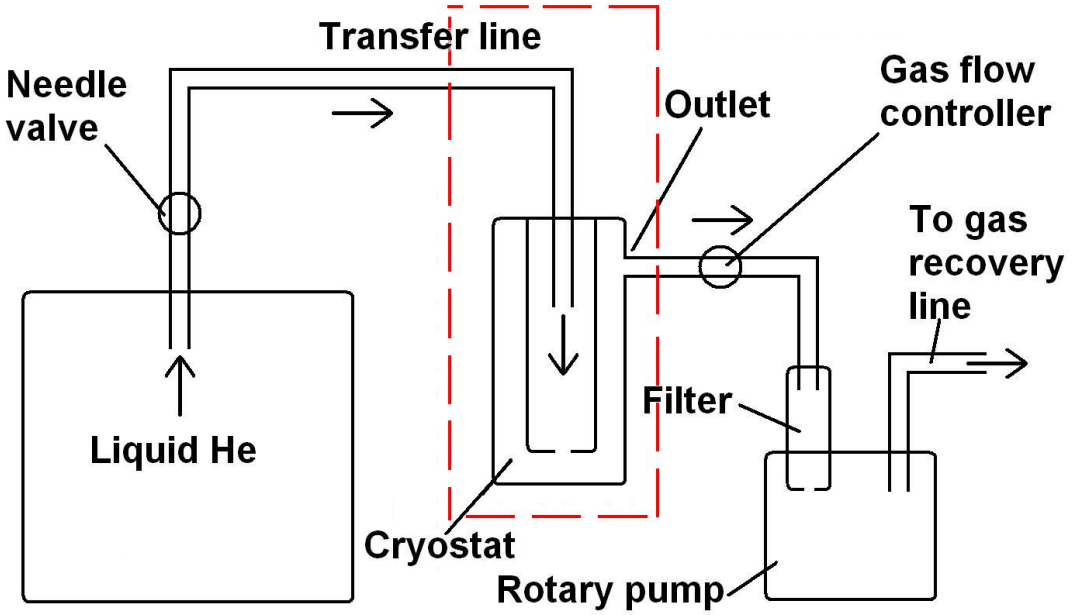

Figure 2.7: A schematic diagram of cryostat assembly (not to scale). Cryostat/cold finger is shown within the dashed boundary. Rest of the assembly is connected externally to the deposition chamber via LHe transfer lines. [53].

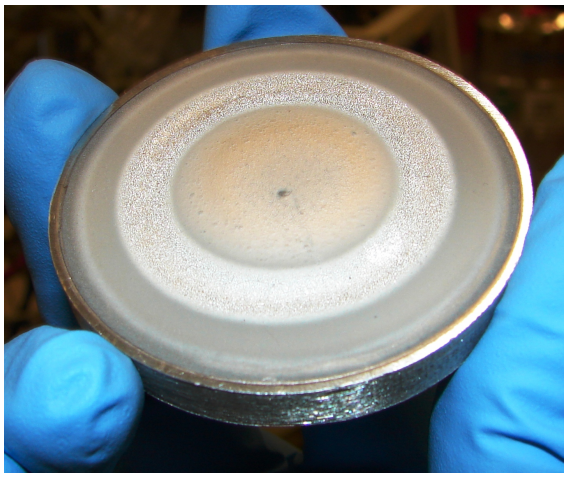

Figure 2.8: A 99.999% pure Tin (Sn) sputter target. A similar target was used for Pb.

2.2.1 Tin (Sn)

Tin is a group 14 element with atomic number 50. Sn is a malleable metal with two oxidation states of Sn^{2+} (less stable) and Sn^{4+} (more stable). In nature, Sn occurs in the form of SnO_2 in the mineral cassiterite. Sn has two allotropes i.e. α-tin and β-tin which are also known as gray and white tin. α-tin is stable below 286.3 K at atmospheric pressure. α-Sn is a zero band-gap semiconductor having diamond structure whereas β-tin is metallic in nature and is stable above 286.3K at atmospheric pressure [55]. Sn has been historically used to make bronze, an alloy of tin and copper. Due to much slower oxidation compared to Fe, tin is widely used in modern industry as a protective coating to avoid corrosion. Also Sn is commonly used in soldering as an alloy with lead. Selected physical and chemical properties of tin are shown in Table 2.1.

2.2.2 Lead (Pb)

Lead (Pb [7]) atomic number 82 is a soft and dense poor metal. Lead is widely used in various applications such as lead acid batteries, radiation shields and bullets. Lead has 4 stable isotopes i.e. Pb^{204}, Pb^{206}, Pb^{207}, Pb^{208}. Lead is a poisonous metal consider a health hazard and can cause nerve damage on ingestion [56]. Some of the selected properties of lead are shown in table 2.1.

2.3 Substrates

To study the electrical properties, the nanoclusters produced in the source chamber were deposited on a substrate. Nitride passivated Silicon substrates with dimen-

Property	Tin	Lead
Standard atomic weight	118.710 g.mol^{-1}	207.2 g.mol^{-1}
Electron configuration	[Kr] $4d^{10}$ $5s^2$ $5p^2$	[Xe] $4f^{14}$ $5d^{10}$ $6s^2$ $6p^2$
Resistivity	106 nΩm	190 nΩm
Density (at $\sim$ 293K)	7.365 g.cm^{-3}	11.34 g.cm^{-3}
Melting point	505.08 K	600.61 K

Table 2.1: Selected physical and chemical properties of Sn and Pb.

[7] Pb is symbol for lead and is abbreviation of Latin word Plumbum for lead

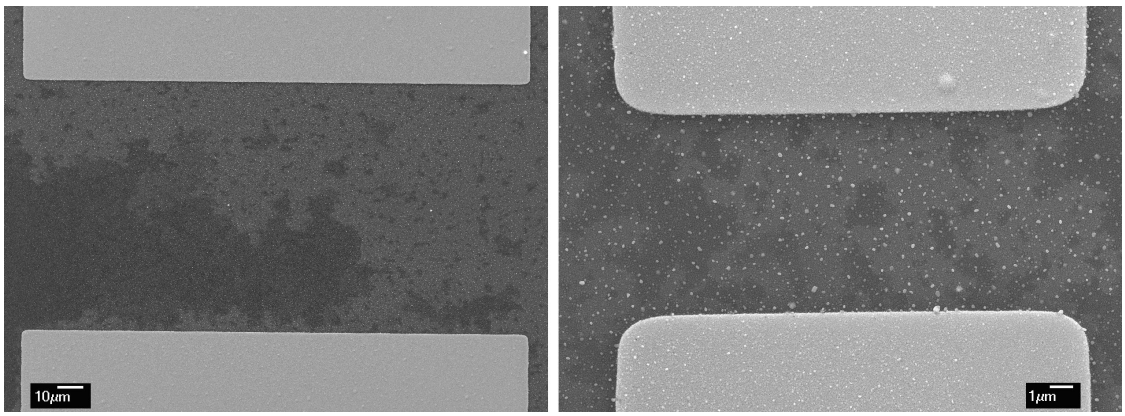

Figure 2.9: Samples with lithographically defined electrical contacts: (a) L1 type sample with electrode dimensions 100×200 μm.(b) L1 type sample with electrode dimensions 10×20 μm.

sions of 10×10 mm were used, see Figure 2.10(b). Samples with 200 nm and 100 nm passivation layer were used. To measure the conductivity of the cluster films gold contacts were formed using an evaporator (Edwards Auto306), details are discussed in the following sections. A 45nm thick electrode layer was formed of gold (Au) (99.99%). To increase the adhesion of the gold layer with Si_3N_4 surface a 5nm thick nichrome[8] (99.5%) layer was deposited prior to the gold layer deposition.

To investigate the electrical properties of the cluster films, electrodes with various aspect ratios and dimensions were formed using metallic mask and lithographical techniques.

Following type of substrate were used for electrical measurements:

1. Samples prepared with shadow masking having electrodes with 100×200 μm gap i.e. Simple samples (SS) (see Figure 2.10(b))

2. Lithographically defined samples i.e.

   - Samples having electrodes with 100×200 μm gap (L1) (see Figure 2.9(a))
   - Samples having electrodes with 10×20 μm gap (L2) (see Figure 2.9(b))

Preparation methods for these samples are discussed in subsequent sections.

[8] A nickel (Ni) and chromium (Cr) alloy

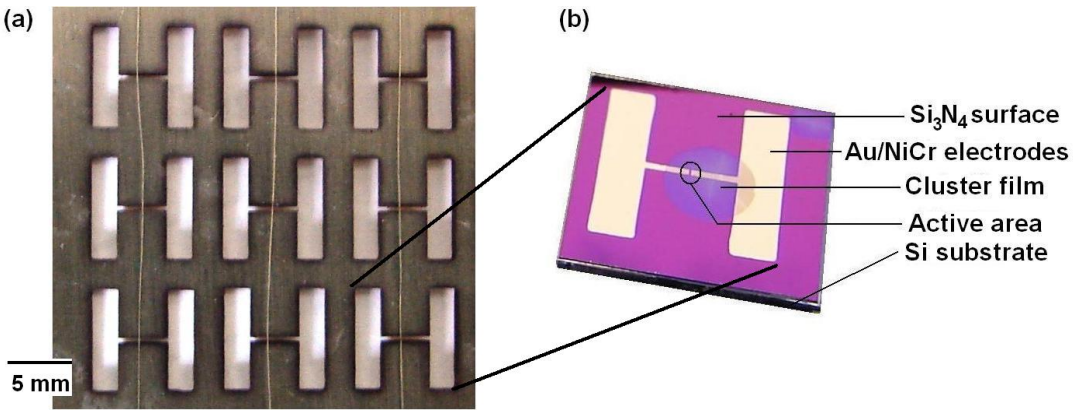

Figure 2.10: a) A shadow mask used for preparing a batch of sixteen simple samples. b) A $10 \times 10mm$ Si/Si_3N_4 substrate with Au/NiCr electrodes.

2.3.1 Shadow Mask Technique

The SS type samples were prepared using a shadow mask consists of a metallic sheet with 'H' shaped cut-outs. A 200 μm wire passes through the middle of the 'H' shape vertically as shown in the Figure 2.10(a). A clean 3 inch Si/Si_3N_4 wafer is attached to this mask and then the electrodes were formed using the evaporator.

This method is much simpler, quicker and involves no chemical treatment on the wafer. However the dimensions of the electrodes could vary slightly because of the round shape of the wire forming the crucial part of the electrodes. Also the surface profile of the electrode shows a gradual slope at the end of the electrodes.

2.3.2 Photolithography

Samples type L1 and L2 were prepared using photolithography technique. Photolithography is a process used to fabricate microstructures by using ultra violet light to transfer patterns from a pre-designed mask to a film of light sensitive chemical called photoresist which is deposited on top of the substrate. The dissolvability of photoresist in the developer changes after exposure of UV light. Structures with size down to $1\mu m$ can be fabricated using photolithography. The process is carried out in the following steps (a schematic diagram of the process is shown in Figure 2.11):

1. Substrate cleaning

2. Photoresist coating

3. Pre-baking
4. Exposure
5. Development
6. Deposition/etching
7. Lift-off/photoresist removal

The substrate on which the electrodes are to be formed is first cleaned with standard cleaning process described in Section 2.3.4 to remove any dust particles or any other contamination which could affect the subsequent stages in the photolithography. After cleaning, a film of photoresist (in our case AZ1518) of thickness 300 nm ±10 nm is coated at a speed of 4000 rpm for 45 seconds using a Laurrels 400B spinner. The photoresist film smoothness and thickness can be controlled by changing spin coating parameters e.g. speed and time. The process of spin coating is simply governed by the centrifugal force which helps get rid of excess material and the bumps, making the surface smooth with a final roughness of ±10 nm [16]. The photoresist is usually a viscous liquid which is applied via a disposable pipette prior to the spinning. The bottom layer of this viscous fluid (i.e. photoresist) adheres better to the substrate compared to the layer lying on top of the first layer and hence when a centrifugal force acts upon it due to the substrate spinning and a smooth thin layer is formed due to a viscous flow.

After spin coating the photoresist, the substrate is baked at 100°C for 90 seconds using a hotplate. This step helps remove any residual solvent in the film. Using a mask selective regions of the substrate with photoresist coating are exposed to ultra violet light (λ =348 nm) for 12 s. The process is carried out using a mask aligner which also facilitates in aligning any previously fabricated structures using built-in optical microscopes.

In order to create negative slope edges especially for lift-off process the substrate is dipped in toluene for 60 seconds and then blown dried with nitrogen gas. This enables the modified top layer of the photoresist to be developed at lower rate and thus create an undercut, which is desirable in the lift-off process. The region exposed becomes soluble in a basic developing solution in case of positive photoresist which is the most common resist being used (AZ1518 was used in my experiments, which is also a positive photoresist). Whereas in the case of negative

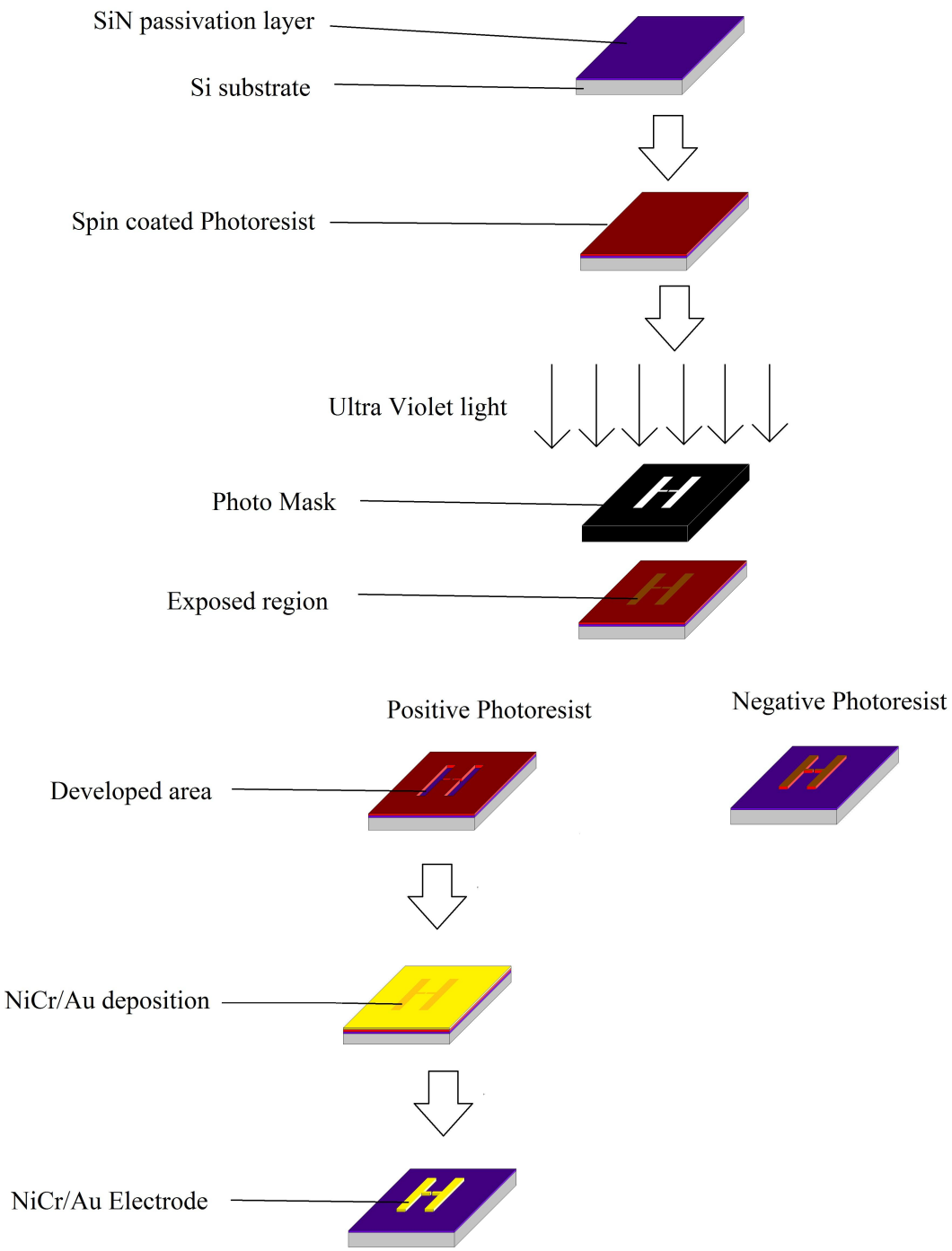

Figure 2.11: A schematic of photolithography process.

photoresist unexposed regions become soluble in an organic developer. After the development process the substrates are baked again to remove any standing wave affect to make the edges much sharper. Moreover the post exposure bake is very critical in chemically amplified photoresist [57].

After all of the above steps we get a pattern of the photoresist on top of the substrate. The substrate is then taken to a thermal evaporator for deposition of material e.g. NiCr/Au in our case. Alternatively, one can remove and etch material of substrate or any other pre-deposited layer from the uncovered region if so desired. After NiCr/Au deposition the photoresist is stripped off along with the unwanted material deposited on top of it using acetone. This process is called lift-off.

Mask writer

As described above a photo-mask is required to expose the substrate coated with photoresist in order to perform the photolithography. The masks are prepared by transferring a computer aided design to a quartz slab with chrome layer using a mask writer. The process of preparing masks is similar to that used for photolithography. The only difference is exposure method, as there is no mask to expose the photoresist coated on top of the chrome layer on a quartz slab. Instead a highly focused laser beams scans the whole area and exposes the desired spots according to the designed fed to the mask writer computer. After the exposure the resist is developed. The parts of chrome layer not covered by photoresist are etched after the development step.

For preparing different mask for my experiments the Tabletop Laser Pattern Generator μPG 101 was used. One can achieve features as small as 1 μm with this mask writer. L-Edit software was used to design and generate files in the proper format for the mask writer.

Mask aligners

A Karl Suss MJB 3 Mask aligner was used to expose the substrates using photomasks in contact mode. Contact mask aligners are the most common type of aligners used in laboratories due to cost effectiveness and simple operation. A mask aligner is important as it not only helps exposing the substrate through the mask but also facilitates in aligning the features on the substrate, from previous

lithography, to the features on the mask. All mask aligners usually have following things in common:

- A mask holder for carrying mask.
- A wafer chuck to hold the wafer.
- A microscope to see and align the mask.
- Control knobs for moving mask relative to the wafer.
- Knobs to control the spacing between mask and wafer.
- UV source and shutter assembly with a timer for exposure.

2.3.3 Evaporator

An Edwards Auto 306 thermal evaporator was used to deposit NiCr/Au electrodes. Evaporation is a widely used thin film deposition technique. Metals are heated up using an electrical current until they are evaporated in vacuum conditions. The system is equipped with a diffusion pump to produce a vacuum of the order of 1×10^{-5} Torr prior to deposition. The substrate is placed straight above the evaporation source and the atoms evaporated are deposited on the substrate surface. A Film Thickness monitor (FTM) is used to calculate the deposition rate. Gold (Au) pallets and Ni/Cr wires both with 99.999% purity were used for this purpose. A current of 1.5 A was used for evaporation.

2.3.4 Substrate cleaning

All the substrates were cleaned before putting into the chamber for deposition, to avoid any unwanted contamination. The substrates are taken from clean wafers but processes like electrode deposition (via shadow mask technique or photolithography technique) can cause contamination. All substrates were cleaned using following standard cleaning process:

1. A five minute ultrasonic bath cleaning using acetone
2. A five minute ultrasonic bath cleaning using Iso-Propyl Alcohol (IPA)
3. Substrate were dried out using 99.99% N_2

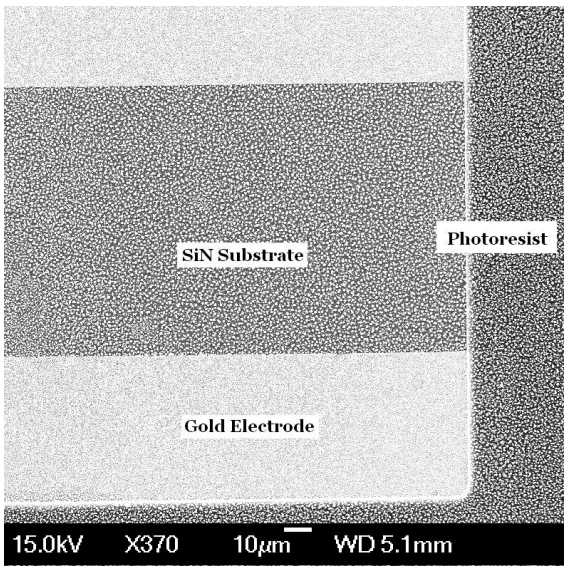

Figure 2.12: A typical SEM micrograph showing gold electrodes on top of Si/Si_3N_4 substrate. Gold electrodes appear brighter due to their high conductivity. The grains visible are tin (Sn) particles deposited.

2.4 Scanning Electron Microscopy (SEM)

The magnification of a traditional optical microscope is limited by the minimum wavelength of visible spectrum of electromagnetic waves (which is between $\sim 400nm$ (violet) and $\sim 700nm$ (red)). To surpass this hurdle, high energy electron beams with tight focusing are used as a probe for a better resolution and magnification.

Scanning Electron Microscopy (SEM) is the primary way to determine the structures of the deposited films during the experiments presented in this thesis. SEM generated micrographs can have magnification of up to 500,000 times and can help examine structures less than 5nm.

SEM uses a highly focused electron beam which raster scans the surface under investigation. The electrons with few keV interact with the surface atoms and produce various effects including secondary electron emission, back scattered electrons and characteristic X-rays, each of which contains of information about the surface structures and morphology. The intensity of secondary electrons signal is directly proportional to the incident angle of the probe beam as the escape depth for secondary electrons reduces significantly for a beam with a greater incident angle compare to one colliding head on to the surface [58].

The emitted secondary electrons (usually with energy less than 50eV) are detected by a Everhart-Thornley detectors. These detectors consist of a scintillator placed inside a Faraday cage with a low positive bias that attracts any secondary electrons generated. The optical signal produced by the scintillator is then taken out of the evacuated specimen chamber by a light pipe that is connected to an external photomultiplier tube which converts it to an electrical signal. The surface profile of specimen can be generated by raster scanning the desired area with a highly focused beam of incident electrons and recording the intensity of secondary electrons at each spot. The signals produced by the photo multiplier tube (PMT) can be fed either directly to a cathode ray tube or can be processed digitally in order to generate an image.

Any electrically insulating areas on a specimen under the electron beam get negatively charged due to the incident electrons. These charged areas exert a repulsive force on the probing beam resulting in less secondary electron emission compare to the conducting regions of the specimen. Hence in SEM micrographs insulating regions appear darker compare to the conducting regions (Figure 2.12). All specimens should be electrically grounded to avoid unnecessary charging which cause a drifting effect and distort the micrograph. One needs to be careful in selecting the energy of the electron beam to get optimum resolution. Sn cluster films in our experiments were examined using 10 to 15 keV. Higher energies can cause melting the nanoparticles.

The intensity of Back Scattered Electrons (BSE) from samples is dependent on the atomic number of the material they are getting scattered. Materials with higher atomic number back scatter more electron compared to the material with lesser atomic number. A dedicated BSE detector is placed in the specimen chamber to detect these high energy electrons. The image attained using BSE signal has a contrast variation for different type of atoms.

Also the characteristic X-rays are utilized to identify the elements present in a specimen. Characteristic X-rays are emitted when incident electrons knock out a core shell electron. X-rays are emitted due to the subsequent filling of this hole by a higher shell electron. By analyzing the wavelength of emitted X-rays, we can find out the material and chemical composition of the specimen as only certain wave length are emitted by every element.

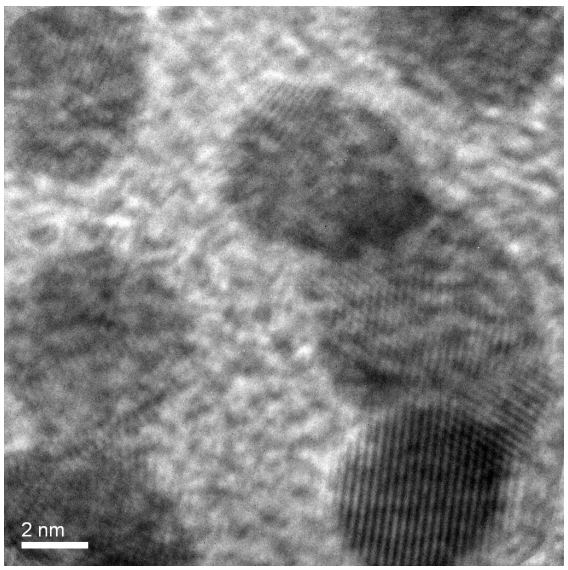

Figure 2.13: A typical HRTEM image (Gold nanoparticles on a TEM grid).

2.5 Transmission Electron Microscopy (TEM)

Transmission electron microscopes use a focused high energy electron beam just like SEM described in previous section but instead of using secondary electron to form an image a TEM uses transmitted electrons through the specimen. The specimen for TEM must be very thin to allow the incident electron beam pass through. The electrons passing through the specimen formed a magnified shadow which is focused on a fluorescent screen or a CCD detector.

At lower magnification the image is formed due to the blockade of electrons due to the specimen atoms. Whereas at higher magnifications in HRTEM the image contrast is modulated because of the electron wave interaction. Figure 2.13 shows a HRTEM micrograph of gold nanoparticles on top of a TEM grid. The fringes visible in the nanoparticles represent atomic plane orientation of gold crystal structure. The image contrast does not directly represent the atoms rather a detailed analysis is required to infer useful results. TEM not only provides higher resolution ($\sim 1,000,000$ times) than SEM but also can be used to see the crystal structure of the specimen under investigation [59].

2.6 Coverage Measurements

The coverage of deposited clusters on a substrate was estimated using an in situ film thickness monitor which provides deposition rate and film thickness. Here it should be clarified that the FTM measures the mean thickness of the film. For simplicity a cluster film could be considered as a hexagonal close packed layer of spherical clusters each with diameter D. The actual thickness of such film will be will be more than the mean thickness measured by FTM, because of the gaps between spherical clusters. Therefore, for example, if one wants to deposit a film with an average thickness equivalent to that of one monolayer (1ML) of clusters of diameter D, a film of thickness $\pi D/(3\sqrt{3}) = 0.605D$ (measured by the FTM) should be deposited.

The critical percolation threshold for an infinite 2D square lattice is $p_c = 0.5927461$ [33]. A more realistic model for our films is an infinite 2D continuum model where the clusters are not restricted to lattice sites. The percolation threshold of such systems are found to be $p_c = 0.68$ [60].

As the overall coverage of the film p increases the probability of new clusters falling into first layer become less and less. It is possible to deduce the coverage needed to have a percolating path in the first layer using following equation [33]:

$$p = -ln(1 - p_1) \tag{2.3}$$

Where p can be greater than 1 but p_1 has a value between 0 and 1. For 2D continuum model coverage of 1.13 ML is required (as $p_1 = 0.68$). For actual coverage measurements, SEM Images are obtained and are digitally processed and analysed using ImageJ software [61]. Figure 2.14 shows a SEM image of coalesced tin (Sn) particles with 82.6% coverage. To calculate the coverage, the gray scale image is converted to a binary black and white image. The threshold is adjusted carefully to distinguish substrate (represented by black colour in right image in Figure 2.14) and the white colour represents deposited material i.e. the Sn cluster film, after which the coverage can be calculated by measuring the ratio of white to black pixel ratio. SEM images also provide a scale bar which can be used to calibrate the image and to find the actual size distribution of the clusters forming the film.

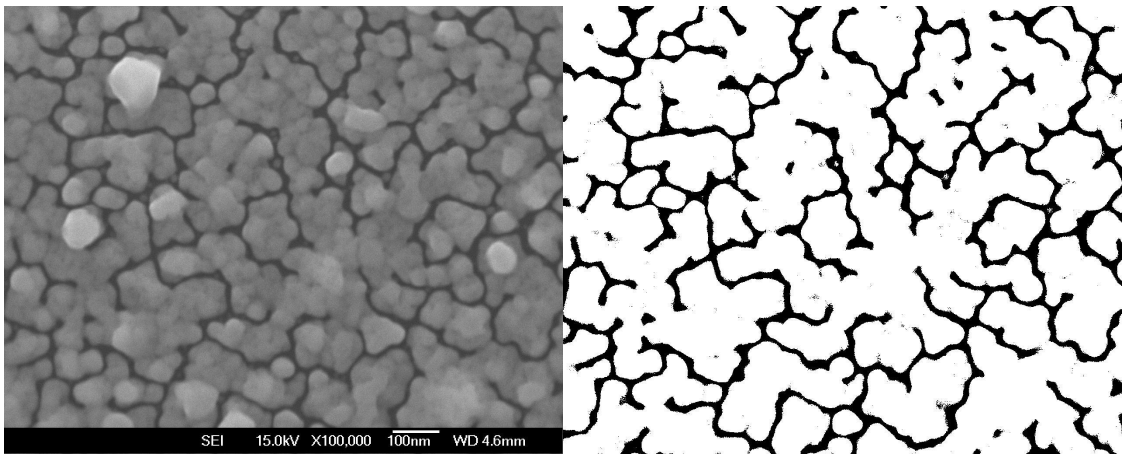

Figure 2.14: (On the left) SEM of tin (Sn) coalesced clusters. (On the right) SEM gray scale image converted to binary image using Image to measure coverage.

2.7 Grain Size Measurement for Cluster Films

Generally, average grain size in any cluster film can be used to quantify film morphology. In many cases, the cluster films discussed in this thesis are highly coalesced. These cluster films consist of big cluster islands with a few hundred to a few thousand nm^2 area. The islands are random in shape and most of the time partially connected to other nearby islands. In such cases where no individual clusters are visible it is really hard to measure the particle/grain size.

To and find out average grain sizes of such coalesced films Watershed algorithm was used. SEM image of 1×1 μm^2 randomly selected area was captured for each sample. Figure 2.15(a) shows a typical Sn cluster film with coalesced cluster islands. Grain size was then measured for all the grains defined by the algorithm. Average value of all the grain sizes was used to quantify the film morphology of certain sample. Figure 2.15(b) and (c) show same image after thresholding and applying watershed algorithm to isolate grains in the islands. In final step ImageJ software was used to count the number of the isolated grains and their area (A) as shown in 2.15(d). Grain size was then estimated using $D_g = \sqrt{\frac{4A}{\pi}}$.

2.8 Conductance Measurements

As discussed in Section 2.1.6 sample holder in the deposition system has facility to do electrical measurements of samples in situ. This section discus some details

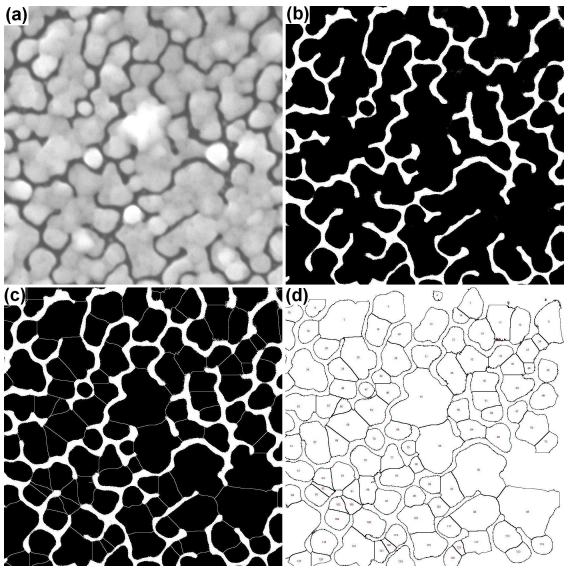

Figure 2.15: Grin size measurement using watershid technique. (a) Original SEM image. (b) Threshold image: black and white pixels representing clusters and substrate respectively. (c) Grain boundary defined by watershed algorithm. (d) Isolated grains for measure grain size.

about the measurements important with respect to Chapter 4.

Conductance measurement were carried out by measuring current and voltage across the Sn cluster films using Keithley 6514 electrometer and Keithley 2000 multimeter respectively. To measure conductance during the deposition 50 mV bias was used for SS and L1 and 5 mV for L2. To study the sample conductance at different voltages, applied voltage was swept in various wave forms using either a power supply with analogue waveform generator or IOtech digital-analog converter along with a Lab view program.

The current and voltage values are measured separately at sampling rate of 5 Hz. During the data acquisition there is a time delay of 50 to 70 ms between current and voltage measurements as shown in Figure 2.16.

The delay can be calculated by analyzing the current and voltage curves near the points where voltage V is crossing V=0 line. y number of data points are selected on each side of the point where the voltage crosses V=0 line. A function $F(\Delta t)$ is defined for each such data set using Equation 2.4 and 2.5 where G is a matrix containing all conductance values. The average delay was found by minimizing function $F(\Delta t)$ in equation 2.5. A similar approach to find out time delays is presented in [62]. The voltage curve is then shifted to the left by Δt

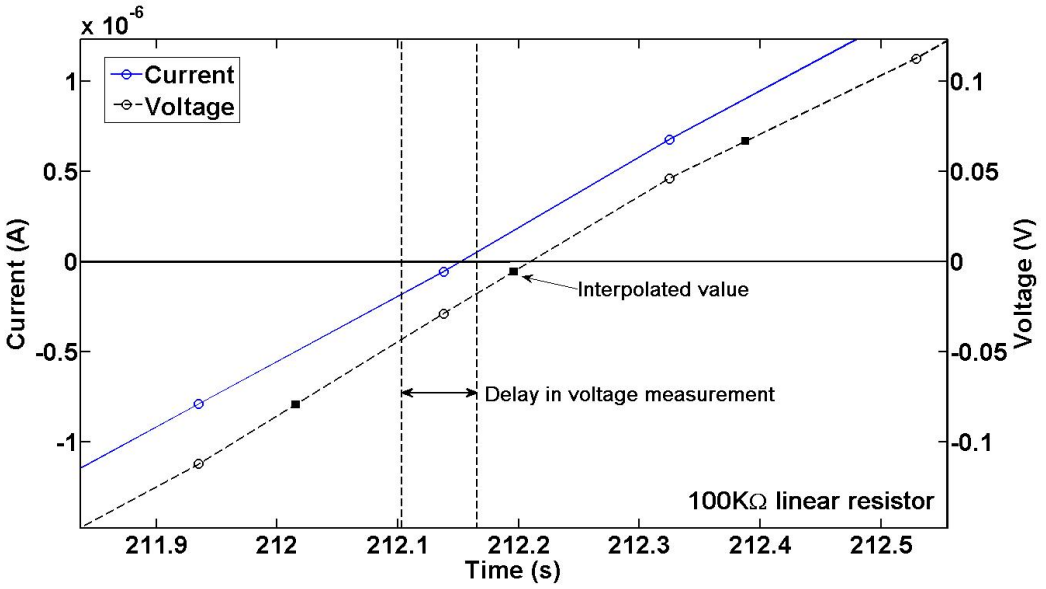

Figure 2.16: Plot showing a delay of 58 ms between voltage and current measurements. To find the correct value of conductance, voltage curve was shifted to the left by 58 ms and the voltage values corresponding to current values at certain time were found out by interpolation.

and new values of conductance corresponding to current data points are found by interpolation.

$$g_i = |G_k - \frac{1}{2y}\sum_{k=x_i-y}^{x_i+y} G_k| \qquad \forall \qquad k = x_i - y \text{ to } x_i + y \tag{2.4}$$

$$F(\Delta t) = \frac{1}{n}\sum_{i=1}^{n} g_i \tag{2.5}$$

Figure 2.17 shows a measured conductance (solid line) for a 100 KΩ linear resistors. Inset of Figure 2.17 shows function $F(\Delta t)$ plotted against Δt clearly showing a minima at 58 ms. Corrected conductance is found by shifting the voltage curve by $\Delta t = 0.058$ and is shown in Figure 2.17 (line with data marker '+').

2.9 Summary

In this chapter the deposition system has been introduce along with. Preparation of substrate has also been discussed along with introduction to the terms that will be used for different type of samples in the rest of the thesis. In the final part of

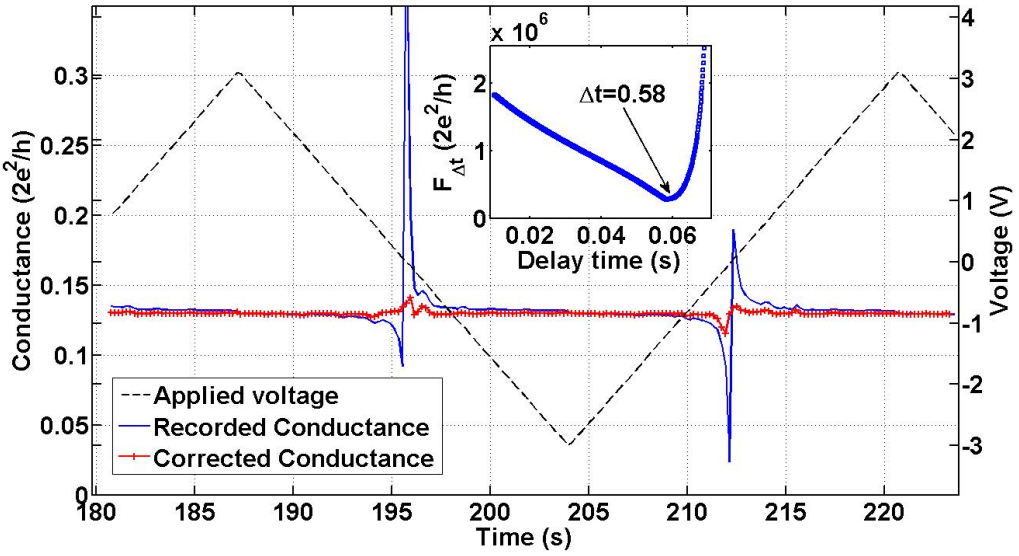

Figure 2.17: Correction of recorded conductance by removing the time delay in recorded current and voltage values. Inset shows the function $F_{\Delta T}$ plotted for a range of ΔT values to find out minima which represent the average delay in current and voltage values recorded at any given time.

this chapter some details about coverage, grain size and electrical measurements are discussed.

Chapter 3

Coalescence in Sn and Pb Cluster Films

The process by which two or more particles merge together to form a bigger particle is called coalescence. The morphology of cluster films changes due to coalescence of individual clusters and assemblies of clusters. This change in morphology becomes important in percolating films as small changes in surface coverage can lead to large changes in overall film behaviour.

Coalescence has implications for film morphologies and hence on durability and failure of devices fabricated using clusters, such as thin film gas sensors [63]. Therefore understanding coalescence between clusters is of great interest. However in cluster films it is difficult to observe time evolution of the coalescence of individual clusters by observing them directly using SEM or TEM, because of uncontrolled heating due to electron beam itself. As an alternative way, coalescence can be studied indirectly by observing another related property such as conductance [64].

In percolating films the overall conductance depends on the conducting paths formed between the adjacent clusters. Due to coalescence the contact area of these interconnecting clusters grows with time causing an increase in the conductance. This conductance variation of cluster films was used to investigate coalescence observed during the experiments presented in this chapter.

To begin, a literature survey is presented on the coalescence of micro and nanoparticles, along with the work on coalescence done previously at UC. Later in the chapter experimental results for Sn and Pb clusters are presented followed by conclusion in the end.

3.1 Literature Review

3.1.1 Coalescence Due to Diffusion

Metallic clusters and nanoparticles coalesce together to form bigger particle due to surface diffusion. Surface diffusion is one of major source of mass transport at nanoscale and is dependent on factors like temperature and chemical potential which is associated with surface curvature [65]. A net flux of atoms diffuse towards the high curvature surfaces at the neck formed between two clusters are in contact. The diameter of the neck between clusters increases due the preferential diffusion.

A lot of experimental and theoretical studies of coalescence between particles of different sizes have been reported over the past half century. According to previous studies [64, 66, 67, 68, 69, 70, 71] the process of growth of necks between two connected particles follows a power law in time. One of such study [64] in 1949 showed that the sintering process follows a power law with exponents $\frac{1}{2}, \frac{1}{3}, \frac{1}{5}$ and $\frac{1}{7}$ for viscous flow, evaporation-condensation, volume diffusion and surface diffusion respectively [72, 73, 74].

In later studies Nichols et al. [68] also suggested that the neck growth between spherical particles during coalescence follows a power law in time. Nichols showed that the exponent is dependent on x/a which is the ratio of the diameters of the neck and the original sphere. Using numerical simulations the exponent was found to be in a range between $\sim \frac{1}{5.6}$ and $\sim \frac{1}{8}$ for $x/a = 0.05$ to 0.7. The value of the exponent decreases sharply when $x/a > 0.7$.

Blachere et al. [69] derived an analytical solution for the sintering time of submicron particles. The sintering process was divided into necking and spherodization stages. In the necking stage the contact area (i.e. the neck) grows such that the clusters maintain their individuality up to an extent. After necking the two coalesced clusters merge completely together to form a single big spherical cluster. The total time for the necking and spherodization stages was found to be proportional to a^4. However, the time for spherodization was found to be ∼17 times longer than the necking time.

3.1.2 Crystallographic Reorientation during Coalescence

In nanoparticles coalescence can sometimes be preceded by crystal reorientation. It has been reported that the coalescence is much more swift if a twin boundary is

formed between two coalescing particles [75]. The simulations by Theissmann et al. showed that the coalescence between two particles can be suppressed if they do not find a suitable reorientation.

José-Yacamán et al. [63] discussed the coalescence process in nanoparticles. Liquid like properties of surface layers play an important role in coalescence. As two nanoparticle's surfaces are in contact atoms rearrange to align the coalescing planes. High liquid like mobility is necessary for this process. Moreover, smaller particles are rearranged to align with bigger particles while coalescing.

3.1.3 Electrical Measurements of Coalescing Particles

In 1950 Dedrick and Kuczynski [76] proposed a method to measure self-diffusion in metals by measuring the contact resistance between two metallic spheres. Later on Massachi [77] used this method to measure sintering and coalescence of the neck between copper wires. In 2001 Peng et al. [78] adopted this technique to analyze coalescence between cobalt nanoparticles. In this chapter a similar approach has been used to study coalescence in Sn and Pb clusters.

To study coalescence using the above mentioned procedure it is necessary to link the resistance of the neck to its radius. It is well known that the resistance of small contacts can be determined using either Holm's equation [79] or Sharvin's equation [80], depending on size of the neck radius r and mean free path for the metal l_0. Holm's law is applicable when $r \gg l_0$ and is:

$$R_H = \rho/2r. \tag{3.1}$$

On the other hand if $r \ll l_0$ Sharvin's law should be used:

$$R_S = \frac{P_F}{N\pi e^2 r^2}. \tag{3.2}$$

Here P_F is the Fermi momentum of electrons, N is the electron density and e is the elementary charge. In short it can be said that the conductance of necks between clusters can be written as:

$$G \propto r^{\omega}. \tag{3.3}$$

As discussed before the neck growth due to coalescence follows power law i.e.

$$r \propto t^{\alpha}. \tag{3.4}$$

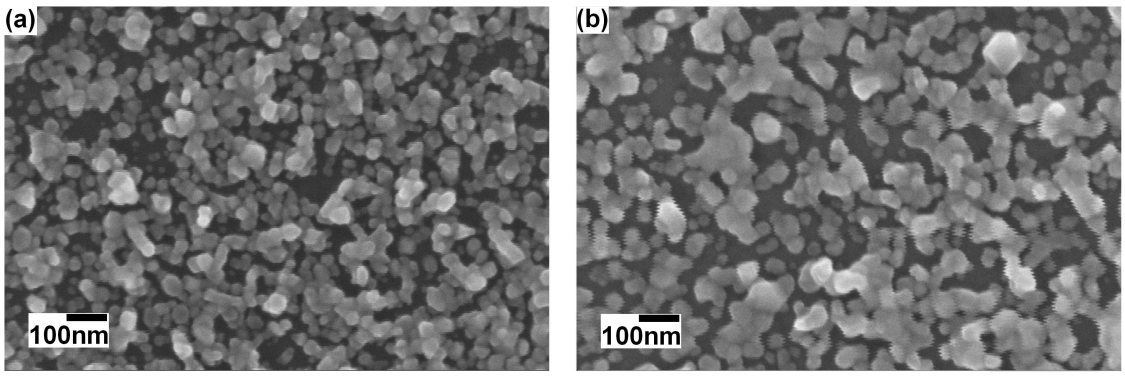

Figure 3.1: Effect of coalescence on the cluster film morphology. SEM image of Bi cluster film (a) after deposition (b) after 3 days in vacuum showing coalescence [45].

Hence combining equation (3.4) and (3.3) yields:

$$G \propto t^{\beta}. \tag{3.5}$$

According to Equation (3.4), (3.3) and (3.5) the conductance G of a growing neck can be used as a measure of the neck radius and hence coalescence. The value of the exponent (β) in Equation (3.5) can be determined by fitting the $G(t)$ data from experiments to a power law.

3.1.4 Investigations of Coalescence at UC

Previously at UC, experiments on Bismuth (Bi) cluster films showed that due to coalescence the morphology of films changes over time while kept in vacuum [45]. As an example, Figure 3.1 shows the effect of coalescence in a Bi cluster film. A freshly deposited Bi cluster film showing some coalescence can be seen in Figure 3.1(a). These clusters coalesced even further to form bigger structures after 3 days in vacuum as shown in Figure 3.1(b) [45].

Efforts have been made to determine the coalescence rate in these cluster films. Coalescence was investigated both experimentally and by using computer simulations. McCarthy [44] developed a model of cluster coalescence due to atomic diffusion with a rate which depends on the number of atomic neighbours. Kinetic Monte Carlo (KMC) simulations of atomic clusters were performed to investigate their coalescence behaviour. In these simulations clusters with 15,000 to 130,000 atoms and Face Centred Cubic (FCC) structure were simulated using lattice based surface diffusion.

The simulation results of coalescence between two clusters are shown in Figure 3.2. Coalescence between simulated clusters starts with a configuration shown in Figure 3.2(a) and evolves to that shown in (b) and (c) over time. The results showed that in the early stages of coalescence, a large number of atoms diffuse towards the high curvature neck formed between two clusters. Due to this influx of atoms the neck grows quickly in the beginning.

The shape of the clusters evolves from sphere→dumbbell→ovoid →sphere as has been previously predicted in Molecular Dynamics (MD) studies [81, 82]. A new power law with exponent $\frac{1}{3}$ [44] was found for the early stages of coalescence that is different from previous theories (see Figure 3.2(d)). Also, it was observed that in later stages[1] the coalescence become much slower, and a smaller exponent with a value 0.03 was observed (see Figure 3.2(e)). McCarthy argued that the reason for the smaller exponent is the effect of faceting on the availability of atoms for diffusion. Figure 3.2(e) shows the conductance curves obtained from the KMC simulations. The conductance is calculated using bulk scattering ($\omega = 1/2$) as mentioned in [45].

In general, the coalescence time is longer for larger cluster sizes as the atoms have to flow over larger regions during the surface diffusion. On the other hand an increase in temperature decreases the coalescence time as it increases the diffusion rate of the individual atoms. A third variable, i.e. the crystal plane at which the clusters intersect during coalescence also plays an important role in defining the path of relaxation. The experimental results for Bi also show an exponent in a range of 0.01 to 0.04 which is not very different from the simulation results [45].

3.2 Current Work: Coalescence in Sn and Pb

In the previous sections coalescence has been introduced along with a brief literature review. Studies presented in the following sections are a continuation of the same work. In the current work the coalescence of Pb and Sn was investigated in a similar way as for Bi. The conductance of the cluster films is recorded in order to find out how the neck between two adjacent clusters evolves over time due to coalescence. Before moving on to the results, the following section summarises the experimental conditions used during the experiments.

[1] Where $\frac{\text{Neck radius}}{\text{cluster radius}} \geq 0.5$

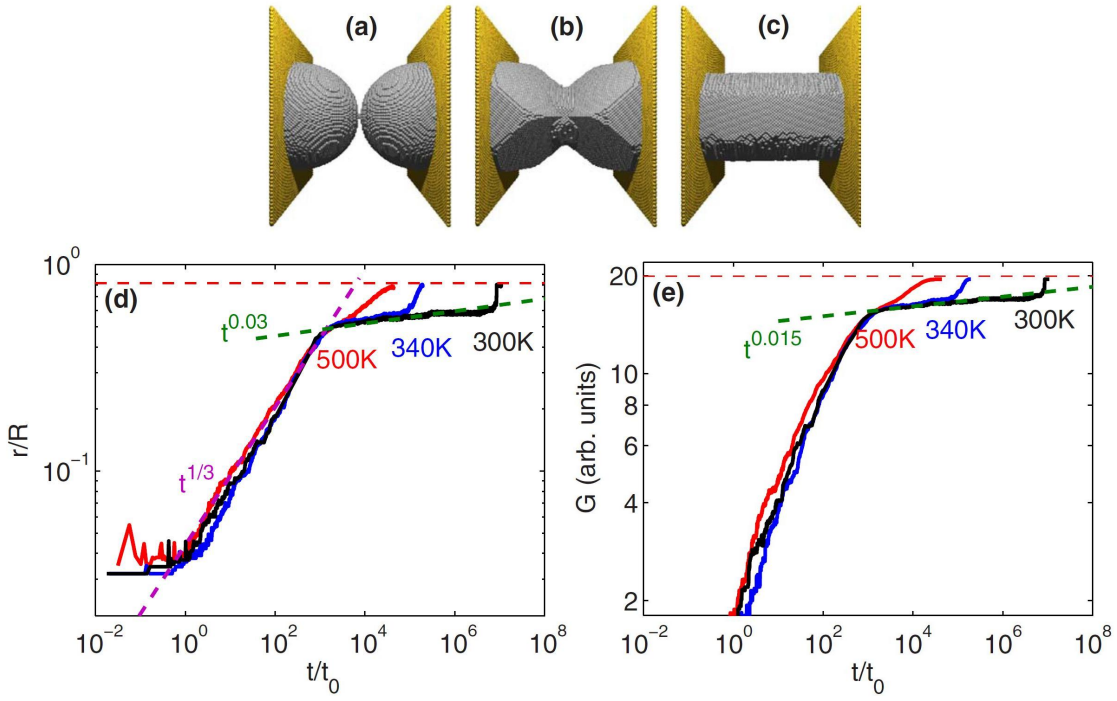

Figure 3.2: KMC simulation of coalescence of two supported clusters. (a), (b) and (c) show different stages of coalescence. (d) Change in normalized neck radius for different temperatures over time. Initial stage can be fitted to power law with exponent $\frac{1}{3}$. (e) Conductance of the neck increasing over time. A late stage of coalescence exhibiting power law exponent of 0.015 in conductance data [44].

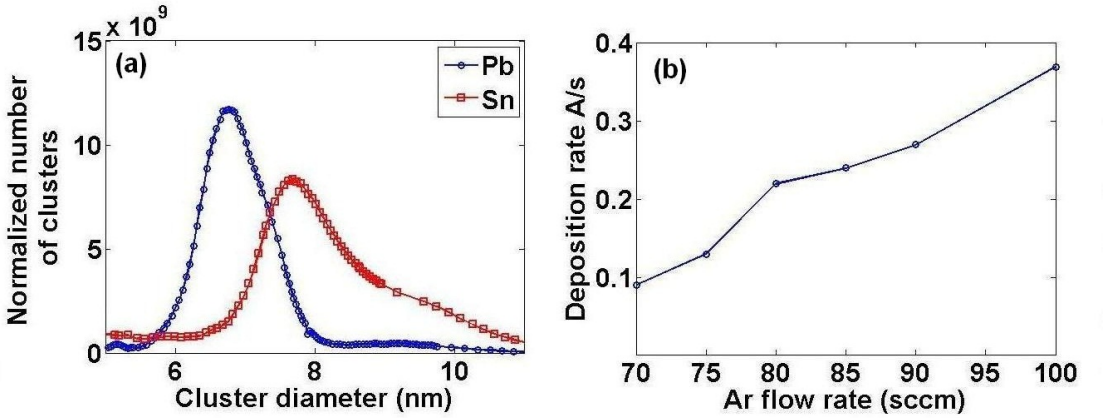

Figure 3.3: Effect of Ar flow rate on (a) size distribution of Sn and Pb clusters at 100 sccm (b) deposition rate at various flow rates.

3.2.1 Experimental Conditions

First of all it is important to note the difference in experimental conditions in the current work and past Bi experiments. In the experiments presented in this chapter, Sn and Pb cluster films were deposited using the UHV-compatible sputter source (see Section 2.1.3) in contrast to the Bi which was deposited using evaporator source [16]. Moreover, in the current experiments Sn and Pb clusters with diameters ranging from 5 nm to 10 nm were used compared to ∼30 nm for Bi, as evident from mass spectra shown in Figure 3.3(a).

SS type substrates (Section 2.3) were used throughout the coalescence experiments. Before depositing clusters the substrates were cleaned using the standard procedure given in Section 2.3.4. For electrical measurements 100 mV was applied across the samples.

Typical source conditions used for experiments are given in Table 3.1. As shown in the table Argon flow rates of 100 sccm were used for all coalescence experiments. This flow rate was chosen because the maximum deposition rate was achieved (see Figure 3.3(b)). It was observed that on further increase of flow rate the deposition rate drops. Further details of source characterization can be found in Section 4.4.1. From here on new results are presented.

Parameter	Values
Argon flow rate	100 sccm
Sputter Power	15 (Pb) and 20 W (Sn)
Aggregation length	8 cm
Mass analyser chamber pressure	$\sim 1 \times 10^{-4}$ Torr
Deposition chamber pressure	$\sim 1 \times 10^{-6}$ Torr

Table 3.1: Experimental conditions for producing lead (Pb) and Tin (Sn) clusters for studying coalescence effect.

3.2.2 Electrical Measurements of Coalescence in Sn and Pb

Figure 3.4 shows the evolution of conductance during and after the end of deposition. It is clear from the figure that the conductance of this sample is very low until the onset point[2], after which the conductance increased rapidly. The quick increase in conductance can be attributed to the increase in the film coverage due to further deposition [83]. After the onset is achieved, the deposition of clusters was stopped by closing the gate valve, which also isolates the deposition chamber from the rest of the system (see Section 2.1) and ensures a better vacuum. The samples were kept under vacuum ($\sim 1 \times 10^{-6}$ Torr) to observe changes in conductance due to possible coalescence between clusters.

Examples of coalescence in Sn and Pb films are presented in Figure 3.5(a) and (b) which show SEM images of samples prepared by depositing ∼7.5 nm and ∼6.5 nm clusters of Sn and Pb respectively. After the deposition samples were left in vacuum for several days. It is clear that the clusters have coalesced together while they were in vacuum as no clusters of <10 nm are visible anymore.

It was observed that after the end of deposition the conductance of the samples keeps on increasing even though there were no more clusters arriving on the substrate. This increase in conductance is believed to be due to the growth of necks between the clusters (i.e. coalescence). Figure 3.6 shows a typical change in conductance after the end of deposition for both Sn and Pb samples. In both cases there was a conductance change of about 5% in a 300 s period after the end of deposition. To determine the coalescence rate more precisely the conductance data acquired during experiments was fitted to various power laws. The fitting

[2]The onset point is the time at which a percolating network of nanoclusters is formed between the electrical contacts used for measuring the conductance of the film.

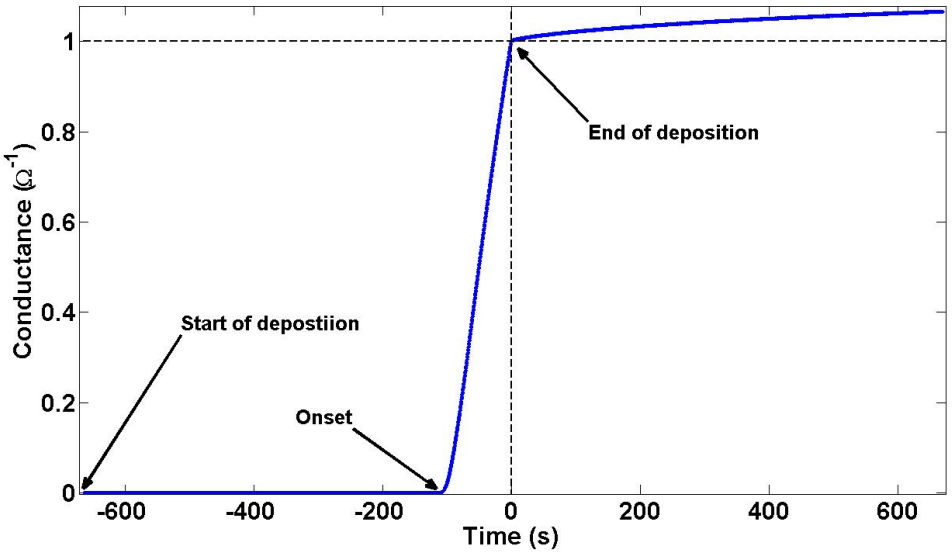

Figure 3.4: Conductance versus time $G(t)$ plot of a Pb sample during and after deposition. Sharp increase in conductance can be seen at the onset point. After the end of deposition the conductance increases due to coalescence.

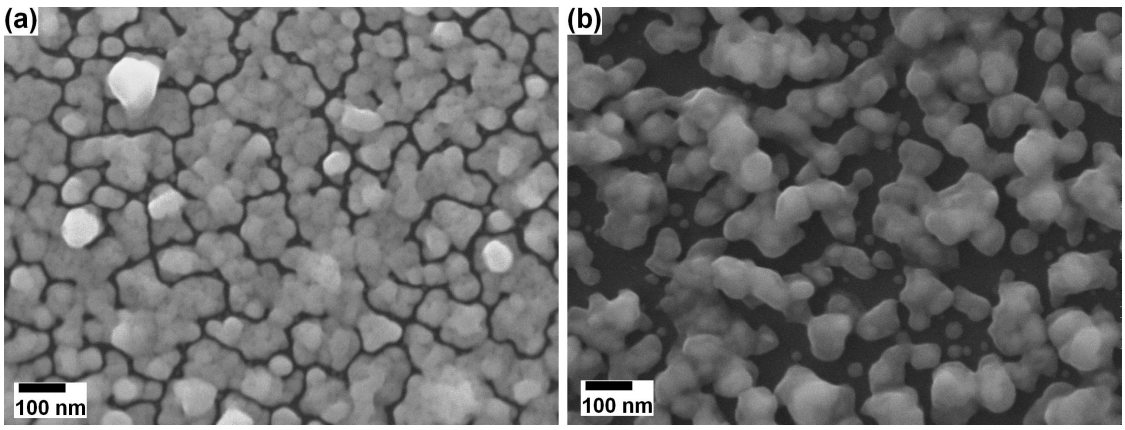

Figure 3.5: SEM micrograph of (a) Sn and (b) Pb clusters deposited on Si_3N_4. Individual clusters a rarely visible because of coalescence.

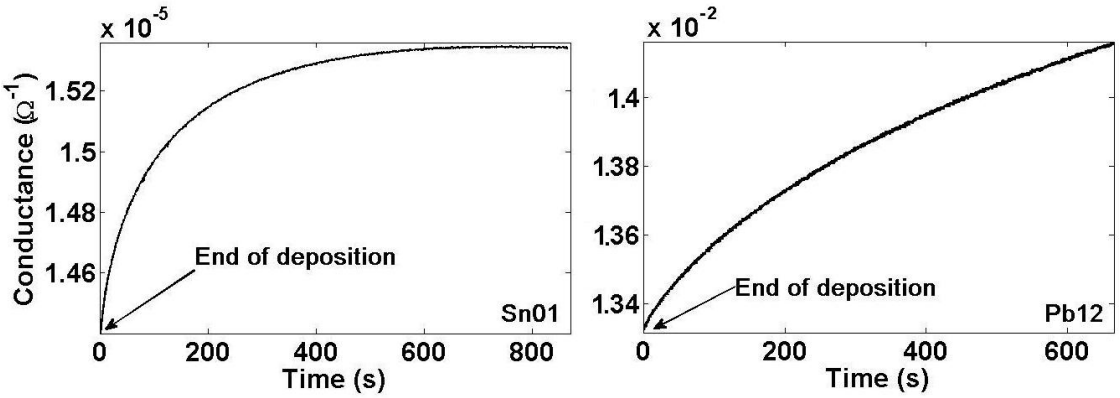

Figure 3.6: Increase in conductance of percolating film due to coalescence after end of deposition (a) Sn sample with deposition rate 0.15 Å/s. (b) Pb sample with deposition rate 0.13 Å/s.

procedure is discussed in the following section.

3.2.3 Fitting Procedure

As discussed earlier the growth of the neck radius between two coalescing clusters is believed to follow a power law (Section 3.1.1)and the exponent of the power law can in principle be determined by fitting the experimental data of the cluster films. Power laws with various numbers of fitting parameters can be used for this purpose. To find out the best option we have tried the following power laws during the fitting procedure [84]:

$$G(t) = a(t)^b \qquad \text{(Power law 1)} \tag{3.6}$$

$$G(t) = a(t - t_1)^b + c \qquad \text{(Power law 2)} \tag{3.7}$$

$$G(t) = a(t - t_1)^b \qquad \text{(Power law 3)} \tag{3.8}$$

where G is conductance, t represents time, and a, t_1 and b are fitting parameters.

Equation 3.6 considers that the coalescence in all the necks starts right after the end of deposition and there is no initial overlap between any clusters i.e. all neck sizes are zero at the beginning. This assumption is certainly not correct for our cluster films where the coalescence starts before the percolation threshold is achieved and many clusters land partially on other clusters forming instantaneously a non-zero initial neck.

Clusters overlapping at the time of deposition may be considered as two clusters

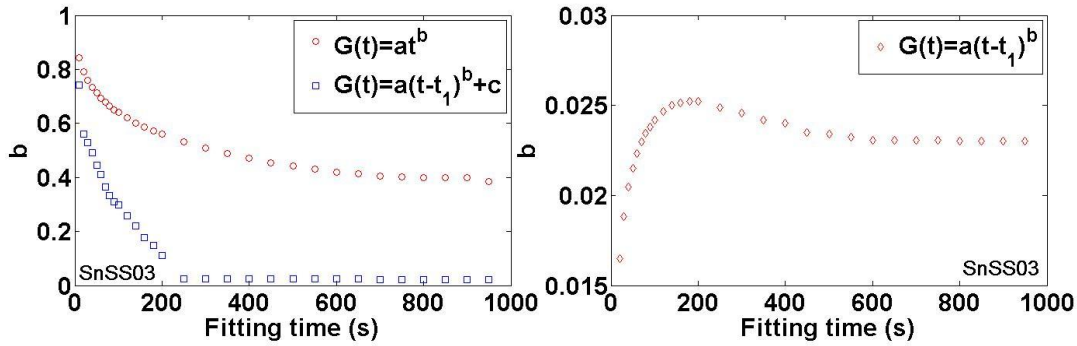

Figure 3.7: Variation in b found using different power laws with respect to fitting time. (Left) Power law 1 and 2 showing bigger variation in b values compared to that of (Right) Power law 3.

which are time t_1 advanced in coalescence compared to the clusters starting with zero neck size. Therefore the parameter t_1 is included in powers law 2 and 3. Power law 2 is more general but four fitting parameters give the fitting procedure a lot of freedom and hence it can even fit the data which does not, in fact, follow a power law [84].

All these power laws yield different values of b for the same data [84]. Moreover during the data fitting it was noticed that the value of b varies even for the same power law depending on the time range of the data used for fitting. Figure 3.7 shows that power laws 1 and 2 show a huge variation in b compared to power law 3 where b does not change much with fitting time. Another advantage of power law 3 is that the exponent b determined for conductance of whole cluster films is similar to the exponent β for individual necks (see Section 3.2.4 for further details). As discussed above Equation 3.8 is the best choice amongst all three equations and, hence, is used for fitting all the data.

Figure 3.8 and 3.9 show Sn and Pb experimental conductance data with fitted curves, respectively. Normalized conductance is plotted versus time (less the fitted t_1) on a $log - log$ plot showing that the data can be well fitted using power law 3 for all data sets.

The exponents determined by fitting data to power law 3 for each data set for both Sn and Pb are shown in Figure 3.10(a) and (b) respectively. The values of the exponent b of Equation (3.8) for all Sn and Pb samples are in the range of 0.01 to 0.03. The average values are 0.027 and 0.011 for Sn and Pb respectively. The observed power law exponents are consistent with values for Bi [45] and are

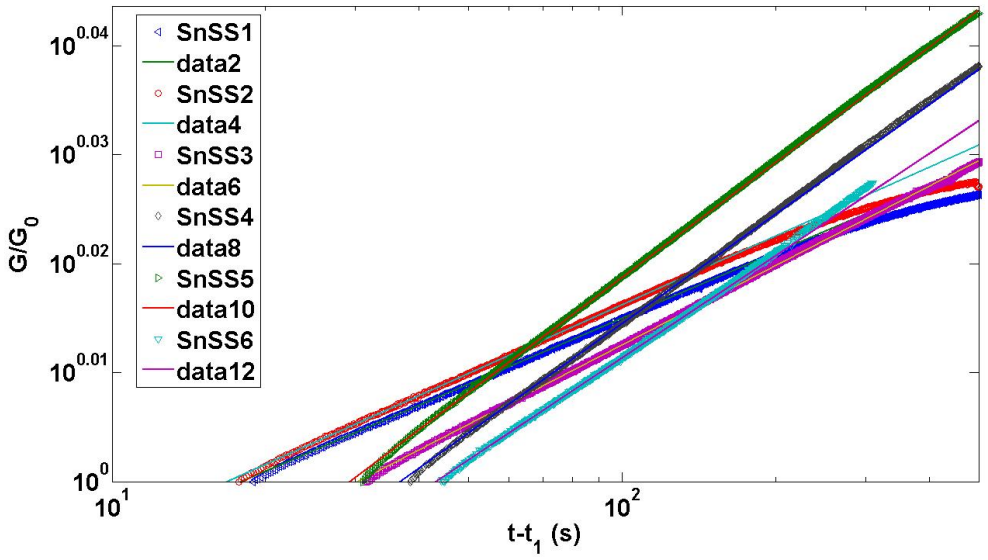

Figure 3.8: log-log plot of G(t) data of coalescing Sn cluster films fitted using power law $G(t) = a(t - t_1)^b$.

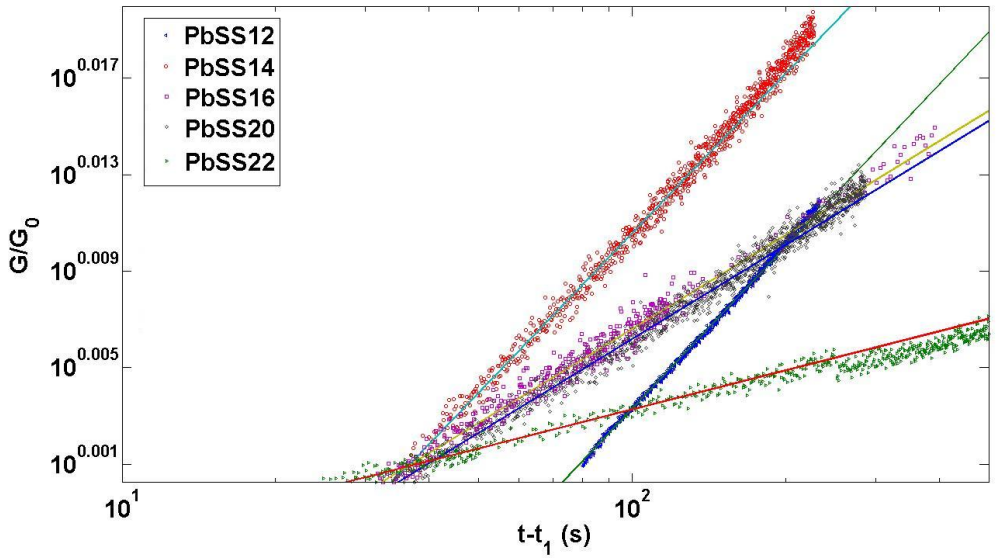

Figure 3.9: log-log plot of G(t) data of coalescing Pb cluster films fitted using power law $G(t) = a(t - t_1)^b$.

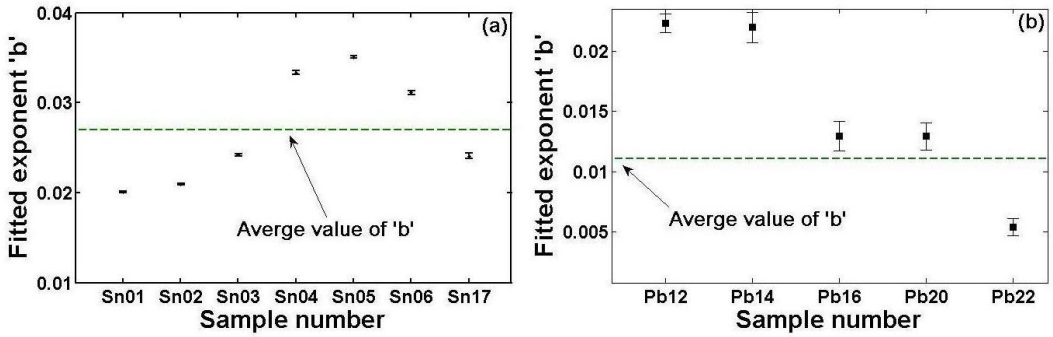

Figure 3.10: The power law ($G(t) = a(t - t_1)^b$) exponent 'b' values for (a) Sn samples (b) Pb samples. Dashed line shows the average value of b for the whole data set.

much smaller than predicted by Nichols and Mullins [67]. However these exponent values are very close to those found in McCarthy's KMC simulations for late stage coalescence [44].

It is important to note that the fitting procedure is being applied on the conductance data of the whole film which could contain thousands of coalescing necks. To find the exponent β for coalescence of individual neck, its relation to b (i.e. exponent for the whole film) should be determined. This issue is discussed further in the following section.

3.2.4 Relating b to β

A computer model was developed which mimics the cluster films to find out how the individual neck conductance variations affect the conductance of the overall film [84]. A 50×50 square percolating lattice of resistors was used for the simulations. As shown in Figure 3.11(a) the top and bottom row of the lattice was considered occupied and the resistance between each node was initially set to zero. To simulate deposition of clusters the lattice sites were occupied randomly. A variable resistance was defined between each occupied node with a time dependent conductance given by power laws discussed in Section 3.2.3.

The following facts were taken into account during the simulation [84]: (a) The clusters do not land on the substrate at the same time during the deposition so the necks are formed at different times. (b) Each neck starts growing due to coalescence right after its formation. (c) The percolating film is treated as a

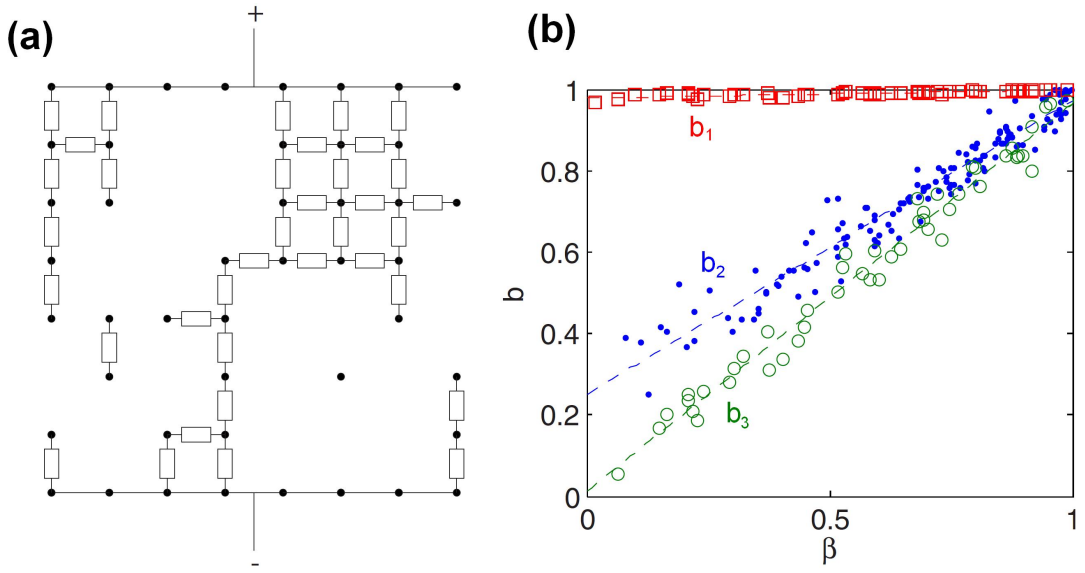

Figure 3.11: (a) Simplified model for percolating cluster films: A resistor network formed by occupying random site on a 2D square lattice. Original simulation were performed for 50×50 lattice. (b) Dependence of b on β. Here b1, b2 and b3 are for power law 1, 2 and 3 respectively.

network of resistors, where each neck is represented by a time varying resistor. The net resistance in such a model shows similar behaviour with respect to time as our experimental results [84].

To generate $G(t)$ data from the simulations various values of β ranging from 0 to 1 were used for individual resistors. This data was then fitted using all three power laws discussed in Section 3.2.3. The values of b determined from fitting results are plotted against the β values used for each simulation run in Figure 3.11 (b). It is clear from the figure that the fitting results from power law 3, β for individual neck that is always the same as b_3 for the whole network. This result indicates that the exponent b determined in Section 3.2.3 for Sn and Pb films also represents the exponent for the coalescence of individual necks in the film. The exponent α of the power for neck growth can be determined by using vales of β found from fittings of experimental data and using values of $\omega = \frac{1}{2}$ (considering bulk scattering) and $\omega = 2$ for grain boundary scatterings as discussed in [45].

3.3 Conclusion

In this chapter coalescence in Sn and Pb clusters was investigated. Sn and Pb clusters were deposited on Si_3N_4 substrates using a UHV-compatible magnetron sputter source. SEM images have shown that these clusters coalesced readily with each other in vacuum. Also, the coalescence was evident from the increase in conductance of the percolating films which was believed to be due to the growth of the necks between adjacent clusters. The conductance variations were used to determined the coalescence rate by fitting the $G(t)$ data of these films to a power law.

Several power laws with different numbers of parameters were fitted but $G(t) = a(t - t_1)^b$ gave the best results. The exponent b determined by the power law is for the conductance data for the whole cluster film with thousands of necks and so simulations [84] were performed to find the link between b and the β for the individual necks. The results showed that the overall resistance evolution of the simulated resistor network follows a power law with exponent b which is similar to the exponent β used for individual resistors.

Using the power law mentioned above β for coalescence of Sn and Pb clusters was found to be between 0.01 and 0.03 which corresponds to $0.01 \leq \alpha \leq 0.06$ for Sn and $0.005 \leq \alpha \leq 0.02$ for Pb. These values are similar to the values determined for Bi (i.e. $0.01 \leq \alpha \leq 0.04$). However these values are much smaller compare to that of reported in literature. It is believed that the smaller exponents is due to fact that the diffusing atoms are locked in the facets formed during the late stage of coalescence as observed in previous KMC simulations at UC.

Chapter 4

Electrical Properties of Sn Cluster Films

4.1 Introduction

According to Moore's law, the number of transistors per unit area of a chip doubles roughly every twenty-four months [1]. However, with the individual transistor size reaching only a few nanometers it is now difficult to keep up with the trend predicted by Moore's law. The way forward is to explore new novel devices which could replace conventional transistors.

This chapter explores the electrical properties of Tin (Sn) cluster films. These devices showed interesting memory and switching behaviour. Percolating films of Sn nanoclusters were deposited on Si/Si_3N_4 substrates using the magnetron sputter source (Section 2.1.3). The conductance evolution at the percolation threshold [33] of the film showed a stepwise behaviour. Interestingly the values of conductance for these steps were very close to the conduction quantum $G_0 = 2e^2/h$ (where e is the elementary charge, h is Planck's constant and G_0 corresponds to the resistance value 12.9 kΩ) [85]. After the end of deposition, a ramping voltage was applied across the films. It was observed that the conductance of these films jumped between various fixed conduction levels. The conductance transitions were found to be both reversible and irreversible. The conduction properties of these films were investigated using different voltages and various electrode configurations.

This chapter can be divided into two parts. The first half contains a literature survey and some theory helpful in understanding the stepping behaviour in Sn

cluster films. The second part of this chapter consists of experimental results, analysis, discussion and conclusion.

4.2 Memristors and Related Devices: A Literature Survey

This section contains a detailed survey of the literature related to memristors and related devices, which show similar switching behaviour to that shown in our cluster films. This section also includes brief introductions to other devices and effects like break junctions, Coulomb blockade, electric field induced surface modifications and electromigration that may be related to the switching behaviour in Sn cluster films.

4.2.1 Memristors

There are four fundamental variables in electrical circuits i.e. current (I), voltage (V), charge (q) and magnetic flux (ϕ). For all six possible pair combinations of these four variables, there is an equation relating them together. Two of these six equations are: time integral of current is equal to charge and time integral of voltage is magnetic flux. The other four equations define four basic circuit elements as shown in Figure 4.1. The resistor, capacitor and inductor are well known. In 1971, Chua theoretically proposed a fourth element called the memristor [86, 87]. A memristor ("memory resistor") is a two terminal circuit element whose value (i.e. memristance) is a function of time and some state variable. Memristance can be defined by the following equation:

$$V = I \cdot M \tag{4.1}$$

and

$$M = \frac{d\phi}{dq} \tag{4.2}$$

Here M is the memristance, which is a function of the quantity of charge passed through it.

It is noteworthy that even before Chua, a three terminal device called a "memristor" was reported as a new fundamental circuit component by Widrow [89]. Since then many devices with memristor like properties were developed showing switching resistance and memory behaviour [90, 91, 92]. These devices were based

on a wide range of structures such as thin metal oxide films [90, 91, 93], phase changing materials [94], conjugated polymers [95] and quantum-well diodes [96].

Strukov et al. [88] have shown analytically that memristors naturally occur in nanoscale systems where ionic transport under an applied voltage varies the resistance of the system. A device was presented in [88] as an example of a memristor. The device was fabricated using a 5 nm oxide film consisting of a layer of titanium oxide (TiO_2) and an oxygen deficient titanium oxide layer (TiO_{2-x}) sandwiched between platinum (Pt) electrodes. When a voltage is applied across the Pt electrodes, the oxygen vacancies act as dopants with 2+ charge which move under the applied electric field. The movement of oxygen vacancies shifts the boundary between the TiO_2 and TiO_{2-x} layers hence changing the resistance of the system.

Figure 4.2(a) shows a model of such a memristive system. The dotted line in the figure represents the boundary between the doped region and the undoped region. The resistance of the device increases because of the wider depletion region when the boundary moves towards the left. On the other hand, if the boundary moves toward the right, the resistance decreases because of the shrinkage of the depletion region. An I-V curve for this device is shown in Figure 4.2(b). Two distinct resistance levels can be seen for the "ON" and "OFF" states of this device.

Memristors are getting a lot of attention in the scientific community because

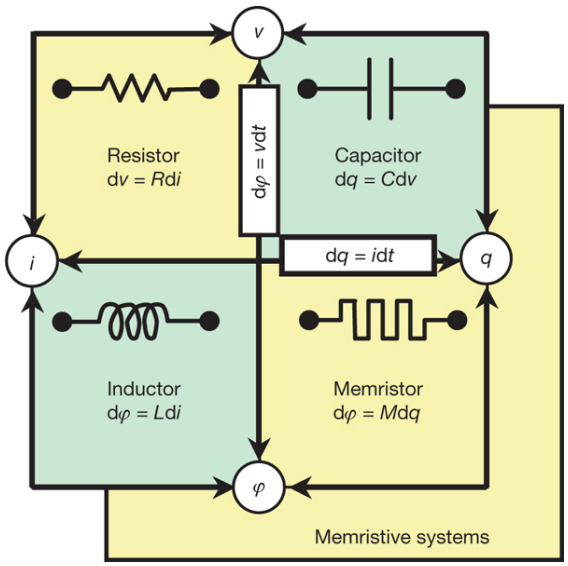

Figure 4.1: Four basic elements defined by four fundamental variables in electrical circuits [88].

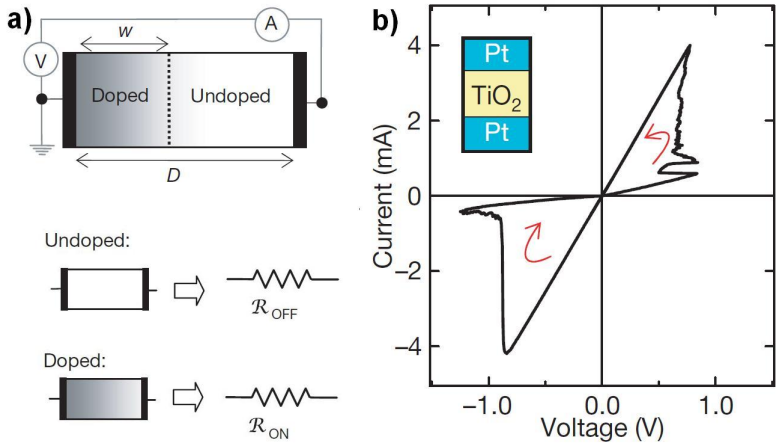

Figure 4.2: Memristor example (a) Equivalent simplified circuit for the Pt-TiO_2-x-Pt device memristive device showing the doped and undoped regions separated by dotted lines (top), along with "ON" and "OFF" states (bottom). (b) I-V plot showing conductance jumps between two discrete resistance levels [88].

of their possible use in non-volatile memories and integrated logic circuits [97, 98]. The advantage of memristors is that they are two port devices with a relatively simple structure compared to conventional CMOS based transistors. Much more compact devices with more condensed elements could be fabricated due to the simplicity of memristive devices. Memristors have also been suggested as a key element in image processing and neuromorphic systems [99].

Various patents have also emerged claiming arrays of two terminal resistance switching devices [94, 100, 101, 102, 103, 104, 105]. Memristor based memories may emerge as a rival to flash memories because of their smaller unit cell size ($\leq$1 nm compare to $\leq$20 nm for conventional flash memories) and ten times higher speed [106].

4.2.2 Quantized Conduction

In 1987 Gimzewski et al. [107] reported a contact resistance of a few kΩ while studying surface modifications induced by a scanning tunnelling microscope tip. They explained the resistance by a Sharvin contact resistance [80] with a 1.5 Å contact area that corresponds to one or two atoms contact. In separate work, Van Wees et al. and Wharam et al. [108, 109] reported that the conduction changes in steps of $2e^2/h$ in two-dimensional GaAs-AlGaAs heterostructures grown using

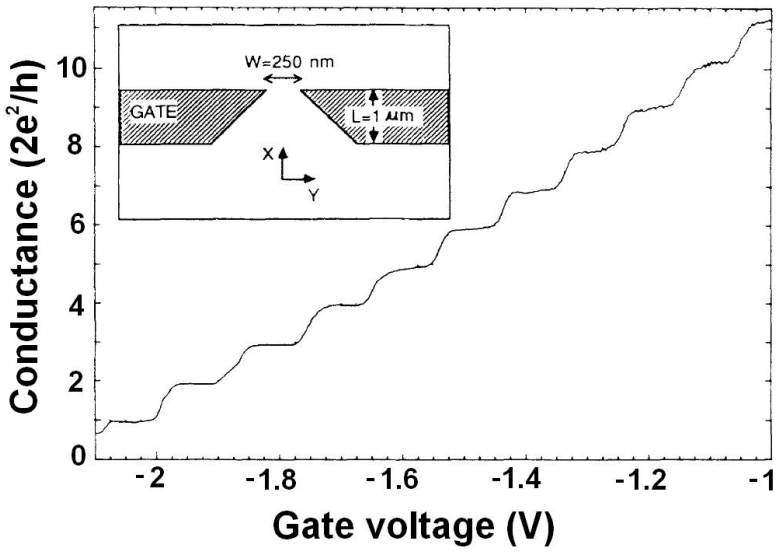

Figure 4.3: Conductance of point contacts as a function of gate voltage showing plateaus at integral multiple of $2e^2/h$. Inset shows the point contact configuration, metallic gate are fabricated on top of GaAs-AlGaAs hetrosturcture deposited by molecular-beam-epitaxy [108].

molecular-beam-epitaxy. Metallic gates were deposited on top of these heterostructures using electron beam lithography, as represented in a schematic in Figure 4.3 inset. An applied voltage on the gate can vary the width of 2DEG (2 Dimensional Electron Gas) in the GaAs-AlGaAs heterostructure. A plot of the conductance variation as a function of gate voltage is shown in Figure 4.3. The conductance curve shows clear plateaus at integral multiples of $2e^2/h$.

Conductance quantization is also observed while breaking metallic wires by stretching them with precisely controlled mechanical systems called mechanically controllable break junctions (MCBJs) [110]. Further details of break junctions are given in Section 4.2.3. STM experiments by Pascual et al. [111] provided evidence for conduction quantization in many metals and the value of conduction quantum was proven to be independent of the metal used. A theoretical proof [85] of conductance quantization is given below.

Quantized conduction behaviour is observed in metallic wires comprising only a few atoms. It is important that electrons should pass through wires ballistically, therefore the length of the pathway should be smaller than the mean free path. Furthermore, if the width d of the pathway is comparable to the Fermi wavelength of the electrons λ_F, only electrons satisfying $\lambda \sim d/N$ can pass through [112],

where N is an integer.

Considering a 1-D electron gas connecting two electron reservoirs with an applied voltage difference of V between them, the density of states is [113]:

$$g(E)_{1D} = \frac{1}{\hbar\pi}\sqrt{\frac{2m}{E}} \tag{4.3}$$

The number of states in the energy interval between Fermi energy E_F and $E_F + eV$ is given by:

$$\Delta n = \int_{E_F}^{E_F+eV} g(E)_{1D}\mathrm{d}E = \int_{E_F}^{E_F+eV} \frac{1}{\hbar\pi}\sqrt{\frac{2m}{E}}\mathrm{d}E \tag{4.4}$$

Or the number of states in a velocity range $\nu_F + \Delta\nu_F$ is given by:

$$\Delta n = \frac{2m\Delta\nu_F}{h} \tag{4.5}$$

The change in kinetic energy due to the applied voltage V can be written as:

$$eV = \frac{1}{2}m(\nu_F + \Delta\nu_F)^2 - \frac{1}{2}m{\nu_F}^2$$

$$eV = m\nu_F\Delta\nu_F \qquad \text{if}\Delta\nu_F \ll \nu_F \tag{4.6}$$

The current flowing between two reservoirs is:

$$I = \Delta n e \nu_F \tag{4.7}$$

Using equation 4.5 and equation 4.6:

$$I = \frac{2e^2V}{2h} \tag{4.8}$$

Hence:

$$G = \frac{2e^2}{h} \tag{4.9}$$

And if N is the number of channels contributing toward conductance:

$$G = \frac{2e^2}{h}N \tag{4.10}$$

According to Equation 4.10 a 1-D electron gas connecting two electron reservoirs exhibits quantized conductance with a value of $2e^2/h$. The percolating Sn cluster films also exhibit quantized conductance which indicates that the width of critical pathways, dominating the overall conductance, may be of atomic size. The results are presented in Section 4.6.6 and 4.7.7 in detail.

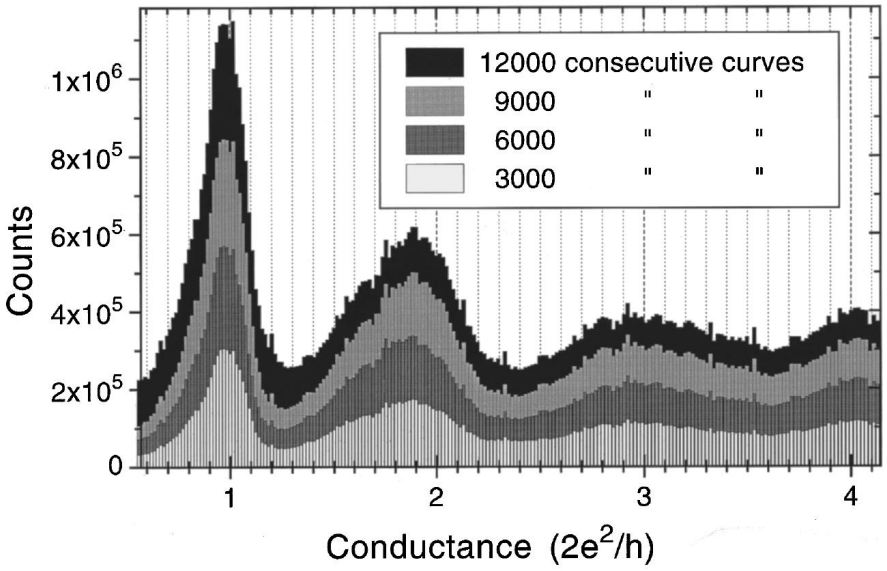

Figure 4.4: Histogram showing the conductance quantization in gold break junctions [123].

4.2.3 Break Junctions

A break junction is an atomic size electrical contact formed during the final stages of the breaking process of a metallic wire. Break junctions can be formed when two metal points are brought into contact and then retracted slowly a few nanometers [110, 112]. The electrical characterization of these contacts or junctions has been under investigation for many decades [108, 110, 112, 114, 115, 116, 117, 118, 119, 120, 121, 122]. It has been found that the electrical conductivity decreases in quantized steps of $2e^2/h$ as the contact width shrinks [114, 112]. Figure 4.4 presents histogram showing clear peaks at integral multiples of $2e^2/h$ in a gold nanowire break junction experiment performed at room temperature. The conduction of Au nanowire break junctions was recorded using a fixed sampling rate. The histogram shown in the figure was constructed by dividing each quantum conduction unit in to smaller bins and counting number of the data points falling in each bin.

The quantized steps can be observed in metallic wires using mechanically controlled break junctions. A schematic of such a junction is shown in Figure 4.5. The pushing rod which is usually a screw pushes up the insulating substrate with a thin metallic wire on top. The wire stretches as the substrate bends due to the pushing rod and finally breaks after forming a single atom contact [110, 112, 116, 124, 125, 126].

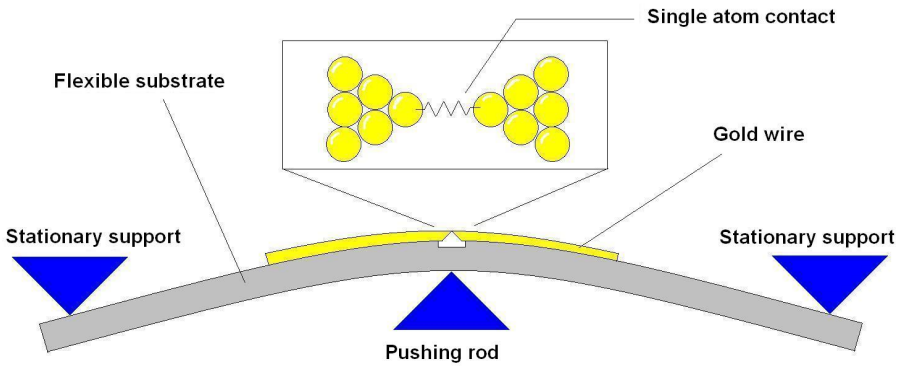

Figure 4.5: A schematic of Mechanically Controllable Break Junction (MCBJ).

Figure 4.6 shows break junction data for Pb and Sn. The histograms present data gathered from more than ten thousand individual conductance traces recorded using 100 mV bias at 4.2 K temperature. The data shows peaks at $1G_0$ and $2G_0$ after fitting the results to Gaussian curves [127].

Also, a step-wise deformation of the contact and atomic rearrangement plays an important role in the step-wise conduction variation in break junctions [118]. These atomic rearrangements take place in a sequence of structural transformations from one stable atomic geometry to another. The jumps in conduction curves observed in break junctions can be correlated to these atomic rearrangements. The deformation and atomic rearrangements of the metallic wire structure finally leads step by step to form a single atom contact showing quantized conduction.

Scanning Tunnelling Microscopes (STM's) have also been used to study break junctions. Break junctions can be formed when an STM tip is brought into contact with a substrate of the same metal as the tip and then retracted slowly. Agräit et al. [114] used STM to study the quantized conductance steps at low temperature. The current through Pb and Au samples was analyzed while varying the tip to sample distance up to 14 Å. The "jump to contact" phenomenon was observed at 2 Å where the resistance changed from $0.06G_0$ to $1G_0$ after the contact was established.

As indicated in the previous section, the Sn cluster films exhibit quantized conduction. Formation of break junction like structures in cluster films provides a reasonable explanation for the quantized stepping behaviour. The results are presented in Section 4.4.

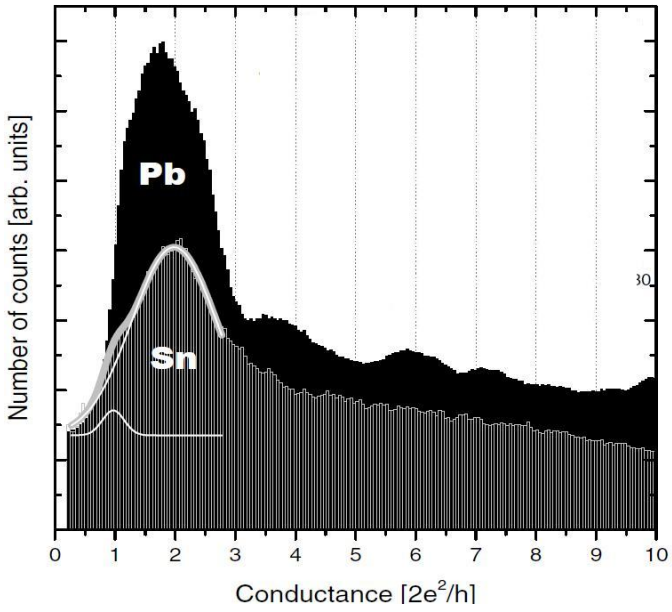

Figure 4.6: Conductance histogram for Pb and Sn break junctions showing peaks at $1G_0$ and $2G_0$ in Gaussian fitting curves [127].

4.2.4 Coulomb Blockade

If we charge a nanoparticle by adding a single electron to it, the change of the electric potential due to this charging will be e/C. If the capacitance C is very small, the potential U built due to charging can be enormous and can prevent addition of another electron. The difficulty of putting any further charge on such a particle is exhibited as an increase in the resistance of the of the tunnel junction.

If we consider a nanoparticle as an isolated spherical capacitor with a capacitance of $C = 4\pi\epsilon_0 R$, where R is the radius of the nanoparticle, the energy required to add a single electron with charge e to this capacitor is:

$$E_c = e^2/2C \tag{4.11}$$

Now let us extend this hypothetical isolated island model to a more realistic capacitor like system where the nanoparticle is situated close to a source electrode separated from the particle by a tunnelling barrier. In such a case electrons can tunnel from the source to the particle and vice versa, and the Coulomb blockade could only be observable if the thermal energy of electrons is smaller than the charging energy i.e.

$$k_B T < E_c = e^2/2C \tag{4.12}$$

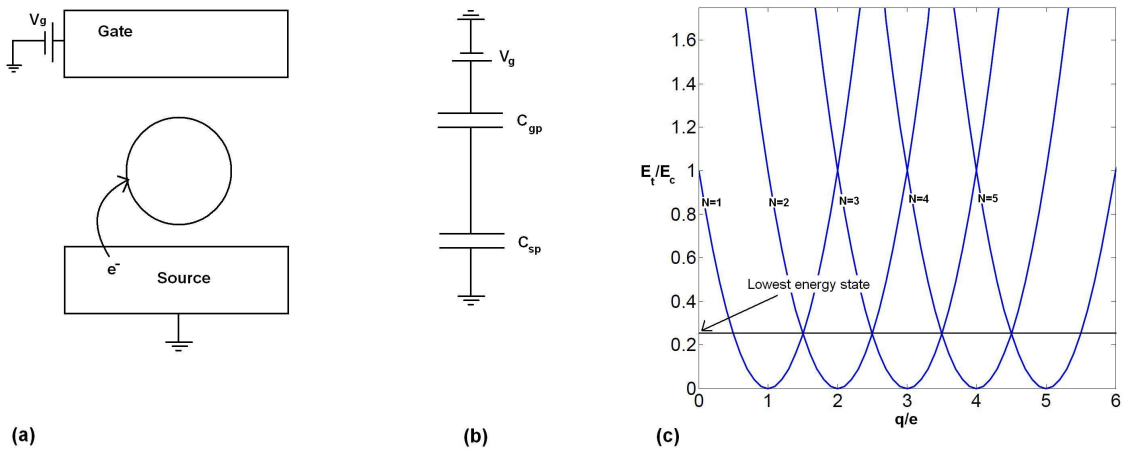

Figure 4.7: (a) A simple Coulomb blockade circuit along with (b) Equivalent circuit. (c)The charging energy variation of the single-electron box depending upon the charge induced by gate voltage $q = C_{gp}V_g$.

here k_B is Boltzmann constant and T is the absolute temperature [128].

Using the Heisenberg uncertainty principle $\Delta E \Delta t > h/4\pi$ where ΔE is equal to the E_c given in equation 4.12 and $\Delta t = RC$ for a Resistor-Capacitor system, the resistance of the tunnel junction required for observing the Coulomb blockade should be:

$$R > h/e^2 = 25813\Omega \tag{4.13}$$

The scenario of an isolated nanoparticle presented above can be further extended by adding a gate electrode to give Coulomb blockade circuit some functionality (see Figure 4.7(a)). This simple Coulomb blockade circuit can be represented by the equivalent circuit shown in Figure 4.7(b). The electrostatic energy of the system is given by:

$$E_t = E_c \left(N - \frac{q}{e}\right)^2 \tag{4.14}$$

where

$$E_c = \frac{e^2}{2(C_{gp} + C_{sp})} \tag{4.15}$$

and C_{sp} and C_{gp} are the capacitances of source and particle and gate and particle junction, N is the number of excess elementary charge on the particle and q is the charge induced by the gate voltage.

Figure 4.7(c) shows the plots of E_t vs. the induced charge by the gate voltage. For each value of N we get a parabola shifted by a value q/e. The solid line intersecting the parabola shows the lowest energy level of the system. The plot

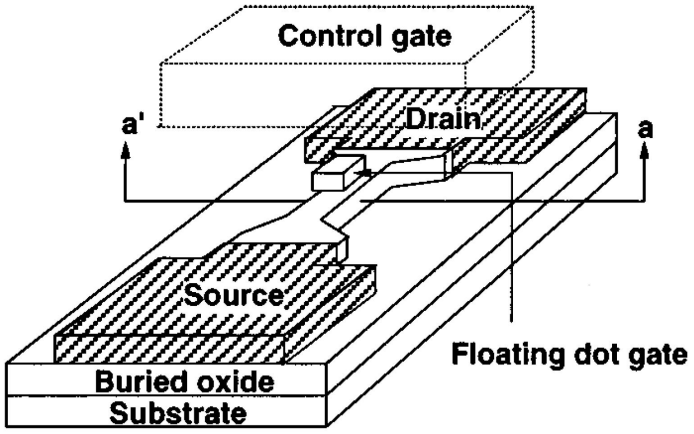

Figure 4.8: A floating gate single-electron memory device. [130].

shown in Figure 4.7(c) indicates that by varying the gate voltage, the number of excess charge on the particle can be controlled.

The concept of Coulomb blockade has been employed in designing single electron devices. In the past two decades single electron transistor and memory devices have been reported widely in the scientific literature [129, 130, 131, 132, 133]. Figure 4.8 shows an example of a memory device utilizing a floating gate single electron transistor. A single electron can be transferred from the control gate shown in the figure to the floating dot gate by tunnelling. The electric field produced by the charging of the floating gate can alter the source-drain current.

4.2.5 Electromigration

Electromigration is mass transport in a conductor due to the momentum transfer from conduction electrons to the lattice atoms. The following equation [134] gives the mass transport flux due to electromigration in a polycrystalline metal film:

$$J_{em} = C_b \frac{D_b \delta}{k_B T d} Z_b^* e E \tag{4.16}$$

where C_b, δ, Z_b^* and D_b are concentration, effective width, charge number and diffusion coefficient of grain boundaries. d, T, E and k_B represent the diameter of the grains, temperature, applied electric field and Boltzmann constant respectively.

Electromigration becomes significant in micro and nanostructures where even a small amount of mass transport can cause device failure. Electron current densities of $\sim 10^8$ A/cm^2 and $\sim 2 \times 10^4$ A/cm^2 are sufficient to produce electromigration

in gold [135] and tin [136] respectively. Electromigration can be used to fabricate nanogaps which can be used to examine the material properties at the nanometer scale [137, 138, 139, 140, 141]. Quantized conduction exhibited by nanogap formed by electromigration has also been reported [135]

4.2.6 Electric Field Induced Surface Modifications

Intense applied electric fields can modify metallic surfaces [142, 143]. Mechanisms such as electric field induced emission and migration have been used to explain the surface modification due to an electric field in STMs [143, 144, 145]. Electric field induced emission occurs when a sharp tip is brought close to a metallic surface at a distance of few nanometers and an electric field of few V/Å is applied across the gap. The atoms from the surface are ionized and are ejected out of the metallic surface. Also, the applied electric field can induce atomic surface migration on the tip [142].

Electric field induced surface modifications have also been observed in nanogaps formed in nanowires and thin films [146, 147]. Figure 4.9(a) shows a nanowire with a nanogap formed by an electromigration process [146]. After the application of an applied voltage (in this case $\sim$ 2.5 V) a nanocontact is formed due to electric field induced surface modification. The connection can be created and destroyed many times by applying voltage in a controlled fashion. Figure 4.9(b) shows SEM micrographs of a gold film deposited on Si_3N_4 substrates separated by a 70 nm gap with a large undercut beneath to prevent electrical contact between two separated parts of the film. Due to application of a voltage (10 V) the grain shown in Figure 4.9(b) pulled a gold atom protrusion from the thin film on the right side of the slit creating a conduction path way [147]. A switching device can be realized using field induced evaporation and electromigration as the conduction path can be formed and broken multiple times using these phenomena [146].

4.2.7 Ion Transport Due to Solid State Electrochemical Phenomenon

Mixed conductors [148] such as Ag_2S whose conduction depends on the transport of both ions and electron/holes have been used to form nanostructures using electrochemical processes similar to the one shown in Figure 4.10. When an electric

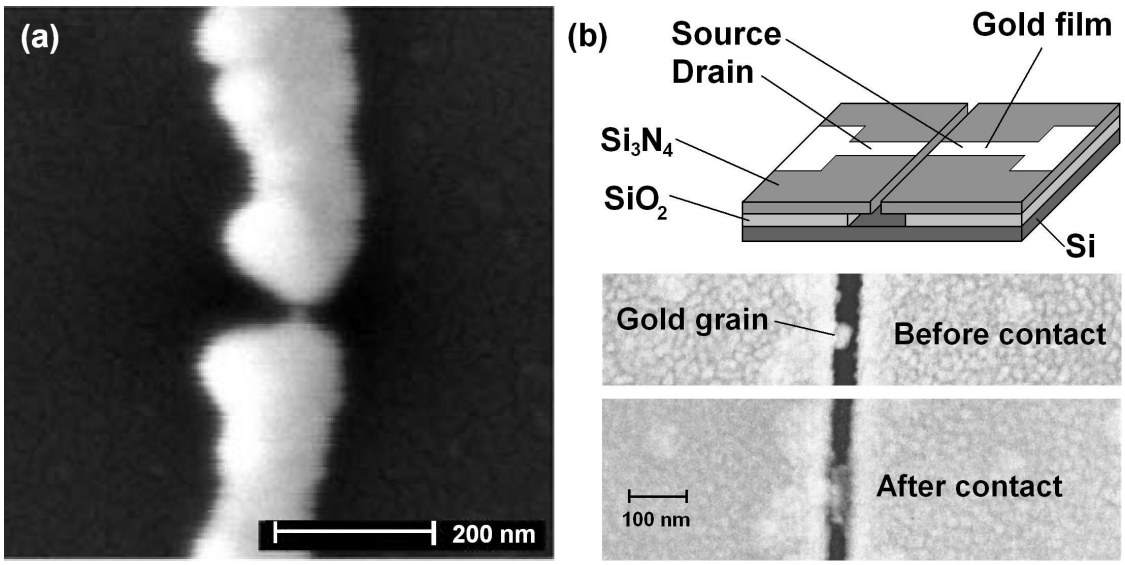

Figure 4.9: (a) Nanocontact formed between a nanogap in gold nanowire [146]. (b) Top: Schematic of lithographically prepared substrate with an undercut and with a deposited god thin film. Bottom: SEM of nanocontact formed between two gold thin films due to an applied voltage pulse [147].

potential is applied across an Ag_2S STM tip and a platinum (Pt) substrate, Ag^+ ions migrate within the tip in the direction of the applied electric field. An Ag protrusion is formed at the end of the STM tip when a negative potential is applied to the substrate. The protrusion disappears when a positive potential is applied to the substrate [149].

Substantial Ag ion migration due to application of an electric field in Ag_2S has also been reported in nanowires [150, 151]. Crossbars of Ag_2S and Pt nanowires, with a gap of 1 nm between them, act as an electrical switch when an electric field is applied. If a positive potential above a certain threshold is applied to Ag_2S a protrusion similar to the one shown in Figure 4.10 is formed in the gap between the Ag_2S/Pt crossbars due to Ag ion migration and an electrical contact is formed between the crossbars. The electrical contact between the crossbars due the Ag protrusion is broken once a negative potential above a threshold is applied to the Ag_2S nanowires.

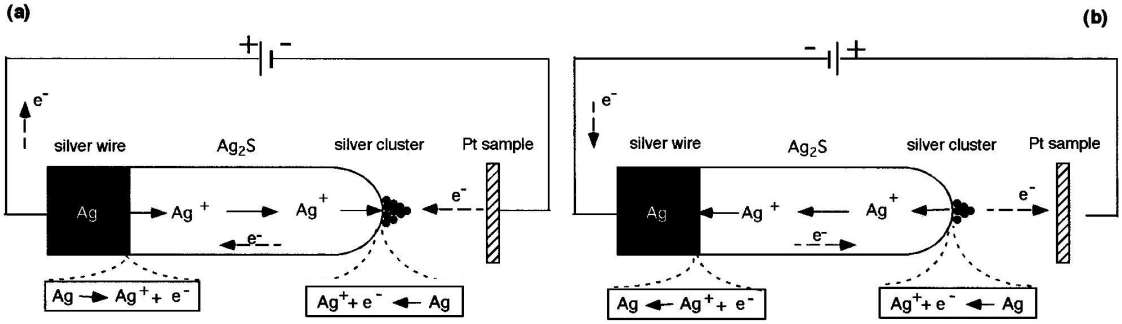

Figure 4.10: (a) Growth of Ag protrusion on top of Ag_2S STM tip when a negative voltage is applied to the sample due to solid state electrochemical reaction. (b) Shrinkage of the Ag protrusion on the STM tip due to a positive biased sample [149].

4.2.8 Discontinuous Films

Discontinuous films are metallic thin films consisting of island structures deposited on insulating substrates. The island size in the discontinuous films ranges from a few nanometers to a few hundred nanometers, with $\leq$ 10 nm gaps [152, 153]. It was observed that such discontinuous thin films show interesting properties which make these films suitable for applications like gas sensors and strain gauges. Also, stable and reproducible switching has been reported in such discontinuous thin films [154]. Kiesow et al. [155] have reported reversible switching behaviour of plasma polymer[1] films with embedded silver particles (see Figure 4.11).

Figure 4.11 shows I-V curves for different films with different filling factors f (ratio of area covered by silver nanoparticles to the total area). Films with f values other than 0.78 followed Ohms law whereas the film with $f = 0.78$ showed abrupt jump in current of about 6 orders of magnitude.

Figure 4.12 shows voltage ramp of a film showing switching behaviour. The switching behaviour is highly reproducible and so it seems difficult to explain it by models based on structural changes (such as conductive path formation due to coalescence of individual particles/islands and formation of thermally induced filament like conductive carbon paths in the polymer[155]. Kiesow et al. proposed that field emission of electrons between metallic nanoparticles could explain the reversibility.

[1]Polymer formed using plasma polymerization where monomers are activated, for polymerization, using a gas discharge or plasma. In [155] hexamethyldisilazane monomers were polymerized using 50 Hz plasma.

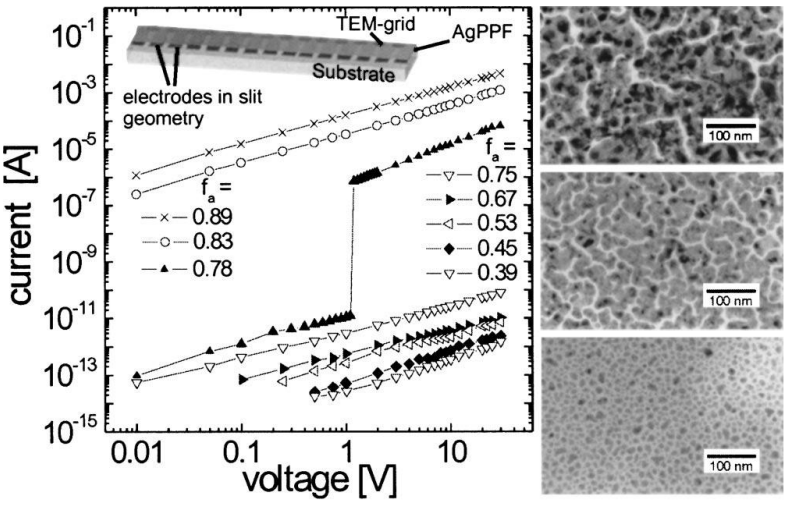

Figure 4.11: I-V plots of plasma polymer thin films with different filling factors f of silver nanoparticles. For $f = 0.78$ a stepwise change in resistance can be seen [155].

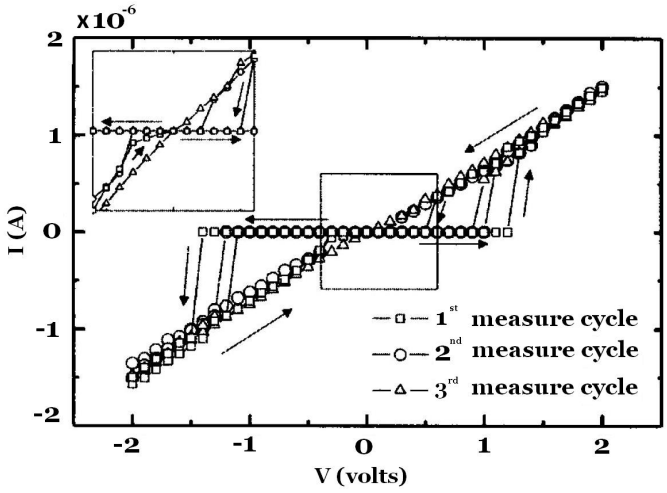

Figure 4.12: I-V plots of plasma polymer thin films with silver nanoparticles showing reversible switching behaviour [155].

4.3 Summary of Previous Research at UC

Investigation of the electronic properties of Bi Cluster thin films and nanowires has been a focus of interest at UC cluster group [41, 156, 16]. An IGA source [16] was used to produce Bi clusters of 20 to 30 nm diameter. These clusters were deposited between Au/NiCr electrodes on Si_3N_4 surface prefabricated by photolithography and EBL. To characterize the Bi devices, I-V curves were obtained at room temperature, liquid helium and liquid nitrogen temperatures for a large number of samples. It was observed that these Bi cluster films showed steps [156] in conductance.

After the deposition of the cluster films I-V characteristics were studied by applying a voltage between the prefabricated electrodes. For low resistance cluster films, measurements were done at room temperature. It was found that the film resistance changes in step-wise fashion as the applied voltage was swept from zero to 3 volts (see Figure 4.13). No steps in resistance were observed when the voltage was ramped back to zero. The steps were observed at the same voltage for a couple of scans for one of the films. It was also observed that there are certain reproducible resistance levels present during the voltage scans. The resistance step size was of the order of few kΩ. The reason for these steps might be the reordering of conduction paths or changes in the types of connection between the clusters.

The resistance of the cluster film was modified after each voltage scan. The resistance jumped to new stable values in a step-wise fashion at certain voltages. According to Gourley [41] The variation in resistance could be due to phenomena like electromigration and coalescence causing modifications in critical necks. Another possible explanation may be the reordering of the clusters due to high electric field causing them to make new temporary connections which may later on fuse and sinter due to high current densities. It is also possible that a combination of these processes is the reason behind the step-wise behaviour.

For some samples, a voltage dependent transition in resistance was observed. When the voltage was increased to a critical value, the resistance of the film decreased to a lower state and remained there until the voltage decreased below the critical value. Figure 4.14 shows I-V characteristics of a V-groove self-assembled nanowire [42]. The steps observed were reversible as the conduction of these nanowires switched to a higher conductance when the applied voltage reached a value of 1.9 V and the conductance returned to its original value at -1.8 V.

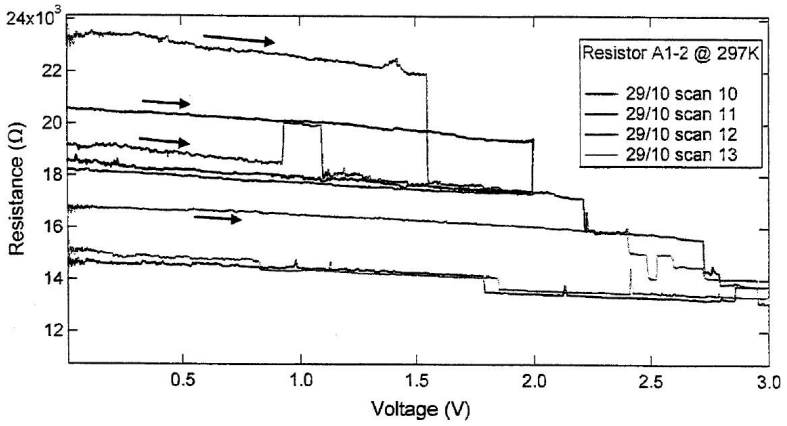

Figure 4.13: Voltage scans for cluster film samples of resistance of the order of few kΩ at room temperature showing step behaviour [41].

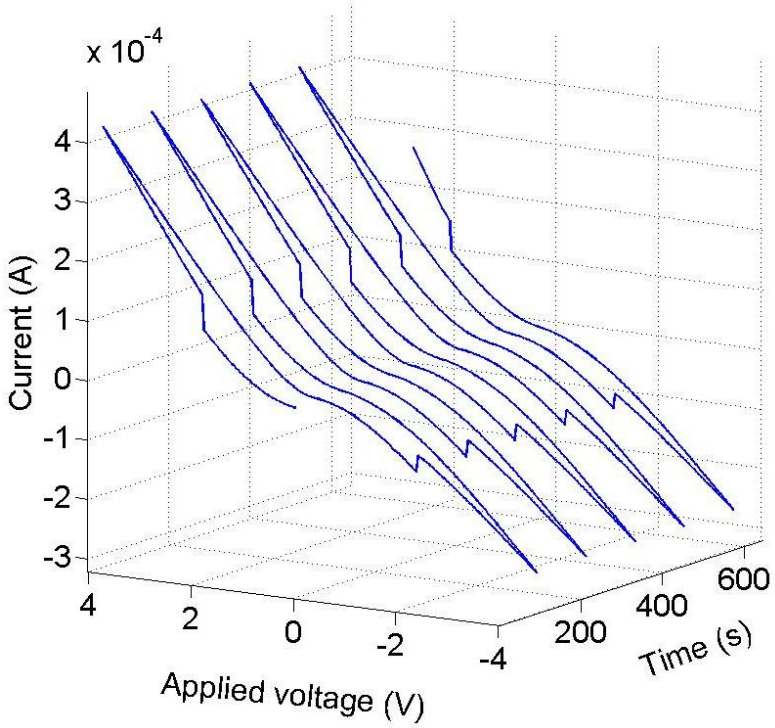

Figure 4.14: IV characteristics of a V-groove self-assembled nanowire. Reversible steps in conductance can be seen at 1.9 V and -1.8 V during the voltage ramp [42].

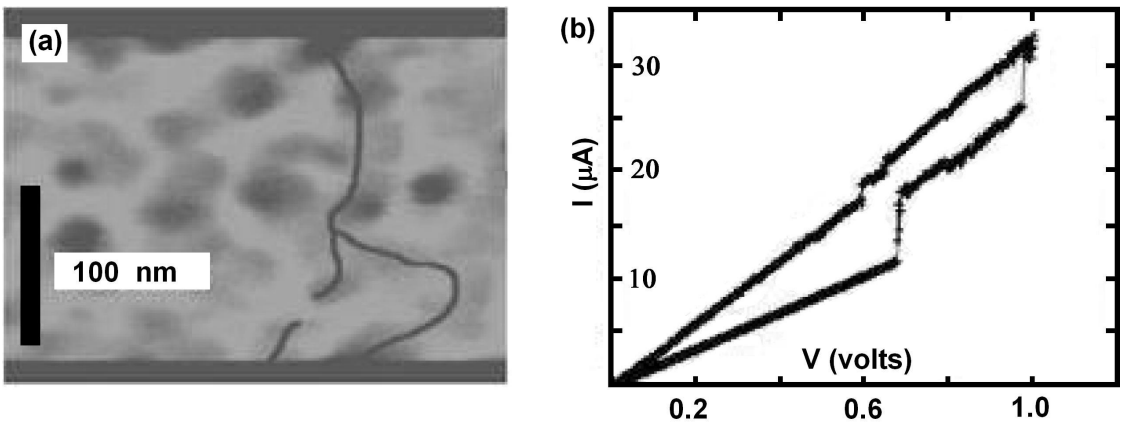

Figure 4.15: Nanowire formed by conducting clusters (b) I-V curve showing discrete resistance steps in Bi cluster film [157].

Reversible and irreversible step-wise behaviour in conductance of Bi cluster thin films and nanowires was observed due to the applied voltage. The step-wise conductance variation could be due to any one or a combination of the phenomenon discussed in Section 4.2.1. The irreversible steps could be attributed to permanent structural changes in the conducting paths due to processes like electromigration and coalescence. The reversible conductance steps can be explained by Coulomb blockade, electric field induced surface modification and electromigration.

Corbett et al. [157] has proposed a model in effort to explain the jumps in conductance values. An example of such conductance jump behavior shown by percolating Bi cluster films is shown in Figure 4.15(a). These film show conductance variation in steps due to voltage variation across them Figure 4.15(b). In these percolating films there is a possibility of many parallel conducting paths being formed during the deposition. The overall resistance between the electrodes is due to the collective effect of all these pathways. There could be some pathways which may be open somewhere in the middle similar to one shown in Figure 4.15(a). Corbett et al. [157] proposed a model based on electro-mechanical condition and relaxation of these nanowire-like structures.The proposed model consists of two parallel nanowire-like conducting pathways. One of the pathways consists of two filament like structures with a gap of length d between them. The filament-like structures (see Figure 4.16)act as an RC circuit and when a voltage is applied across them an opposite charge is built up on both ends. An attractive electrostatic force between the oppositely charged filaments results in reduction of the gap and

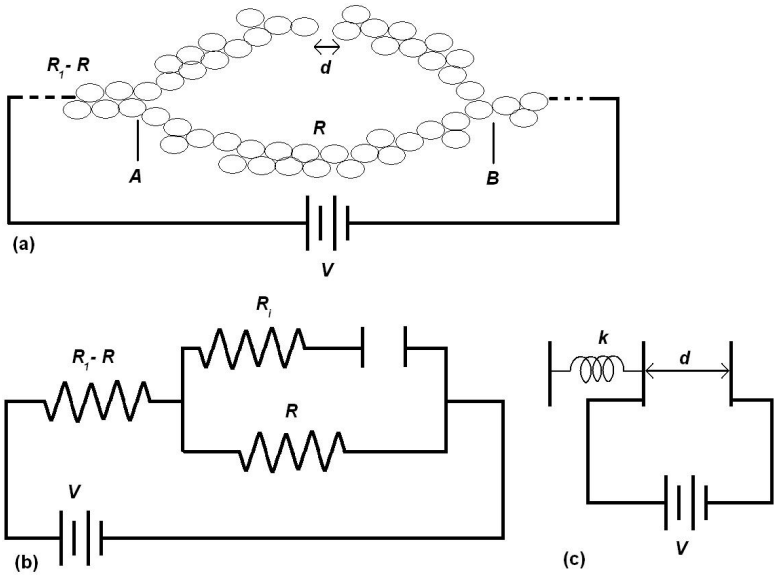

Figure 4.16: Proposed electro-mechanical model to explain step-wise conductance behaviour in Bi cluster films: (a) Two filaments are connecting point 'A' and 'B'. One of the filaments is broken in the middle and has a gap of width 'd'. (b) An equivalent RC circuit for the model presented in (a). A charge could built up across the gap which can produce an attractive force to connect both ends. (c) The arms of broken filaments can act as rigid cantilevers with spring constant 'k' and tend to pull apart from each other after the charge responsible for the attraction is neutralized due to electrical connection. [157].

ultimately formation of an electrical connection between the ends. The formed electrical contact could fuse together due to melting even after the charge stored is neutralized. An equivalent circuit for this resistor-capacitor system is shown in Figure 4.16(b).

4.4 Experiments for Characterization of Sn Cluster Films

So far in this chapter the devices showing switching behaviour have been introduced. Also phenomena related to the switching behaviour have been explored. From here on the experimental results for electrical characterization of Sn cluster films are presented. Over two hundred samples were prepared and analysed during the course of experiments. Sn cluster films showed interesting quantized conduc-

tion steps during and after the end of deposition. These steps were found to be both reversible and irreversible and are discussed in Section 4.7.5 and 4.7.6. In Section 4.7.8 a detailed analysis and discussion is presented exploring the origins of the conductance steps in Sn cluster films.

4.4.1 Source Characterization

The cluster beam properties were tuned using various source parameters e.g. aggregation length, sputter power, nozzle-skimmer alignment, pressure in the deposition chamber and inert gas flow rate (Section 2.1). The cluster properties such as size and ability to coalesce, after deposition on a substrate, vary dramatically even with slight changes in the source conditions.

During the experiments a leak in the vacuum system was discovered which was later fixed. All the samples prepared for the electrical characterization of Sn cluster films can be divided into two groups i.e. Batch 1: samples deposited with the leak in the system and Batch 2: samples deposited after the system leak was fixed. The cluster film morphology was different for Batch 1 and Batch 2. Figure 4.17 shows that the cluster films of Batch 2 are highly coalesced compared to Batch 1. Oxygen present in the system due to the leak can form an oxide shell around the clusters produced in the source chamber. This oxide shell can hinder the coalescence process after the clusters were deposited on the substrate.

Experiments to deposit Sn cluster devices were performed under various conditions. Typical source conditions used in the experiments are presented in the Table 4.1. A range of values for sputter power, aggregation length and system pressures are given in the Table 4.1 to elaborate the variations in system condition.

Figure 4.18 shows an example of the time evolution of the mass spectrum of Sn clusters produced using the sputter source. The source pressure decreased with the passage of time, and reached an equilibrium state in a time span of $\sim 6 \times 10^3$ s. As the source pressure decreased the full width of half maximum of the mass spectrum decreased and the peak of the spectrum shifted toward bigger diameters. Figure 4.18(a) shows that fewer clusters were produced at higher pressures which could be an indication of the fact that the system is contaminated with residual gases like O_2 and N_2, hindering the aggregation process [158].

Figure 4.19 shows a summary of characterization experiments for the Sn clusters produced by the sputter source (Section 2.1.2) for conditions similar to those

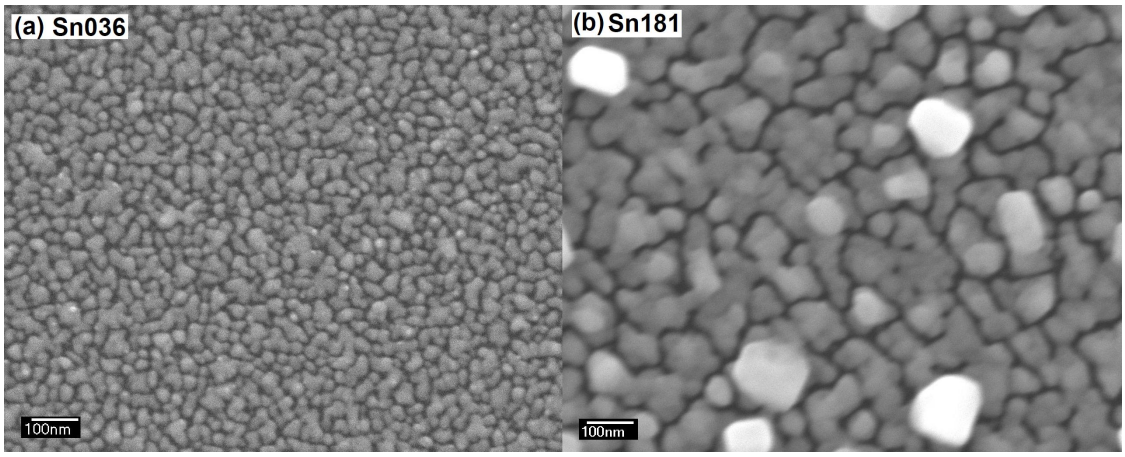

Figure 4.17: Comparison of Sn cluster film morphology before and after leak in the deposition system was fixed. Sample from Batch 1 (with leak in the system) (a) shows much less coalescence compare to the samples from Batch 2 (after the leak was fixed) (b) showing huge amount of coalescence.

Parameter	Value
Argon flow rate	100 sccm
Sputter Power	15-25 W
Aggregation length	8-13 cm
Mass analyzer chamber pressure	1×10^{-5} to 1×10^{-4} Torr
Deposition chamber pressure	$<1 \times 10^{-5}$ Torr
Nozzle dimensions	3 mm (diameter)

Table 4.1: Typical experimental conditions used for Sn cluster deposition.

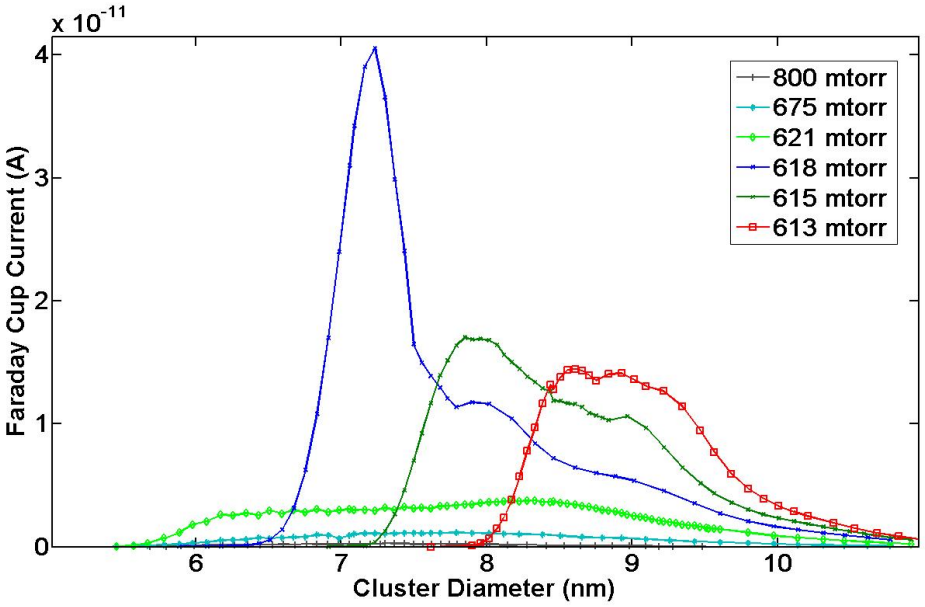

Figure 4.18: Mass spectra for different source pressures. The peak of cluster diameter shifts toward bigger diameter with decrease in source pressure.

described in Table 4.1. It was found that the deposition rate[2] can be increased by simply increasing the sputter power, which is simply due to the fact that more material was sputtered at higher power. Figure 4.19(a) and (b) show a comparison of deposition at 20 and 25 W sputter power. It can be seen that there is always a critical aggregation length below which there is no measurable cluster production. The deposition rate also depends on the inert gas flow rate. The maximum deposition rate can be achieved around 100 sccm flow rate of Ar gas. It was observed that the deposition rate dropped when the flow rate is either too high or very small.

Any variation in the source conditions can alter the cluster size. Figure 4.19 (c) and (d) show the variation in average cluster size due to change in aggregation length and Ar flow rate. The average cluster size increases due to an increase in the aggregation length, as the clusters will have more time to grow before leaving the source chamber (Section 2.1.3). Figure 4.19(e) shows that the cluster size distribution was shifted towards bigger sizes with increase in aggregation length at 60 sccm flow rate. On the other hand, at a flow rate of 90 sccm the mass spectra developed a second peak representing clusters of bigger diameter (see Figure

[2]The deposition rate is measure of total mass reaching the FTM per unit time irrespective of the mass distribution of the clusters.

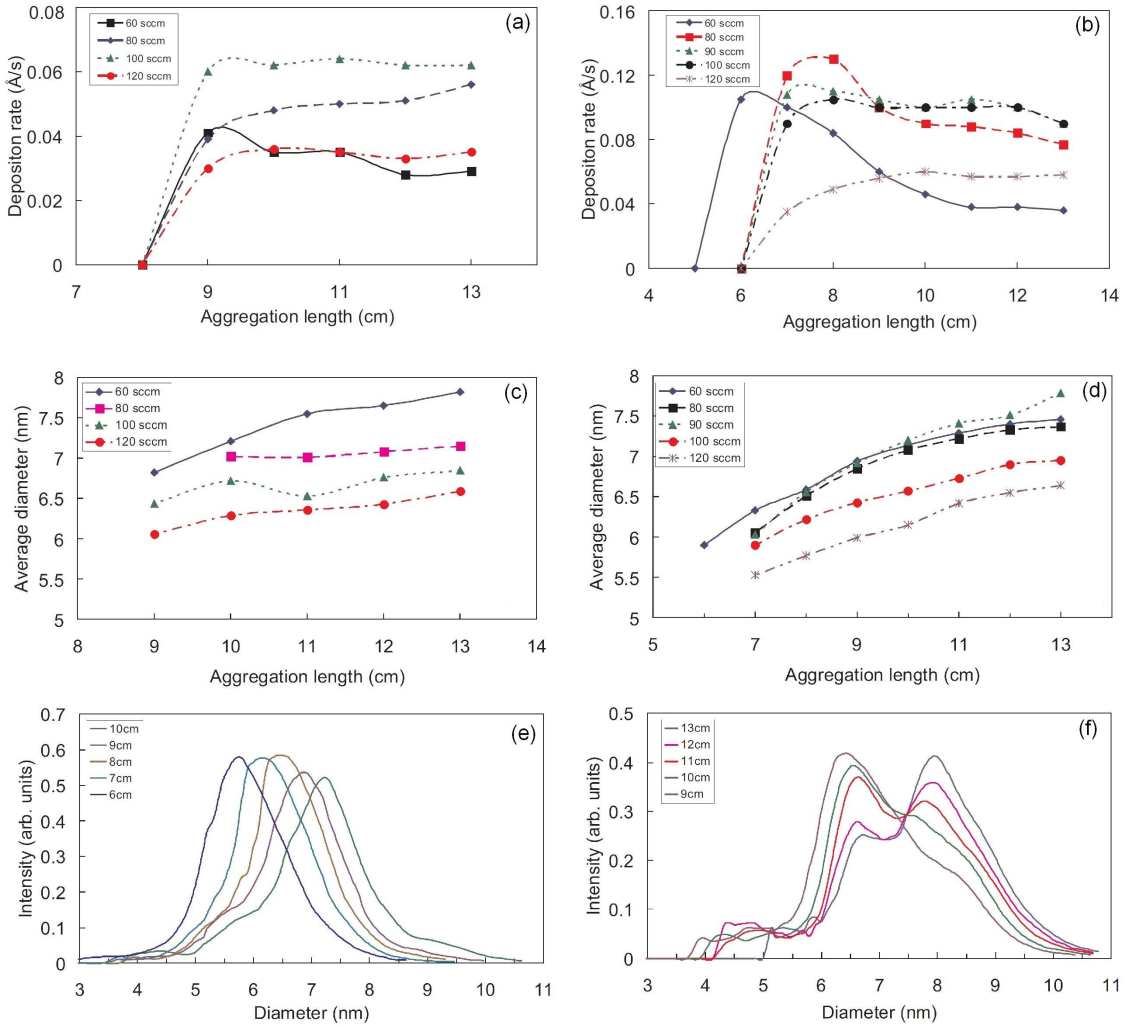

Figure 4.19: The Source Characterization for Sn clusters (a) Dependence of deposition rate on aggregation length using various flow rates of Ar and 20 W sputter power. (b) Dependence of deposition rate on aggregation length using various flow rates of Ar and 25 W sputter power. (c) Dependence of average diameter of Sn clusters produced using various flow rates of Ar and 20 W sputter power. (d) Dependence of average diameter of Sn clusters produced using various flow rates of Ar and 25 W sputter power. (e) Mass spectra of Sn clusters produced using various aggregation length (sputter power=25 W, Ar flow rate=60 sccm. (f) Mass spectra for Sn clusters produced using various aggregation length (sputter power=25 W, Ar flow rate=90 sccm) [159, 160].

4.19(f)). These bigger clusters were produced due to the aggregation of smaller clusters [159, 160].

4.5 Effect of Deposition Chamber Pressure on Conduction Evolution

Electrical properties of cluster films are not only affected by the source chamber conditions but also by the quality of vacuum in the deposition chamber. The pressure in the deposition chamber was varied by inducing an air leak by a precision needle valve. Three samples 'a', 'b' and 'c' were prepared under the same source conditions. As usual, the chamber was pumped continuously during the experiment using a turbo pump. The conduction evolution for these samples is shown in Figure 4.20. The deposition chamber pressure for the 'a', 'b' and 'c' samples was maintained at 5×10^{-6}, 1×10^{-5} and 5×10^{-5} Torr respectively. These pressures correspond roughly to an exposure of ∼1,2 and 10 Langmuir per second to oxygen which mean formation of ∼1,2 and ML in 1 s time assuming that every gas molecule sticks to the surface on its collision to the surface of the sample.

For all three samples shown in Figure 4.20, a sharp decrease in the conductance was observed right after the end of deposition which was due to coalescence in the cluster film. All these samples have film thickness very close to the critical thickness required for percolation. Hence after the end of deposition any coalescence tends to reduce the area coverage further, which causes a decrease in overall conductance. The sharp decrease in conductance after the end of deposition was much more visible in sample 'a' that was deposited with deposition chamber pressure 5×10^{-6} Torr. The conduction of sample 'a' decreased monotonically to zero much more quickly compared to the other two samples deposited at higher pressures.

Sample 'b' with pressure 1×10^{-5} Torr was more stable compared to the first sample and showed conduction steps (both upward and downward) and after some time, the conduction eventually reached an open circuit state. After the end of deposition, sample 'c' showed a smaller decrease in conductance compared to sample 'a' and 'b'. However after 3000 s, the conductance of sample 'c' decreased in steps similar to sample 'b'. The stability of sample 'c' can be attributed to the reduction of coalescence due to formation of an oxide shell around the clusters.

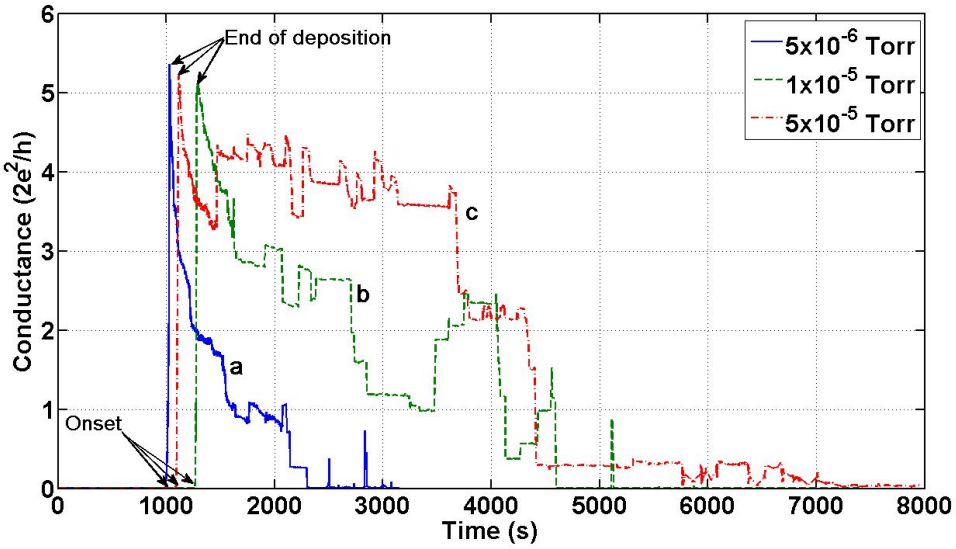

Figure 4.20: Conduction evolution for samples deposited at three different deposition chamber pressures. Samples deposited on relatively higher pressures show more stable conductance response.

The samples discussed above have been deposited during a single run with identical source conditions. The effect of ambient gases, changing the film morphology and conductance behaviour, is very important to understand in order to fabricate stable devices showing useful conductance switching behaviour. However more work is needed for a comprehensive understanding of this phenomenon and to find out ideal conditions for stable cluster devices.

4.6 Conduction-Onset Step Behaviour

As the Sn nanoclusters are deposited, the ratio of the area covered by the nanoclusters to the total area between the electrodes, increases. At the point where the total coverage reaches the percolation threshold an electrically conducting path is formed. Just before the contact between the two electrodes is formed (at the percolation threshold), the conduction of the cluster film jumps from open circuit to tunnelling regime (see Figure 4.21 for an L2 sample). A steep increase in the current represents the onset of conductance at the tunnelling percolation threshold (∼1400 s) followed by the true[3] percolation threshold at ∼1500 s after which the

[3]Conduction through a physically connected path

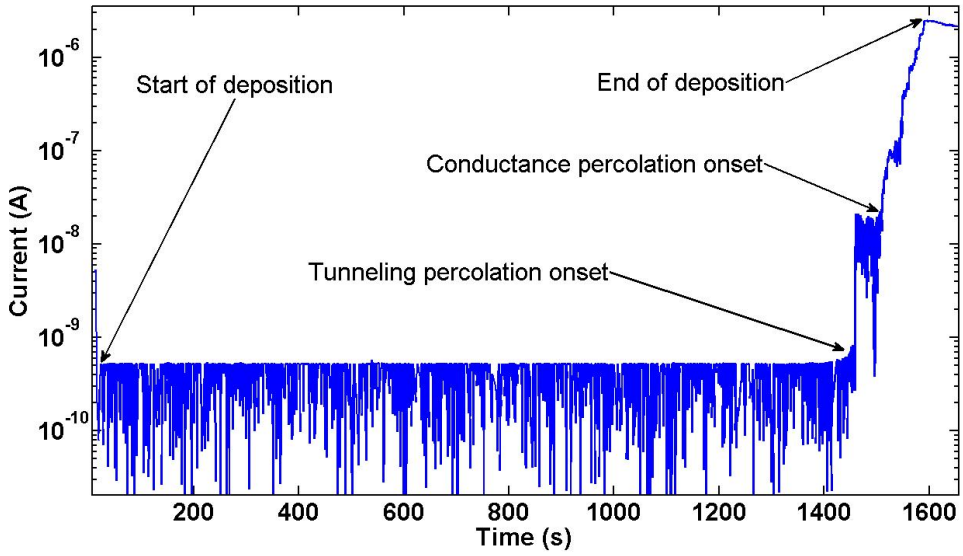

Figure 4.21: Current evolution for Sn cluster deposited on L1 type samples. The steep increase in current at ∼1400 s represent onset of conductance when the tunnelling percolation threshold is achieved followed by the contact percolation threshold at ∼1500 s.

conductance kept on increasing until the deposition was stopped.

It has been observed that the conduction onset behaviour varies from sample to sample depending on factors such as source conditions and the substrate surface properties. Sample to sample variation in conduction behaviour of the individual cluster films makes it really hard to see any correlation of the electrical properties of the films to the source condition or film morphologies. However after the careful analysis of more than two hundred samples a pattern began to emerge showing four main categories of the sample according to their onset behaviour. The four samples categories are as follows:

1. Category A: Smooth onsets.
2. Category B: Onsets with steps of the order of $1G_0$
3. Category C: Onsets with steps of the order of $\sim 5G_0$.
4. Category D: Onsets with steps of the order of $>10G_0$.

Table 4.2 shows the important properties of the samples in each of these categories. Figure 4.22 shows average critical thicknesses plotted versus average deposition rate for all sample categories. Higher film thicknesses are required to achieve

Category	Total Number of Samples	Deposition Rate Å/s	Critical Thickness (nm)	Source Pressure (mTorr)	Grain Size* (nm)
A	61	0.08±0.02	80 ±30	640±50	20±20
B	67	0.12±0.02	170±70	630±50	40±30
C	28	0.18±0.03	230±50	610±50	70±30
D	40	0.35±0.09	280±90	600±50	90±40

Table 4.2: Summary of parameters used for different conduction-onset categories. Values shown are average for all the samples in a corresponding category along with the standard deviation. Mean cluster diameters of 7.5±2 nm were used for all the sample categories. *Note: The Sn cluster films were highly coalesced and the grain sizes were measured using the technique explained in Section 2.7.

percolation for samples deposited at higher deposition rates. The target deposition rate for most of the experiments was 0.1 Å/s. however due to uncontrolled source parameters the deposition rate varied between the range of values shown in Table 4.2.

During the deposition Sn nanoclusters land randomly on the substrate, some of them fall on empty spaces while others fall on top of previously deposited clusters. Any clusters landing on top of other clusters or landing beside already deposited clusters will tend to coalesce. During the coalescence process incoming clusters are consumed in forming particles with bigger diameters and hence increasing the average thickness of the film and contributing less towards increasing the surface coverage. The surface coverage required for the onset can be achieved for smaller numbers of clusters deposited if there is less coalescence.

It is possible that the formation of oxide/nitride shell could be the reason of different coalescence in the samples of different categories. An oxide/nitride shell around the clusters may be formed in the source chamber due to the presence of oxygen/nitrogen which may also be the reason for the decreased deposition rate. It can be seen in Table 4.2 that at lower average source pressures we had higher deposition rates. The increase of deposition rate with decrease in source chamber pressure is also evident from the increase in number of clusters measured by mass analyzer (see Figure 4.18).

Another possible scenario is that in the case of higher deposition rate the clusters being deposited on substrate will have less time to grow any oxide or nitride shell around them in deposition chamber, which could increase their coalescence

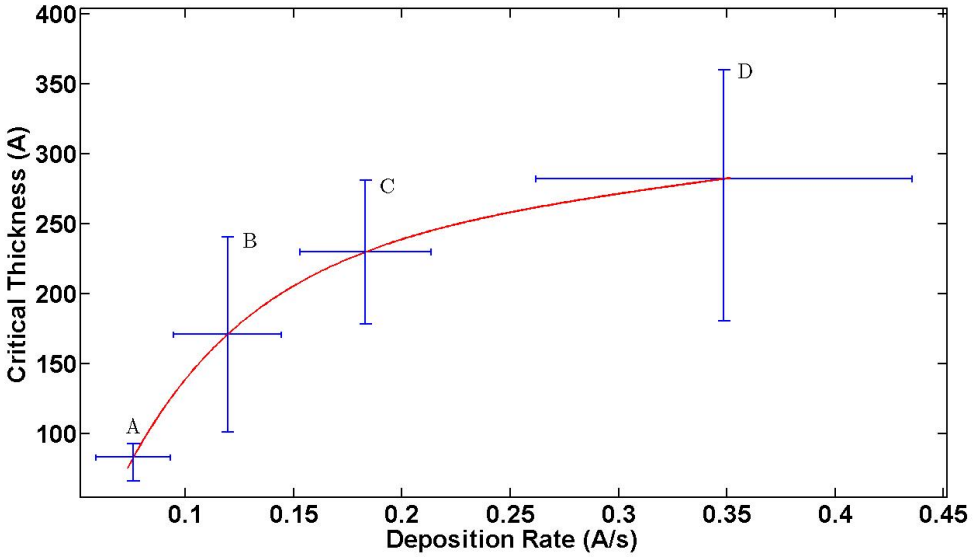

Figure 4.22: Average critical thickness required to achieve percolation threshold versus the average deposition rate for each sample category.

with incoming clusters. Hence, higher coalescence can be expected in the case of higher deposition rates which in turn needs thicker films to achieve percolation threshold as evident from the trend shown in Figure 4.22.

Samples deposited under different source conditions behave differently in terms of onset and can be categorized accordingly. The detailed discussion of all these categories is given in subsequent sections.

4.6.1 Category A

All the samples with less coalesced cluster films showed smooth onsets. The deposition rate for all these samples was ∼0.08 Å/s. The SEM micrograph in Figure 4.23(a) shows clusters coalesced to form bigger interconnected islands with average size[4] ∼ 400 nm^2 after coalescence (average cluster diameter deposited was 7.5 ± 2 nm).

The source pressure for the samples of this category is 650 mTorr which is the highest compared to all other categories showing higher coalescence. The mass spectra for clusters produced in source chambers presented in Section 4.19 clearly shows the effect of source pressure. As discussed in Section 4.6 that lower deposition

[4]The island size was calculated using the watershed algorithm (see detail in Section 2.7).

rate and higher source pressure could be indications of formation of oxide/nitride shell around the clusters in source chamber.

The formation of the oxide/nitride shell around the clusters in source chamber [158] could be the reason for smaller amounts of coalescence compared to the samples from other categories. After the end of deposition conductance decreased as bigger islands were formed with higher thicknesses than the average thickness at the time of the end of deposition. In category 'A' samples conduction does not show significant conductance steps in response to applied voltages.

4.6.2 Category B

Samples in this category showed quantized steps in conduction-onset curves. Figure 4.23(b) shows a staircase of quantized steps of the order of $1G_0$ (see Section 4.6.6 for details). The average cluster island size for category B is 1500 nm^2 (see Table 4.2). The film structure is clearly different from the other type of samples as the cluster coalescence is somewhere between those of category 'A' with very small amount of coalescence and on the other hand category 'C' and 'D' with huge coalescence. SEM and conduction onset curve of a typical sample from category 'B' is shown in Figure 4.23(b).

In most cases, after the end of deposition the conduction of the samples decreased in a step-wise fashion up to a point where the conduction reached a very small value. On the other hand in some samples the conduction was also found to increase in steps as well as decrease, in contrast to the other sample categories where film conduction drops to zero abruptly in one or two steps after the end of deposition. A detail discussion of the conduction behaviour after onset is presented in Section 4.7.

4.6.3 Category C and D

Samples deposited with lower source pressures ($\leq$ 615 mTorr) had higher deposition rates and higher coalescence in the deposited films compared to category 'A' and 'B' samples. The average diameter for the islands is 90 ± 40 nm. Category 'C' and 'D' samples have onset curves with large steps with difference in conduction $\sim 5G_0$ and $>10G_0$ respectively. Because of the high coalescence the percolation is achieved at much higher average thickness compared to the other category sam-

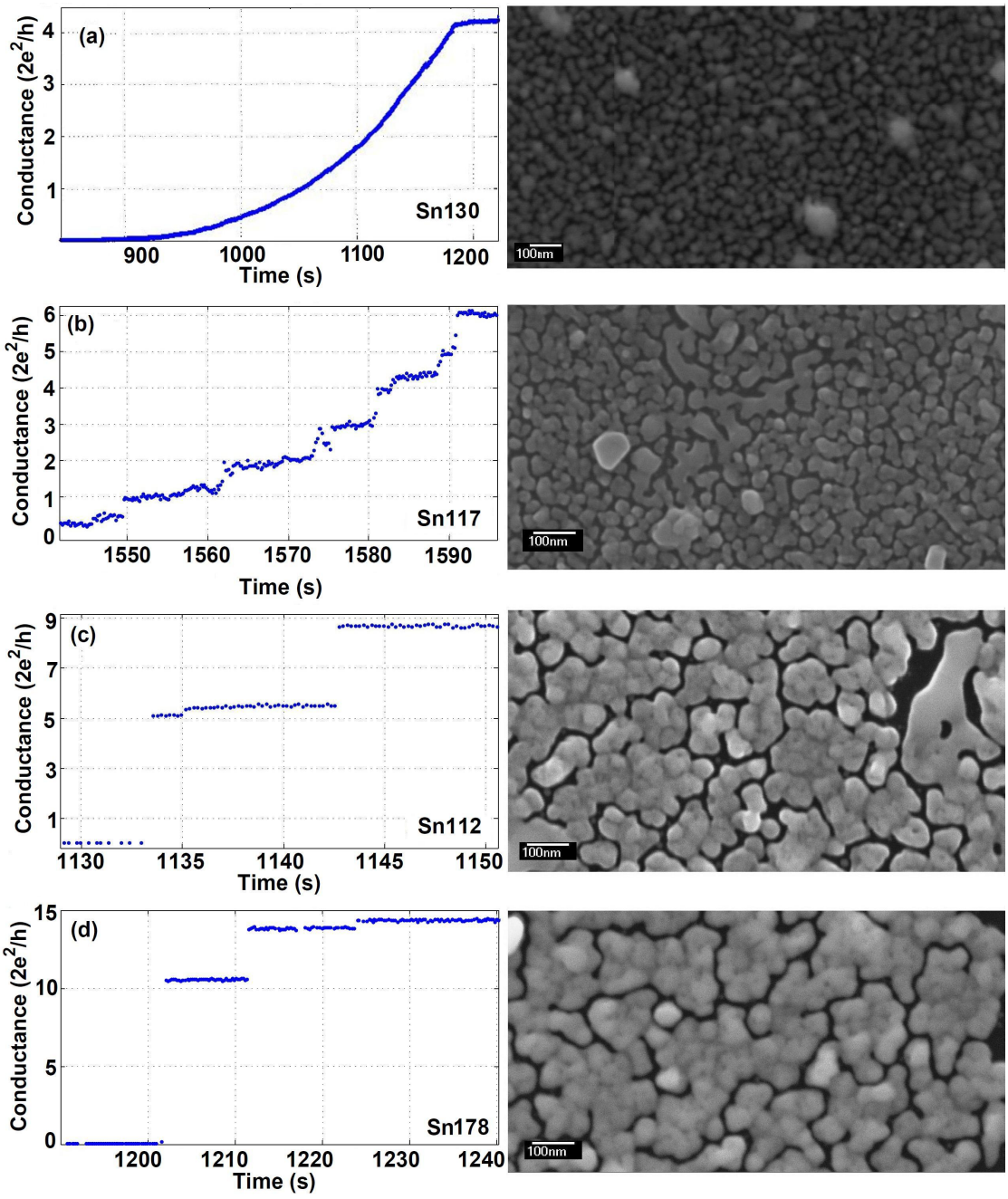

Figure 4.23: (a) Category 'A' sample showing a smooth onset of conduction after the percolations threshold is reached. On the right side, an SEM micrograph showing film morphology of the sample. (b) Category 'B' sample showing stepwise increase in conductance during the onset. On the right side an SEM micrograph showing coalesced nanocluster film structure for this sample. (c) and (d) Conduction onset curve for typical samples of category 'C' and 'D' showing huge jumps in conductance during onset. Respective SEM micrographs on right hand side show highly coalesced cluster islands.

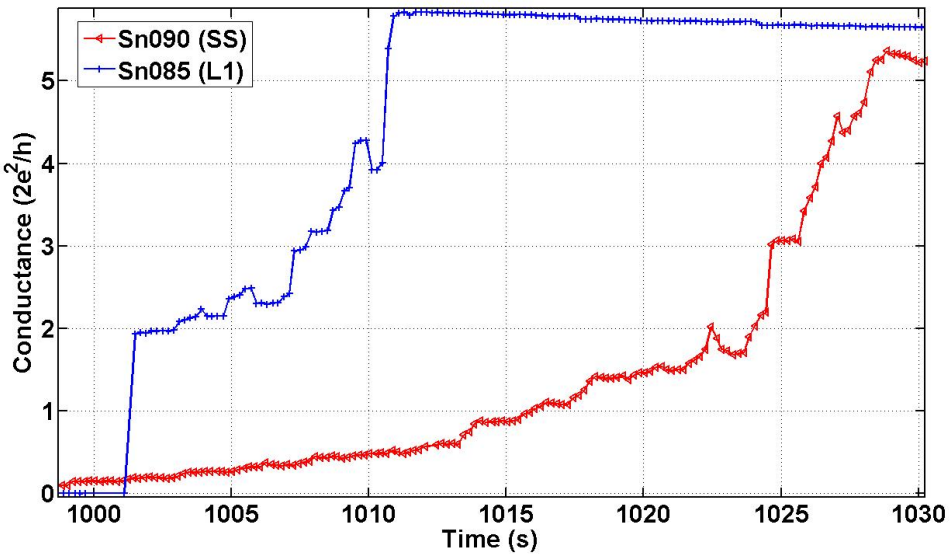

Figure 4.24: Conductance onset curves for SS sample (Sn090) and lithographically prepared L1 type sample (Sn085). SS type sample showed a continuous onset of conduction whereas L1 type sample showed an initial step of the order of $1G_0$.

ples. SEM images along with onset curves for categories 'C' and 'D' are shown in Figure 4.23(c) and (d).

4.6.4 Substrate Surface Effect on the Onset behaviour

It was observed that certain samples behave differently in terms of conductance onset due to differences in the substrate surface even for similar source conditions and deposition rate. Figure 4.24 shows onsets of conduction of samples with SS and L1 type substrates[5] under similar deposition conditions. Both types of samples have electrodes with 200 μm width and 100 μm gap. Many of L1 type substrates fabricated using photolithography showed a jump of the order of $1G_0$ when the sample reached the percolation threshold. On the other hand SS samples fabricated using a shadow mask showed a smooth onset of conductance. However after the initial onset, conductance behaviour was similar as both type of samples show non-smooth increase in conductance.

Two possible reasons could be behind this difference in onset. Firstly, the profile of the electrode is different for the two types of samples. The SS type sample's

[5]See Section 2.3 for details about substrate types.

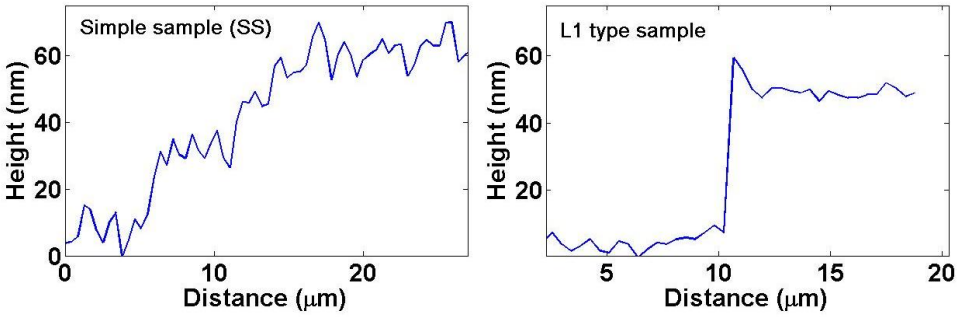

Figure 4.25: Surface profile of: (a) SS type sample fabricated using shadow mask showing a continuous gradient. (b) L1 type Sample prepared using photolithography showing vertically flat edges. Insets show SEM micrographs for each type of sample.

electrodes have a continuous gradient at the edges, inherent in the shadow mask technique as shown in Figure 4.25(a). On the other hand L1 type samples prepared using lithography do not have a continuous gradient, rather these samples have vertically sharp electrode edges (see Figure 4.25(b)).

Secondly, the difference in onset behaviour could be due to the difference in the film morphology of the two types of samples. L1 type samples have been exposed to the photolithography process[6] and its surface could be different compared to the clean Si_3N_4 surface. This difference in surface could lead to different morphology of the cluster film. Due to the difference in conductance behaviour of L1 and SS type samples, it was suspected that a thin film of photoresist residue might be sticking to the substrate surface despite using the standard cleaning process (Section 2.3.4).

To study the effect of photoresist a control experiment was performed with a clean substrate and a substrate with photoresist residue. Figure 4.26(a) and (b) shows SEM images of the sample surfaces with clusters deposited simultaneously under the same conditions. The films consist of random shaped islands separated by cracks of width of a few nanometers.

Figure 4.26(a) shows cluster islands on top of the Si_3N_4 surface and (b) shows cluster islands on top of substrate surface with a photoresist (AZ1518) residue. A small difference in the morphology of the films can be seen in the processed SEM images in Figure 4.26(c) and (d). Smaller islands with narrower inter-island gaps are formed on photolithographically prepared samples in contrast to the slightly

[6]L1 samples were prepared by coating a photoresist mask which was used for lift off process to fabricate Au/NiCr contact pads.

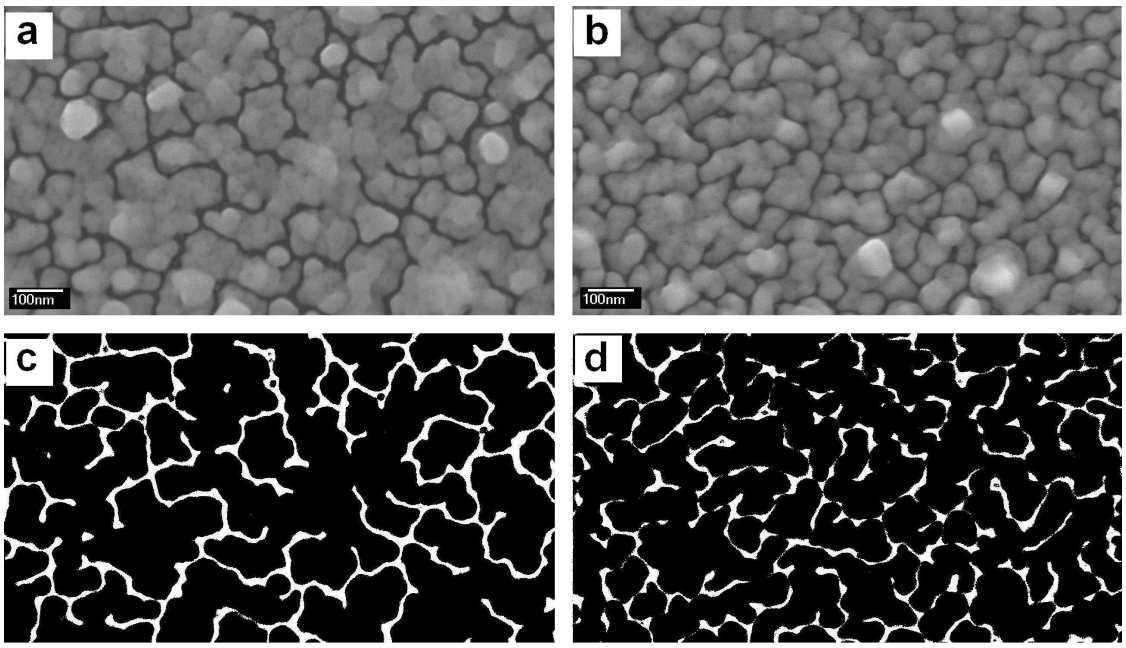

Figure 4.26: (a) Sn cluster islands on top of Si_3N_4 with an average of 10.3 cracks/μm. (b) Sn clusters on photoresist (AZ1518) with average 14.6 cracks/μm. (c) and (d) Processed images of micrographs shown in (a) and (b) respectively showing difference in film morphology.

bigger cluster islands formed with wider inter-island gaps on top of Si_3N_4 surfaces.

The cluster film on the clean Si_3N_4 surface has an average of 10.3 cracks per micron and the crack density for the film on top of lithographically prepared sample is 14.7/μm. The results indicate that any photoresist on the Si_3N_4 substrate changes the surface. The change in substrate surface could lead to a different surface wetting angle for cluster islands and could also change the coalescence, resulting in an increase in crack density.

Further investigation is required to fully understand the effect of photoresist on the film morphology and device conduction behaviour. However, for the sake of consistency in experimental conditions, the standard cleaning method (see Section 2.3.4) was used for all the results (for SS, L1 and L2) presented in this chapter.

4.6.5 Resistance Calculations for Cluster Films

This section provides some estimations of resistance for Sn films for reference which might not necessarily accurate for the cluster films under investigation in this

chapter. To begin with the bulk resistance[7] of a Sn film with 1:2 length to width ratio and a thickness of the order of 17 nm[8] is of the order of 6 Ω. However when the size of the structures becomes comparable to the mean free path of electrons l_0 the resistivity of materials differs from that of the bulk. The overall resistance of the cluster films depends upon factors such as surface scattering and grain boundary scattering. Also constrictions in the conductance pathways, such as necks between two clusters, will lead to extra contact resistances.

As the film thickness t_f decreases, surface scattering becomes more and more prominent factor in resistivity. The resistivity due to surface scattering can be found by the Sondheimer relation [161]:

$$\rho_{surface} = \rho_{bulk} \frac{3(1 - P_s) l_0}{8 t_f} \tag{4.17}$$

here P_s is the probability of electrons scattering elastically from the surface, l_0 and ρ_{bulk} are the mean free path and bulk resistivity respectively.

Figure 4.27(a) shows the ratio of resistivity due to surface scattering to the bulk resistivity as a function of film thickness. The calculations are done for Sn [9]. The average film thicknesses for all categories discussed earlier are between 8 and 28 nm. In this range of thicknesses the surface scattering adds up only few percent to the bulk resistance of the cluster film.

The resistivity due to grain boundary scattering for grain size D_g can be estimated using Mayadas-Shatzkes (M-S) theory [163] and is :

$$\rho_{gs} = \rho_{bulk} \frac{3 l_0 P_g}{2(1 - P_G) D_g} \tag{4.18}$$

here P_g is the probability of electrons scattering from grain boundary. The above equation has been plotted for a range of diameters and is shown in Figure 4.27(b). It is clear from the figure that the resistivity due to grain boundaries is ~ 10 times the bulk resistivity for grain size$\sim$ 1 nm which is still not big enough to explain the kΩ resistance measured for our Sn cluster films.

According to the above discussion the observed resistance of the order of kΩ in Sn cluster films cannot be explained by either of the above phenomena. However, considering the percolating nature of the film structure, probably the main source

[7] using $R_{bulk} = \rho \frac{L}{A}$ where L and A are the length and the cross section area.

[8] Average film thickness of category 'B' samples.

[9] Considering mean free path = 4.1 nm [162]

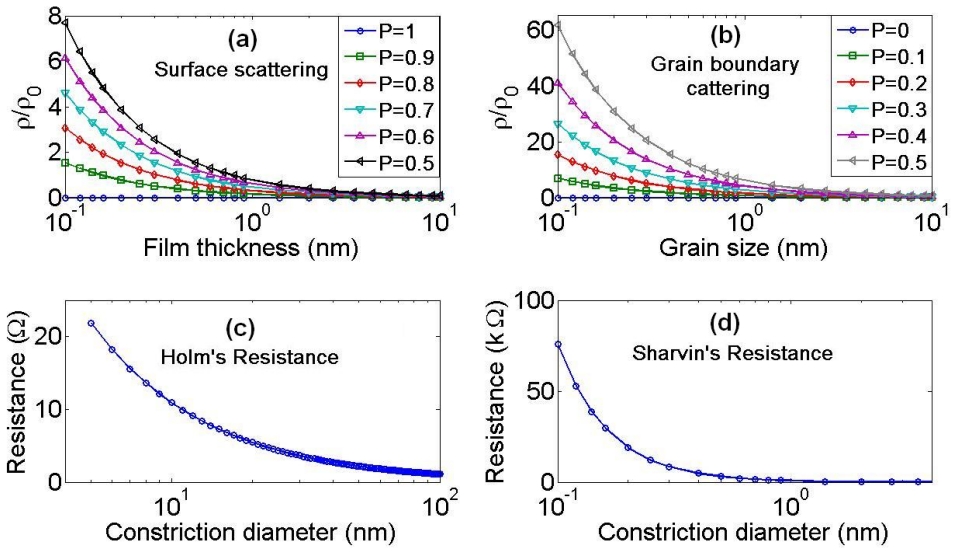

Figure 4.27: Resistivity due to surface scattering in in films of various thicknesses. (b) Effect of grain boundary scattering on thin film resistivity. (c) Holm's resistance due to constrictions bigger then mean free path. (d) Sharvin's resistance due to constrictions less then mean free path.

of resistance are the critical necks. The resistance of the necks between clusters can be estimated using Holm's equation and Sharvin's equation (see Section 3.1.3). The variations in the resistance of necks with diameter D using Holm's and Sharvin's equations are shown in the Figure 4.27(c) and (d). From the figures it can be seen that the necks of few Å would exhibit resistance in the kΩ range according Sharvin's equation.

The observed resistance of the order of kΩ in experiments indicates that the contact diameters in our films are in a regime where $D \ll l_0$ with neck sizes of only few Å which corresponds to a few atom contact.

It has already been discussed Section 4.2.2 that single atom contacts exhibit quantized conductance. Sn cluster films also show conductance quantization and are discussed further in the following section.

4.6.6 Quantized Steps in Conduction Onset

Samples in category 'B' showed a stepwise conduction onset after the film coverage reached the percolation threshold. It has been observed that the conductance

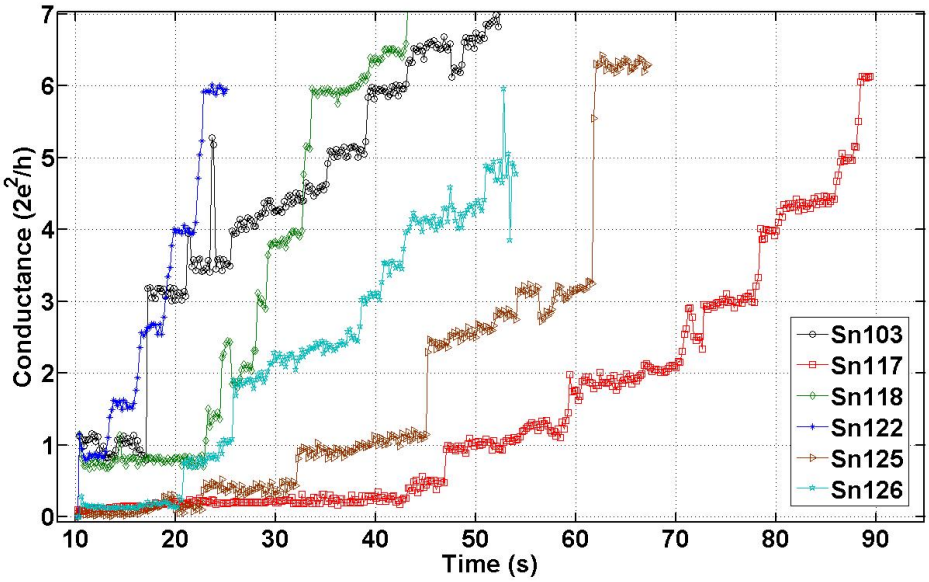

Figure 4.28: Typical onset conductance curves for category 'B'. Although the conductance curves for the samples deposited under similar conditions show slight variations in behaviour, however for all these samples conductance preferentially jumps to values close to integral multiple of the conductance quantum (G_0). Here t=0 represents conductance onset point.

jumps preferentially to conductance levels with values close to integral multiples of the conduction quantum G_0. Figure 4.28 shows few examples of such conduction onset curves which clearly show plateaus near values close to integral multiples of G_0. The deposition conditions for these samples are given in Table 4.3.

The quantized conduction behaviour shown by the Sn cluster films such as shown in Figure 4.29 are very similar to that of the break junctions presented in Section 4.2.3. The 12.9 kΩ resistance corresponding to the step sizes observed in these films is much larger than expected resistance for a thin film of Sn (see Section 4.6.5). Sn percolating films consist of complex networks of cluster islands and there is a possibility of formation of break-junction-like single atom connections. Due to high coalescence in category 'B' samples, incoming clusters form bigger islands with only a few nanometer cracks separating them from each other. Once the film area coverage reaches the percolation threshold a conducting path between the electrodes could be formed even by a single incoming cluster and single atom contacts could be formed as discussed below.

Sample number	Deposition Rate Å/s	Critical Thickness nm	Aggregation Length cm	Source Pressure mTorr
Sn103	0.1	12.6	13	622
Sn117	0.08	12.4	13	646
Sn118	0.12	11.3	13	625
Sn122	0.08	10.4	9	595
Sn125	0.1	9.0	13	581
Sn126	0.1	10.8	13	636

Table 4.3: Source conditions for selected samples from Category B. All the samples were deposited on L2 type substrates using 25 W sputter power.

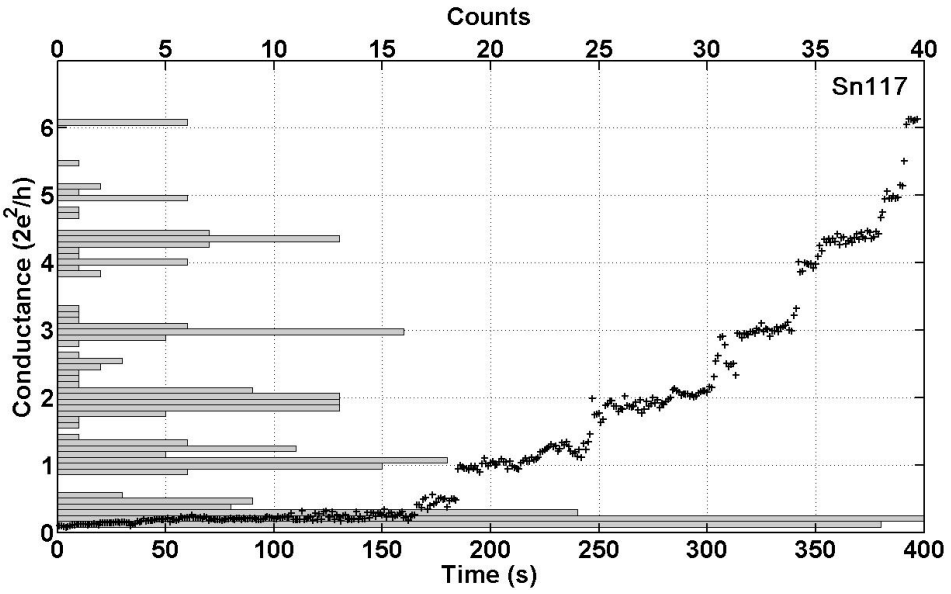

Figure 4.29: The onset conductance curve for L2 type sample along with the histogram showing number of data points recorded for certain conductance value.

Three possible scenarios of single atom contact formation are presented in Figure 4.30. In scenario (a) the final cluster lands close enough to a cluster island to form a single atom connection straightaway. In scenario (b) the final cluster completing the conduction pathway lands directly on one of the islands across the critical gap and then coalesces to form a bigger island. This bigger island could finally make a single atom connection to the island on the other side of the gap. In scenario (c) a single atom contact is formed in three stages. (I) A nanowire-like structure is formed in the cluster films. (II) The structure formed in step (I) becomes thin enough to form a single atom path due to a phenomenon like the Rayleigh instability [43, 164, 165]. (III) The single atom junction formed in (II) is connected to the percolating path by another incoming cluster.

It was observed that conductance of the film increases in steps to 2, 3, $4G_0$ if deposition is continued. This could be due to the formation of more than one parallel single atom contact in the film.

Considering the 0.1 Å/s deposition rate, roughly a million clusters with average size of 7.5 nm land every second on a SS sample during the deposition. These clusters land on random sites forming random shaped island structures. There is a probability of formation of single atom junctions in these randomly shaped islands with a gaps of ≤ 2 nm under circumstances similar to shown in the Figure 4.30.

Single atom junctions could also be formed, between inter-island gaps formed during the deposition, due to a process such as electric field evaporation (Section 4.2.6). However this idea can be discounted due to the fact that the voltage[10] applied during the deposition can only generate electric fields of a few mV/Å. Whereas the typical field intensities required for electric field evaporation is of the order of few V/Å for metals [166].

In case of percolating Sn films, the measured conductance is due to critical necks and the conductance of rest of the film. This could be a reason why some samples in Figure 4.28 show steps smaller than $1G_0$. Although the probability of observing quantized conduction in break-junction-like structures is relatively high compared to other conductance values, still it is difficult to see pure quantized conduction. Therefore, conductance histograms are helpful to analyse the data in such cases. The quantized values were divided into a number of bins. The histograms were then constructed by counting number conductance data points whose values fell

[10]Typically 50 mV in case of SS and 5 mV in case of L2 samples.

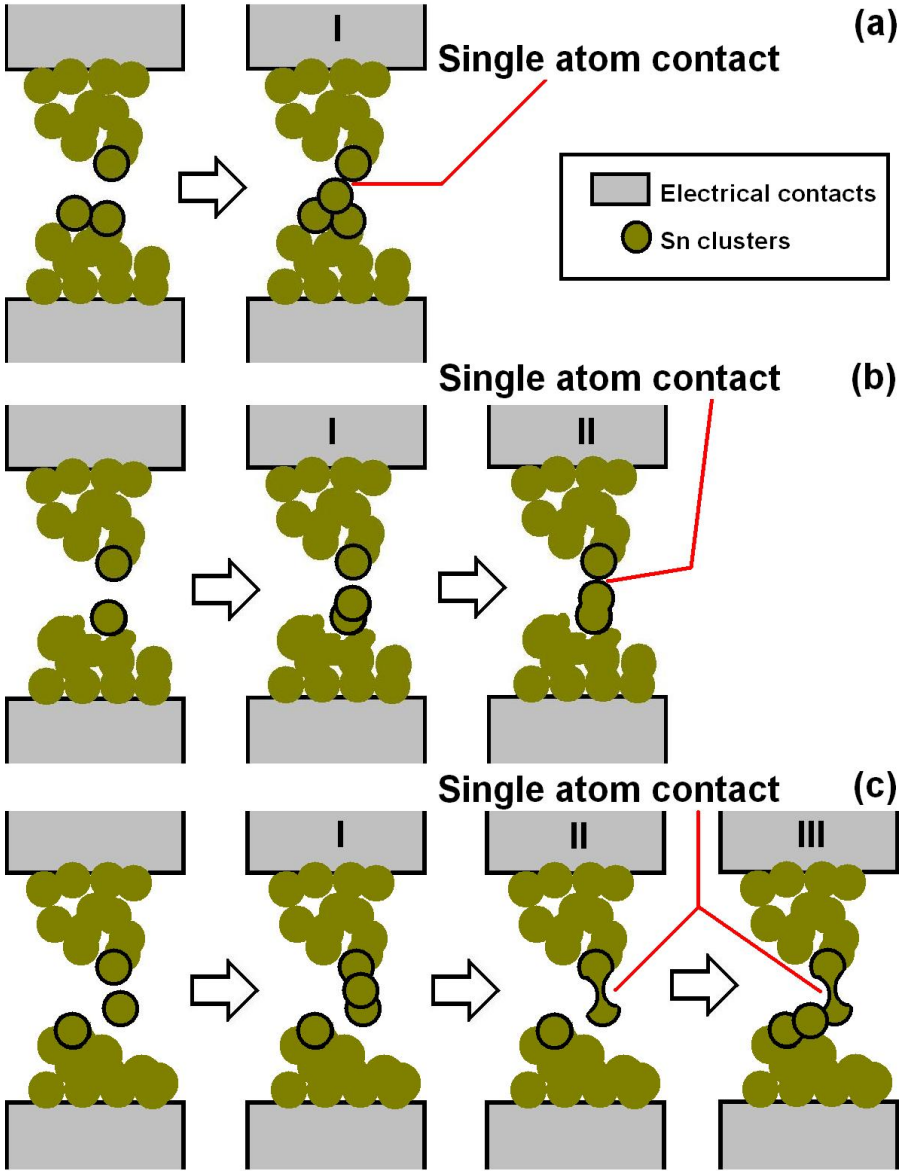

Figure 4.30: Possible scenarios of forming single atom connections in cluster films. (a) The final cluster lands close enough to a cluster island forming a single atom connection. (b) The final cluster completing the conduction pathway lands directly on one of the island across the critical gap and then coalesce and form a bigger island which finally makes a connection to the island on the other side of the gap. (c) Single atom contact is formed in three stages. (I) A nanowire-like structure is formed in the cluster films. (II) The structure formed in step (I) become thin enough to form a single atom path due to phenomenon like Rayleigh instability. (III) The single atom junction formed in (II) is connected to the percolating path by another incoming cluster.

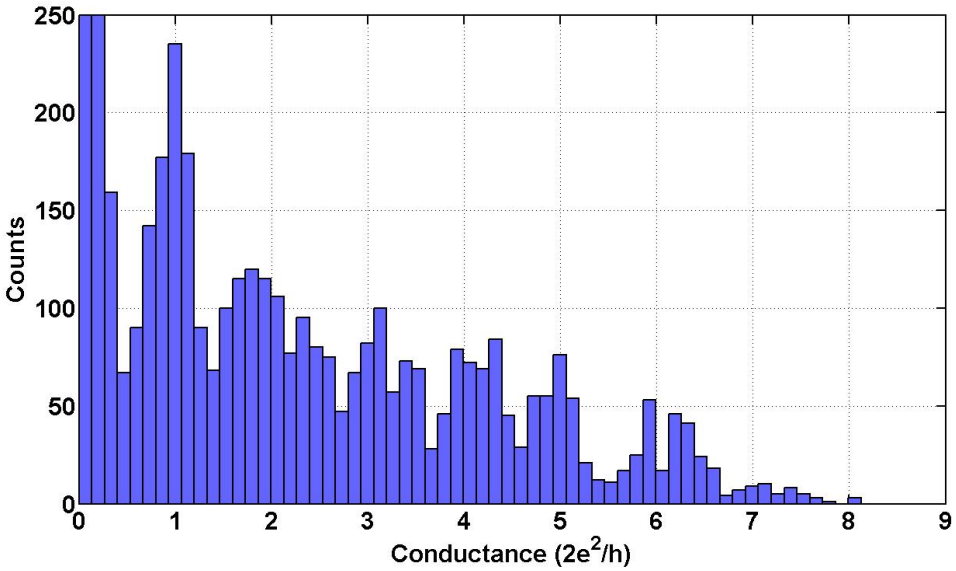

Figure 4.31: Histogram of conduction during the onset for twenty two category 'B' samples showing clean conduction steps. Clear peaks at integral multiple of G_0 are the evidence of conductance quantization during the onsets in these Sn cluster films. The conduction measurements were carried out with sampling rate of 5 Hz and each measurement was considered as a count to form the histogram.

into each bin.

The histogram of the conductance values during onsets showing typical quantized steps of category 'B' samples is shown in Figure 4.31. The peaks in the histogram clearly indicate the higher probability of the conductance taking a value close to an integral multiple of the conductance quantum. Many samples in category 'B' do not show clear steps at quantized conductance however the histogram (of data from multiple samples) reveals peaks near quantized conductance values as shown in Figure 4.31.

The conductance steps observed during onset for category 'B' are interesting as one third of the samples showed at least one distinct step near $1G_0$, which provides a strong indication of the existence of quantized conduction which presumably originates from single atom contacts. The samples from category 'B' also show steps after the end of deposition and are discussed further in subsequent sections.

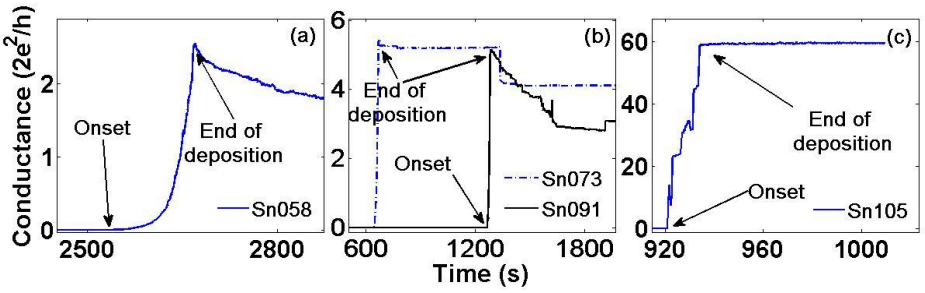

Figure 4.32: Conduction behaviour of samples from (a) category 'A' showing decrease in the conductance over time. (b) 'B' showing conductance decreases in sample Sn091 and the conductance remain stable for sample Sn073. (c) Showing stable conductance for sample Sn105 from category 'C'. Samples from category 'D' behave same as category 'C'.

4.7 Conductance Characteristics after the End of Deposition

The aim of the experiments was to fabricate and study Sn cluster devices which show step behaviour in their conductance after the end of deposition. During the experiments the deposition was stopped after a percolating path was formed and the net resistance of the film was of the order of few kΩ. It was possible to stop the deposition after achieving the desired final resistances due to gradual onsets in the case of category 'A' and 'B' samples. However in case of category 'C' and 'D' the onsets were abrupt and the final resistances were not so controllable. The deposition for category 'D' samples was stopped right after the percolation threshold was achieved.

Figure 4.32 shows typical conduction behaviour of the samples from category 'A', 'B' and 'C'. After the end of deposition the samples from category 'A' show a decrease in the conductance over time. On the other hand, in the case of category 'C' and 'D' the conductance remains stable after the end of deposition. Some samples in category 'B' show a decrease in conductance similar to category 'A' while the other samples show stable conductance behaviour.

Beside the time-dependent changes in conduction indicated above, cluster films show steps in conduction due to an applied voltage. An initial constant voltage of 5 mV and 50 mV was applied for L2 and SS samples respectively, to monitor the conduction during the deposition. Typically the steps were observed when the

voltage was increased from its initial value after the end of deposition. (see Section 4.7.8).

4.7.1 Conductance Steps after the End of Deposition

Sn cluster films consist of complex network of interconnected cluster islands. These cluster islands form conducting paths which span from one end to the other end of the percolating films. After the end of deposition the conductance of these films varies gradually over time under a voltage (5-50 mV) applied to record the conductance. These variations in conductance can be attributed to coalescence between the clusters forming the film. Moreover applying the higher voltages can modify the film conductance behaviour. The applied voltages were gradually ramped to higher values to see its effect on film conduction. In some cases sample become open circuit while in other cases samples started showing interesting conductance variation between discrete conductance levels.

Figure 4.33 shows an example of the electrical conduction of an SS type sample after the end of deposition. Only minute variations were observed in the film conduction until a ramping voltage was applied across the film. After the application of the ramping voltage, the conductance of the film started jumping between different levels. In Figure 4.33 it can be seen that (at t=4500 s) a ramping voltage cycle[11] between 3 V and -3 V was applied. The conductance dropped from $6.9G_0$ to $0.9G_0$ during this voltage ramping cycle. The overall conductance of the sample (whose data is shown in Figure 4.33) could be due to multiple parallel paths formed during the deposition. The $6G_0$ step in conduction at 4500 s seems to be due to the breakage of some of the parallel paths.

The initial breaking of paths could lead to a situation where fewer critical necks are responsible for the overall conductance of the film. These few paths could be altered by ramping an applied voltage. As the applied voltage was increased the conductance of the sample shown in Figure 4.33 increased in big steps. On the other hand when the applied voltage was decreased the conductance decreased in multiple smaller steps. This behaviour was observed over the next six cycles as shown in Figure 4.33.

Sn cluster films showed a variety of conduction behaviour varying from sam-

[11]Here cycle means change of voltage from zero to maximum voltage value in either polarity and back to zero.

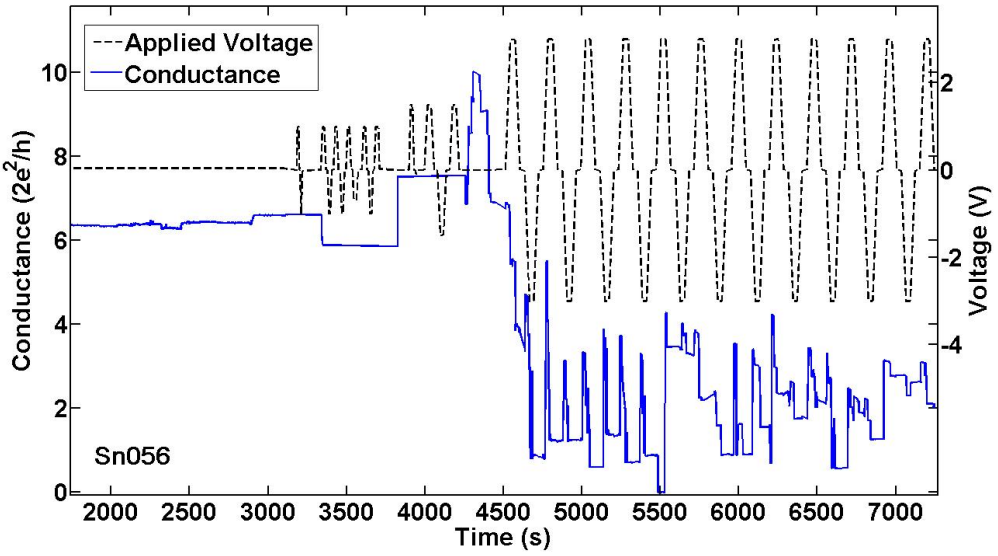

Figure 4.33: Sn cluster film showing stepping behaviour after the end of deposition due to an applied voltage.

ple to sample even deposited under similar conditions. However there are a few characteristic conduction behaviours which can be associated with certain types of films which were deposited under similar conditions. During the course of experiments the samples were prepared under different conditions. All these samples have already been categorised in Section 4.6 with respect to their onset conductance behaviours and film morphologies. Table 4.4 shows a summary of the number of samples showing step behaviour in each category along with the range of step sizes observed.

Category number	Step size in onset	Total Number of Samples	Samples Showed Steps(%)	Step Size after deposition
A No steps	61	5%	$\leq$0.5 G_0	
B	$\sim$ 1 G_0	67	67%	$\leq$5 G_0
C	$\sim$ 5 G_0	28	18%	1-30 G_0
D	$>$ 10 G_0	40	10%	4-50 G_0

Table 4.4: Summary of steps shown in various categories. The steps size column shows the range of step sizes observed in each category. Note: 61 samples of category 'A' contains 50 samples from Batch 1 and 11 from Batch 2.

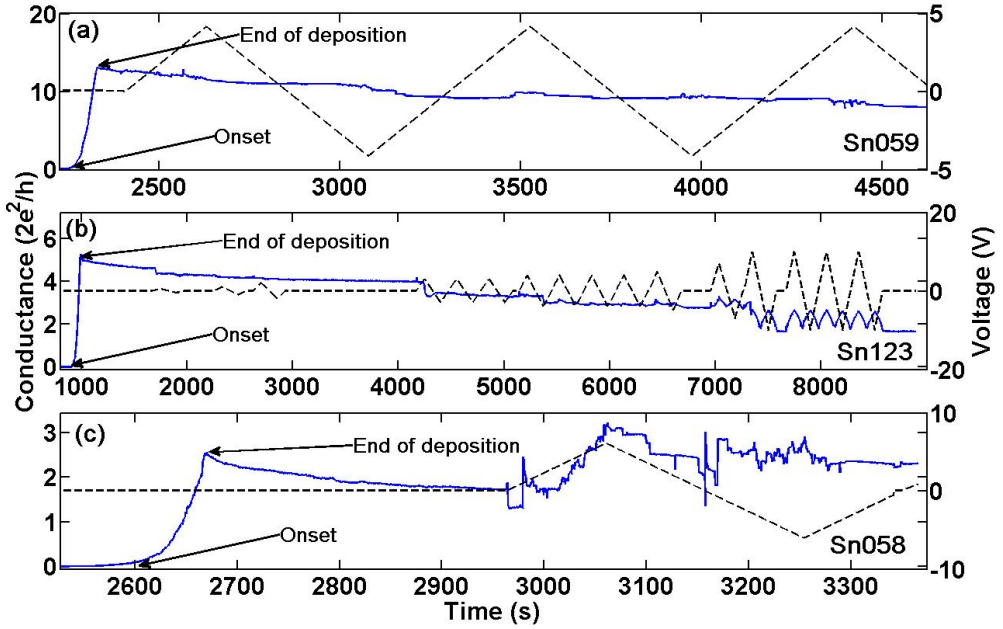

Figure 4.34: Category 'A' samples showing very few steps in conductance (solid line) after the end of deposition. The dashed line represents applied voltage.

4.7.2 Conductance Steps in Category A

Most of the samples from category 'A' do not show step behaviour after the end of deposition (see Figure 4.34(a) and (b)). However, some samples showed small steps with sizes $\leq 0.5G_0$. The conductance levels of the steps shown by category 'A' samples were not very well defined as shown in Figure 4.34(c). The source conditions and the film morphologies play an important role in defining the stepping behaviour of the cluster films. The samples in category 'A' have typical island sizes of ~ 400 nm^2 which is much smaller than category 'B'. Many samples in category 'A' are from the Batch 1 (see Section 4.4.1) samples which were deposited when there was a leak in the system.

4.7.3 Conductance Steps in Category B

The steps were especially observed in category 'B' samples. Sixty seven percent of category 'B' samples showed discrete steps with a sizes of a few kΩ due to the applied voltage ramp after the end of deposition. Figure 4.35 shows the range of conduction behaviours exhibited by the samples included in category 'B'. Commonly the SS and L1 type samples show multiple steps with both increase and

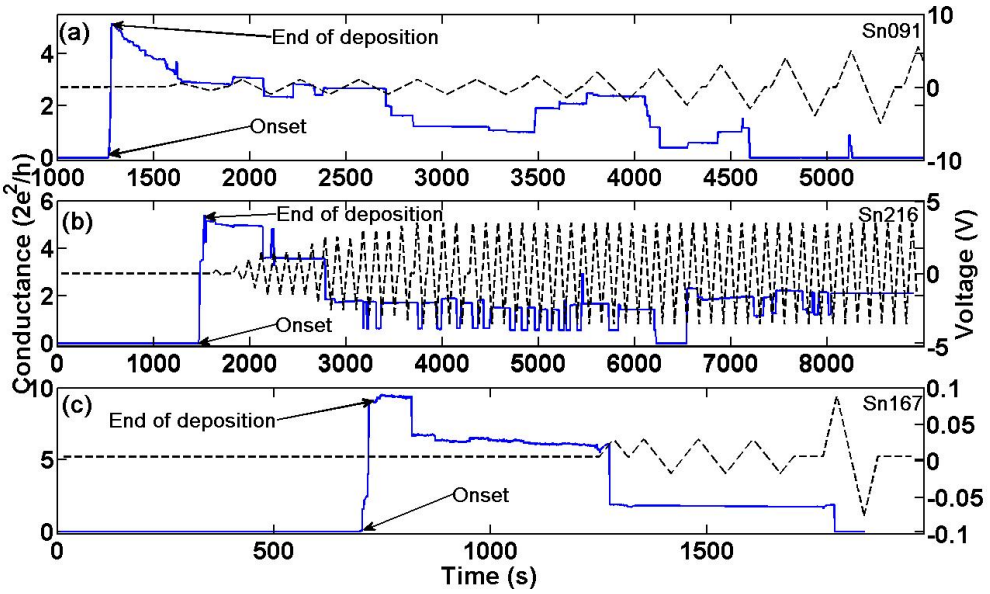

Figure 4.35: Range of conductance behaviours shown by category 'B' samples after the end of deposition under and applied voltage (dashed line). Conductance is represented by solid line. Samples show both reversible and irreversible steps.

decrease in conductance in a stepwise fashion. On the other hand L2 type samples show only a few downward steps leading samples to a very low conductance state of the order of few μS. Figure 4.35(a) and (b) show reversible stepping behaviour where the conductance jumps both to higher and lower conduction levels under an applied voltage ramp. Figure 4.35 (c) shows a typical conductance response of an L2 type sample where the conductance decreased in only a few steps. The details of the voltage dependence of this stepping behaviour are discussed in Section 4.7.8.

4.7.4 Conductance Steps in Category C and D

In contrast to category 'A' and 'B' the samples from category 'C' and 'D' show either no steps or a few very large well defined steps. The average step size for categories 'C' and 'D' is 10 and 16G_0 respectively. The samples from these two categories are very volatile in nature and even a small increase in voltage can kill the sample. Figure 4.36(a) shows typical conduction behaviour after the end of deposition displaying no steps. However there are some exceptions where we can see a few steps, such as Figure 4.36(b). The steps shown by category 'C' and 'D' samples are much bigger compare to the steps shown by category 'B'.

The step behaviour displayed by these Sn cluster films, especially by the cat-

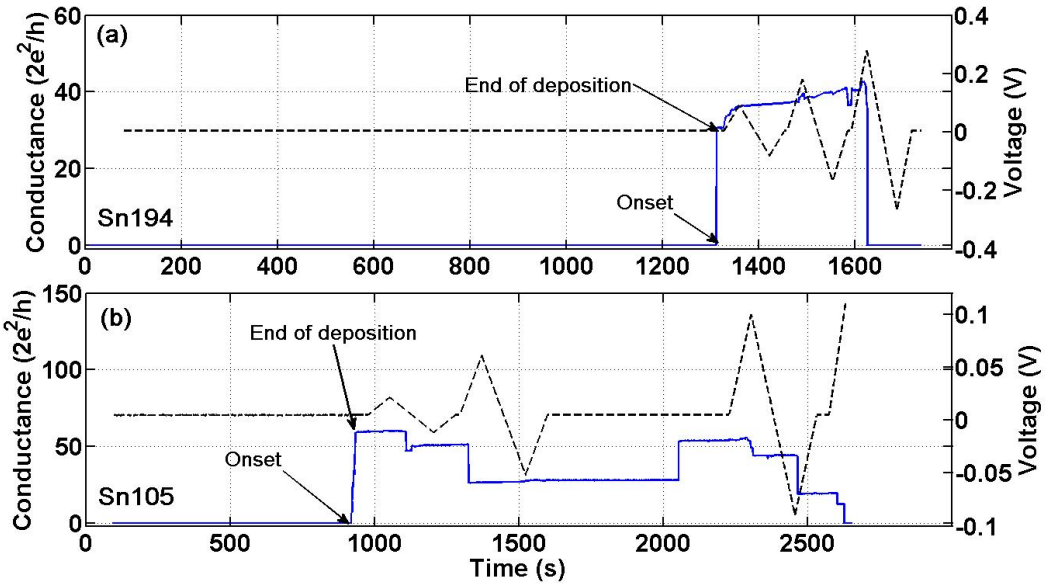

Figure 4.36: (a) Category 'C' and 'D' samples show very few steps in conductance (solid line). The samples jump to highly resistive levels due to an applied ramping voltage (dashed line). (b) Some samples show few steps. The step sizes shown by category 'C' and 'D' are much larger and less frequent compare to category 'B'.

egory 'B' samples can be classified into two groups i.e. monotonic (irreversible) steps and bi-stable (reversible) steps and are discussed in following section.

4.7.5 Monotonic Steps

Steps in which the conductance of the samples decreases monotonically in a stepwise fashion are defined as monotonic or irreversible steps. Figure 4.37 shows three different examples of monotonic steps exhibited by Sn cluster films. All three samples presented here show similar steps but there are differences in the behaviour of the samples in their response to the applied voltage.

Figure 4.37(a) shows an L2 type sample. After the end of deposition at 1800 s the conductance decreases even under an applied voltage of just 5 mV. However in the case of the sample shown in Figure 4.37(b) the steps begin after the applied voltage was increased from 50 mV to 0.25 V. Another step was observed once the voltage reached 1 V after which the sample became highly resistive. Another interesting example of the monotonic steps is shown in Figure 4.37(c). A stepwise decrease in conductance was observed at 0.5, 1 and -1 V after which the sample became highly resistive (>300 MΩ). The sample jumped back to a less resistive

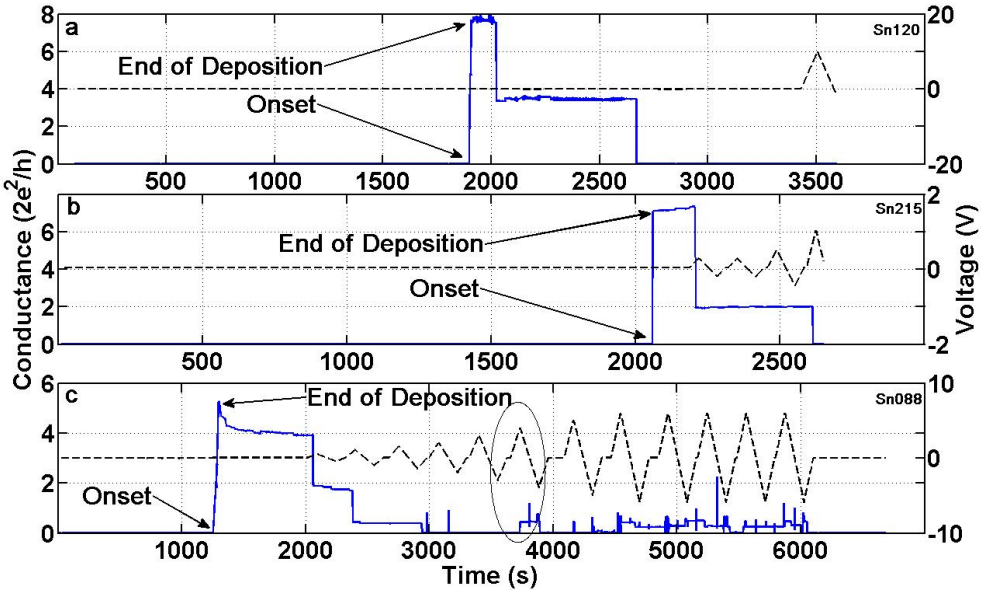

Figure 4.37: Samples showing monotonically decreasing conductance steps. (a) An L2 type sample showing steps in conductance (solid line) at very low constant applied voltages of 5 mV (dashed line). (b) An example of SS type sample showing monotonic stepping behaviour exhibited due to increase in applied voltage. (c) An L1 type sample showing stepping behaviour due to increase in applied voltage, the samples resistance became very high after three initial steps but it revived its low resistance state once the voltage was further increased as indicated.

state (28 kΩ) as the applied voltage was increased to 3 V.

It has been observed that monotonic steps are more common in L2 type samples whereas SS type samples show both monotonic and bi-stable steps (Section 4.7.6). The film area of L2 samples is hundred times smaller than the SS samples and hence have a comparably smaller cluster networks[12]. Therefore in L2 samples there is less possibility of formation of complex structures[13] required for bi-stables steps.

L2 sample may have multiple parallel paths and due to the applied ramping voltage these path may break one by one showing monotonic steps. The current produced by the applied voltage is big enough to cause electromigration and hence break conducting paths. The L2 type samples have cluster films with an average cross-section area of the order of 10^{-13} m^2 (considering a continuous film) and a

[12]Considering ∼10 nm cluster as building blocks the SS type samples consist of a network 10000×20000 cluster compared to 1000×2000 for L2 type samples.

[13]Structures which might show phenomenon such as Coulomb blockade, electric field induced evaporation and solid state electrochemical reaction discussed in detail in Section 4.7.8.

resistance of the order of few kΩ. Therefore a voltage of the order of 0.1 V can produce a current density of $\sim 1 \times 10^5$ A/cm^2 which is high enough to produce electromigration in tin [135]. Another reason for monotonic steps could be Joule heating due to the current passing through such sample, which could rupture the percolating pathways due to melting. It is important to note here that in percolating films the conductance path is much narrower and the current densities could be much higher compared to the values given above for thin films.

4.7.6 Bi-stable Steps

As well as the monotonically decreasing conduction steps discussed in previous section, some samples from category 'B' show reversible or bi-stable steps. In this type of stepping behaviour the conduction jumps back and forth between two or more well defined levels under an applied voltage. Figure 4.38 shows a range of bi-stable steps observed in different samples. Reversible steps are only observed in SS and L1 type samples which have an active cluster film area of 100×200 μm between the contacts. Figures 4.38(a) and (b) show samples exhibiting reversible steps between three or more levels. Figure 4.38(c) shows a sample whose conductance jumped, most of the time, between two well-defined levels like a switch.

Some bi-stable steps show characteristics similar to non-volatile memory devices. Figure 4.39 shows the conduction variations of an SS type sample due to applied voltage. The conductance of the sample jumped between $0.5G_0$ and $1.5G_0$. These conductance levels may be assigned logical values of '0' and '1'. The sample jumped to the ON state ('0' to '1' transition) when the applied voltage reached ∼-3.5 V during the voltage ramp. The sample then retained the ON state until the voltage was increased to a 3.5 V where the conductance jumped to the lower level (OFF state). This device remembered its logical state even when the applied voltage is zero. Similar bi-stable (reversible) conduction steps can also be seen in other samples from category 'B' (Figure 4.38(c)). In these devices the cluster film morphology is a complex percolating structure which evolves over time due to phenomena like coalescence, melting due to Joule heating and electromigration. Hence the steps also vary over time. It can be seen in Figure 4.38(c) that the conductance jumped between roughly three different levels. After ∼800 s the conductance started to jump between two levels just like a square wave similar to the one shown in Figure 4.39. However this is not a permanent behaviour of such films

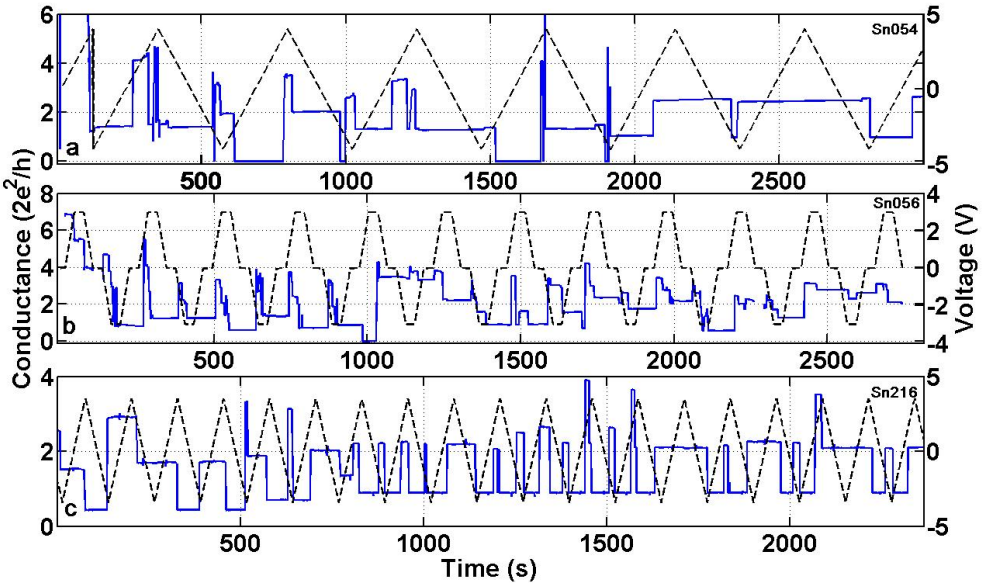

Figure 4.38: Examples of bi-stable steps exhibited by Category 'B' samples. Conduction data shown for three SS type samples (solid line) and the applied voltage is represented by dashed line. (a) and (b) showing samples jumping between multiple levels in a single voltage cycle. (c) Shows sample showing bi-stable steps especially between 800 to 2000 s.

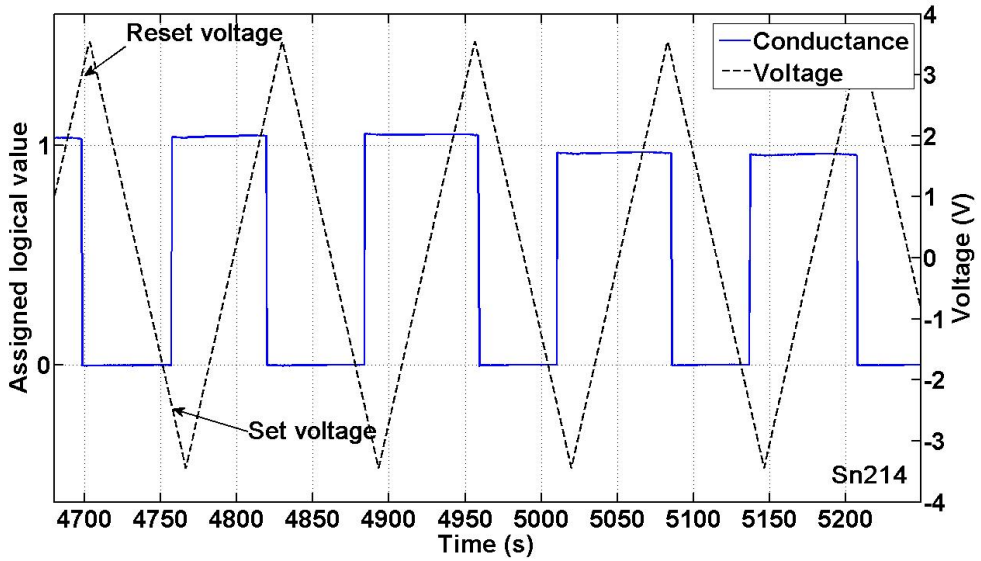

Figure 4.39: An example of non-volatile memory like steps jumping between two well defined levels. Conductance values of 0.5 and 1.5G_0 are assigned logical values of '0' and '1' respectively.

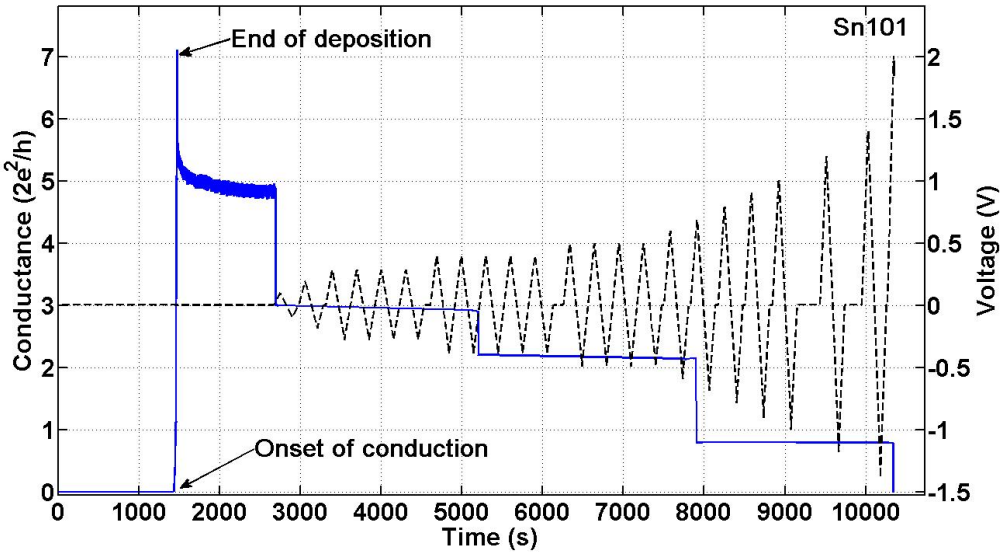

Figure 4.40: An example of quantized conductance observed in Sn cluster films. The plot shows conductance (solid line) along with the applied voltage (dashed line) for an L2 type sample. The conductance preferentially stays at the conductance levels near 3, 2 and $1G_0$.

and with the passage of time either the values of conductance levels change, or new conductance levels emerge. The possible mechanisms behind these reversible switching events are discussed in detail in Section 4.7.8.

4.7.7 Conduction Quantization in Sn Cluster Films

Sn cluster films showed steps both during and after the end of deposition. The quantization of conductance during the onsets has already been discussed in Section 4.6.6. The conduction after the end of deposition also shows conduction quantization. It has been observed that the values between which the conductance jumps are close to the integral multiples of the quantum of conduction (see Figure 4.40).

The conductance values between which Sn cluster films jump are found to be independent of the film area, aspect ratio, film thickness or applied voltage. Figure 4.40 shows an example of an L2 type sample showing quantized conductance. After the end of deposition, this particular sample initially showed a smooth decrease in conductance. However, when a voltage ramp was applied the conductance jumped to lower conductance levels in three consecutive downward steps each with value

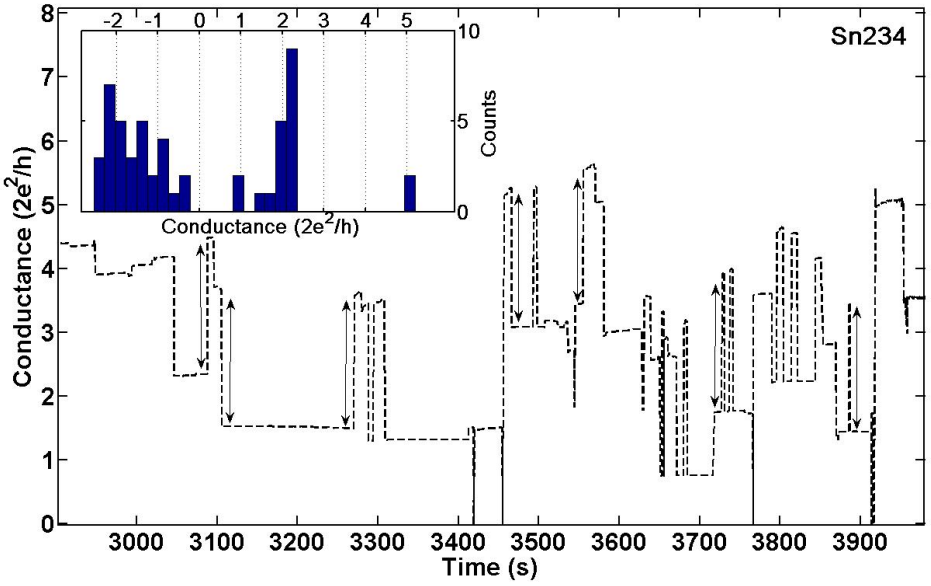

Figure 4.41: Conductance data for L1 type sample showing conductance transition with a step size very close to $2G_0$ as indicated by vertical arrows in the figure each with length corresponding to $2G_0$. Inset shows histogram for all the step sizes showing peaks near $-2G_0$ and $2G_0$ representing downward and upward transition of magnitude $2G_0$ respectively.

close to 3, 2 and $1G_0$. The behaviour shown in Figure 4.40 is strikingly similar to that of break junctions.

In some samples, it seems that the sizes of the steps are quantized instead of the conductance levels. Figure 4.41 shows conductance data for an L1 type sample. In this sample the conductance jumped between various conductance levels not corresponding directly to integral multiples of G_0. However, many conductance transitions had step sizes very close to $2G_0$, as indicated in the figure by the vertical arrows, each with length corresponding to $2G_0$.

Figure 4.42(a) and (b) shows the detailed analysis of the steps for two selected SS type samples. The histogram 'I' in each figure shows the distribution of step sizes. Clear peaks near $1G_0$ for both samples provide evidence of quantized conduction. The probability of step occurrence was found to be higher at higher voltages. This is evident from the peak visible at higher voltages in histograms labelled 'II'. The histogram 'III' in each figure shows the number of steps, which occurred at a certain time after the end of deposition, while the applied voltage was continuously ramped. The decrease in the number of steps for sample Sn054 indicates that the

sample evolved towards an equilibrium state over time. The histograms labelled 'IV' show the values of the conductance when the steps occurred. Peaks near $1G_0$, $2G_0$ and $3G_0$ can be seen for both samples.

During these experiments, many samples showed conductance jumps between well defined levels but quantized conduction levels are not exhibited clearly by all the cluster films. However, a histogram of the combined data of many samples shows peaks at preferred levels of conduction. Figure 4.43 shows a histogram for more than fifty category 'B' samples. A clear peak is visible at $1G_0$ for the conductance data after the end of deposition. Moreover, the data was fitted using Gaussian curves and perhaps two smaller peaks at $2G_0$ and $3G_0$ are also present.

So far, the discussion in this section provides strong indication of Sn cluster films exhibiting quantized conductance in their conductance behaviour. Overall conduction of the percolating networks depends upon only a few critical necks. These critical necks could have diameters of a few angstroms to a few tens of nanometers. However, the width of the necks can shrink to single atom contacts due to a phenomenon such as electromigration. In case of a gradual electromigration process the critical contact width decreases gradually. The electromigration in these single atom necks would stop after forming single atom contacts when the conduction of electrons enters in the ballistic regime (from the diffusive regime) [135]. There is also a possibility of an increase in the contact conductance as neighbouring atoms can join the existing single atom contact due to structural rearrangements. These structural changes can exhibit an increase in conductance in quantum steps [135].

There is also a possibility of formation of nanowire like structures in percolation films. These structures can self-destruct due to the Rayleigh instability [43, 164, 165]. Before the complete breakage due to Rayleigh instability these nanowire-like structures can further shrink and form single atom contacts showing quantized conduction. Electric field induced evaporation (Section 4.2.6) and ion migration due to electrochemical reaction (Section 4.2.7) could also be behind forming single atom contacts.

4.7.8 Voltage and Time Dependence of the Step Behaviour

As shown in the previous section the conductance of Sn cluster films can be modified by varying the applied voltage. The applied voltages can not only modify the

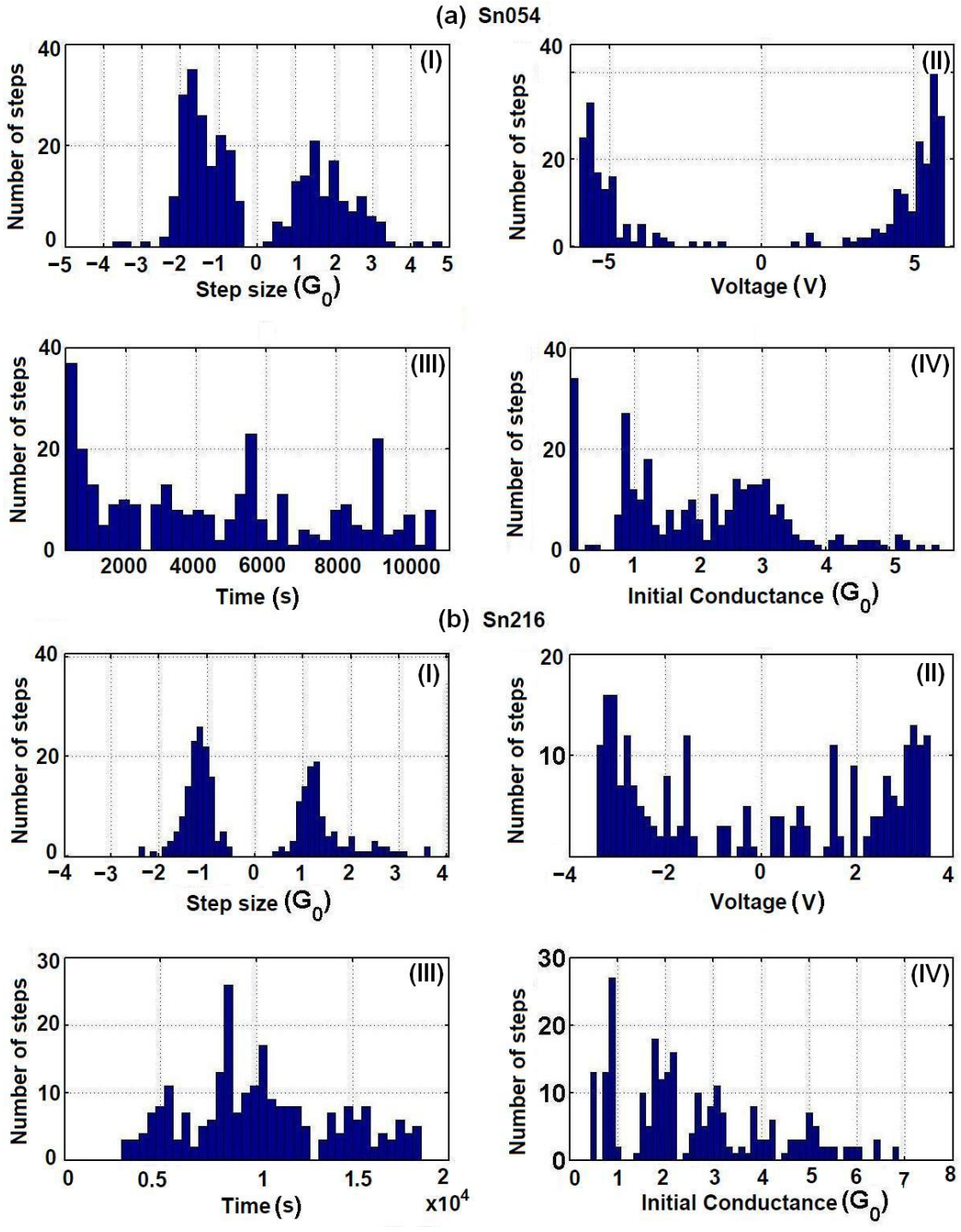

Figure 4.42: Histograms for two simple samples showing (I) step size distribution, (II) number of steps as a function of applied voltage, (III) number of steps as a function of time, (IV) initial conductance where steps occur.

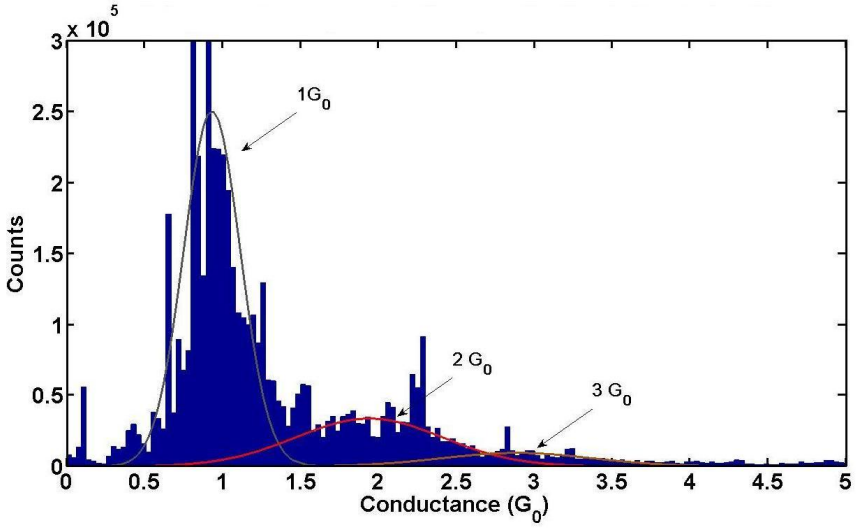

Figure 4.43: The conduction histogram of over fifty samples from category 'B' showing a clear peak at $1G_0$. Gaussian curves were fitted on the rest of data showing peaks at $2G_0$ and $3G_0$.

stepwise conduction behaviour, but can also cause an electrical breakdown in the cluster films. It has been observed that the applied voltage has to be kept below certain limits for samples with different geometries to avoid sudden electric breakdowns. Figure 4.44 is an SEM micrograph of a sample with electrode separation of 20 μm, and shows clear evidence of breakdown. Melting due to passing excessive current through the connected clusters, and subsequent coalescence, resulted in forming larger agglomerates. In such a sample, the conductance drops in only big steps ($>10G_0$) because of the rupture of the conduction path due to melting.

In most deposition experiments 50 mV was applied across the SS type samples to measure the film conductance. However, this voltage is high enough to induce an electric breakdown in L2 type samples. Hence a smaller voltage of 5mV was used for these samples. Figure 4.45 shows a comparison of the voltages under which two typical samples (Sn183 and Sn226) underwent an irreversible resistance jump rendering samples in a very highly resistive state (0.55 GΩ and 1 GΩ). Sample Sn183 (an L2 type sample) has a 10 μm electrode separation compared to a 100 μm separation in case of Sn226. It can be clearly seen in Figure 4.45 that the samples with larger electrode separation can survive higher voltages compared to samples with smaller electrode separation.

It has been observed that the film conductance settles down to a certain value

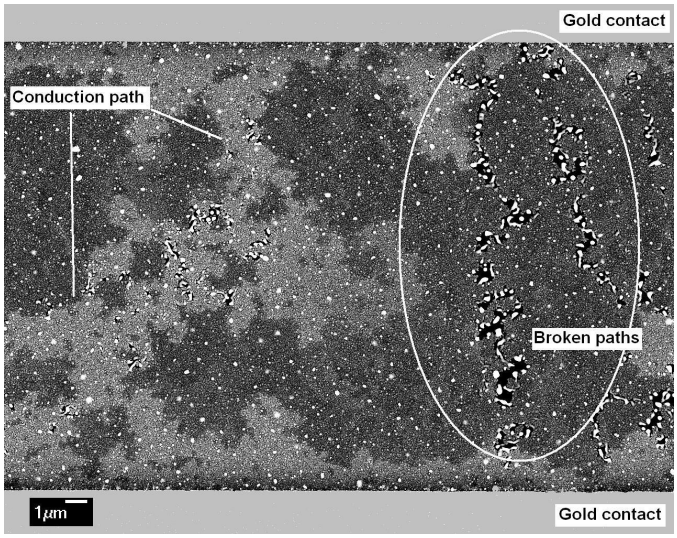

Figure 4.44: A sample showing electrical melting and subsequent coalescence. A trails of Sn agglomerates formed due to an electric breakdown is visible, spaning between the electrodes. The indicated brighter region shows a percolating path still intact.

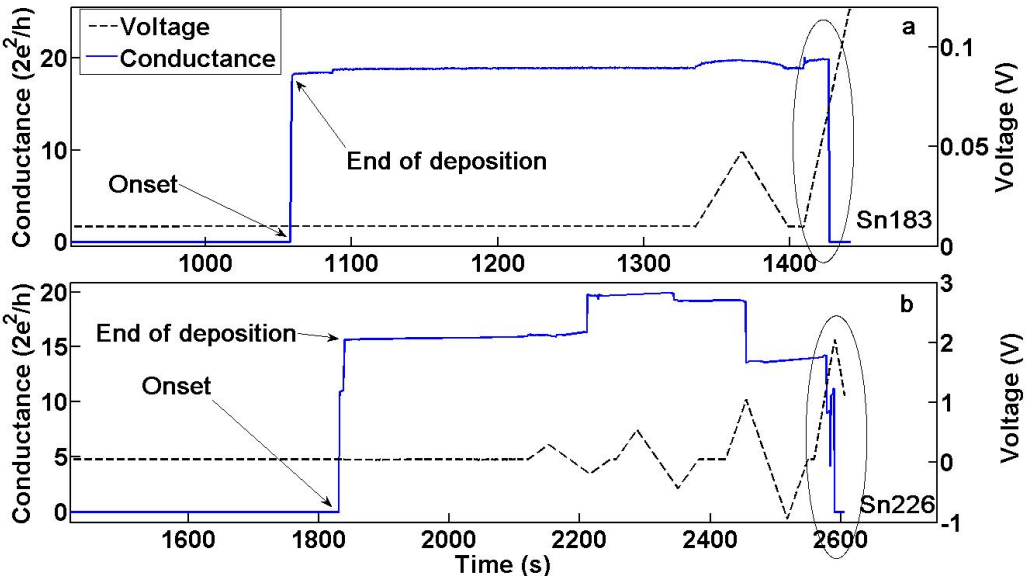

Figure 4.45: The effect of applied voltage on cluster film conductance. (a) Conductance path breaks down at a much smaller voltage (70 mV) for L2 type sample with electrode separation of 10 μm compared to (b) SS type sample with electrode separation of 100 μm which breaks down at 2V.

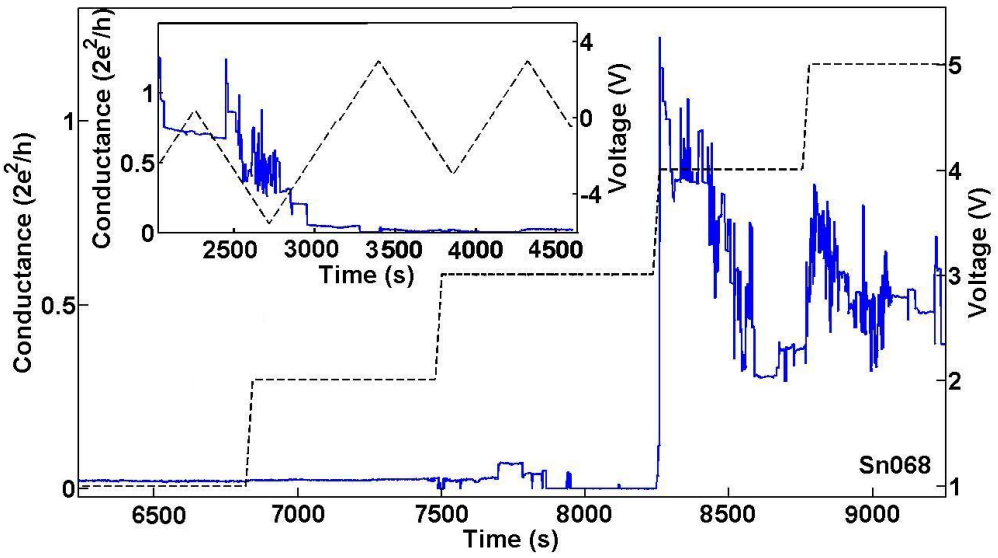

Figure 4.46: Conduction behaviour of Sn cluster films under a voltage changing in a staircase fashion. The sample jumped to very highly resistive state due to the applied voltage as shown (inset). The sample was brought back to stepping mode by increasing the applied voltage in stepwise fashion. The sample jumps to $\sim 1G_0$ after a certain critical voltage is reached.

after some time if the applied voltage is not varied. Figure 4.46 shows conduction data for an SS type sample in a dormant state and shows minor changes in conductance over time. The deposition was stopped for this sample at $\sim 3G_0$ conductance. Later, due to an applied voltage ramp, the conductance dropped to lower values ($1 \times 10^{-3}G_0$) as shown in the inset of Figure 4.46. The decrease in conductance could have happened as a result of breakage of a critical neck in the percolating path. Here the tunnelling resistance of the order of MΩ indicates the formation of a nanogap, probably due to electromigration.

After the breakage, the applied voltage was increased in 1 V steps from zero to 5 V. The sample became active and started showing steps above a critical voltage i.e. 4 V in this case. The step shown at 8300 s is clearly a result of the applied voltage and could be explained by electric field induced evaporation[14] of atoms across the nanogap formed by the initial breakage of the percolating conduction path.

It has also been observed that an aging effect causes the steps to diminish

[14]See introduction in Section 4.2.6.

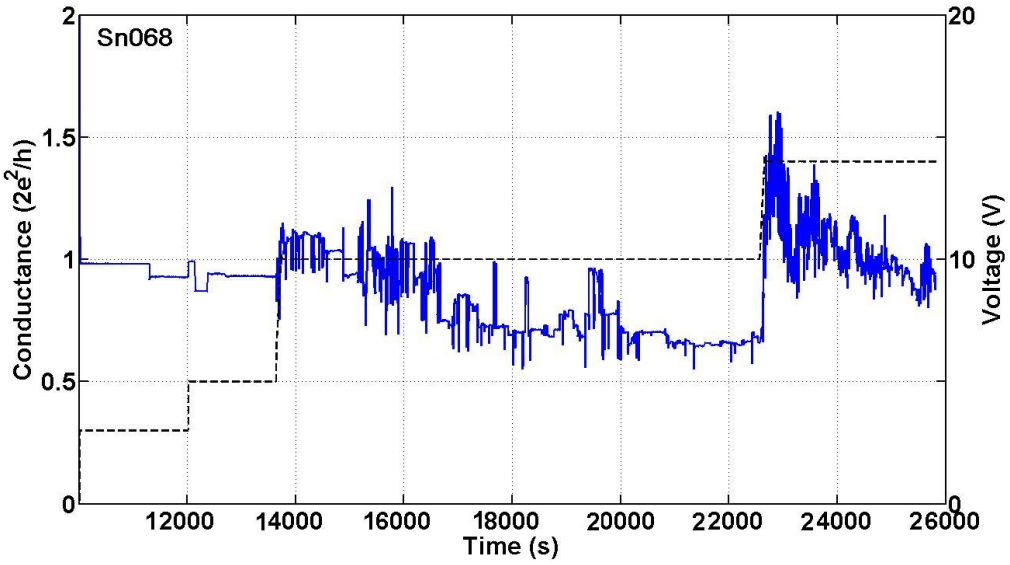

Figure 4.47: The conduction steps diminish with the passage of time when the sample is kept at a constant applied voltage. The step behaviour is revived as the voltage is increased to a higher value.

over time at a certain fixed voltage. The sample can only be brought back to the stepping mode by applying a higher voltage than the voltage previously used on the sample. Figure 4.47 shows data for a SS type sample. The applied voltage was increased in steps, and the sample started showing fluctuations in conductance at 6.6 V. These fluctuations settled down over a time period of ∼8000 s. The fluctuations in the conductance were revitalised once the voltage reached 12.6 V. The voltage required to revitalise conduction steps varies from sample to sample due to the random nature of percolating films. The aging effect discussed above could be due to the consolidation of the critical necks due to electrical annealing. The steps could be revitalised by destabilising the conduction paths by applying higher voltages.

Figure 4.48 shows conductance data for a simple sample from a category 'B' in the tunnelling regime. This sample originally showed stepping behaviour and jumped to various conductance levels as shown Figure 4.38. A voltage ramp over the range of -10 to 10 V was applied. It can be seen that the sample jumps back and forth between the tunnelling and a lower resistance regime when the voltage reaches its maximum absolute value (irrespective of the polarity). This type of behaviour can be explained by the combined effect of electric field induced

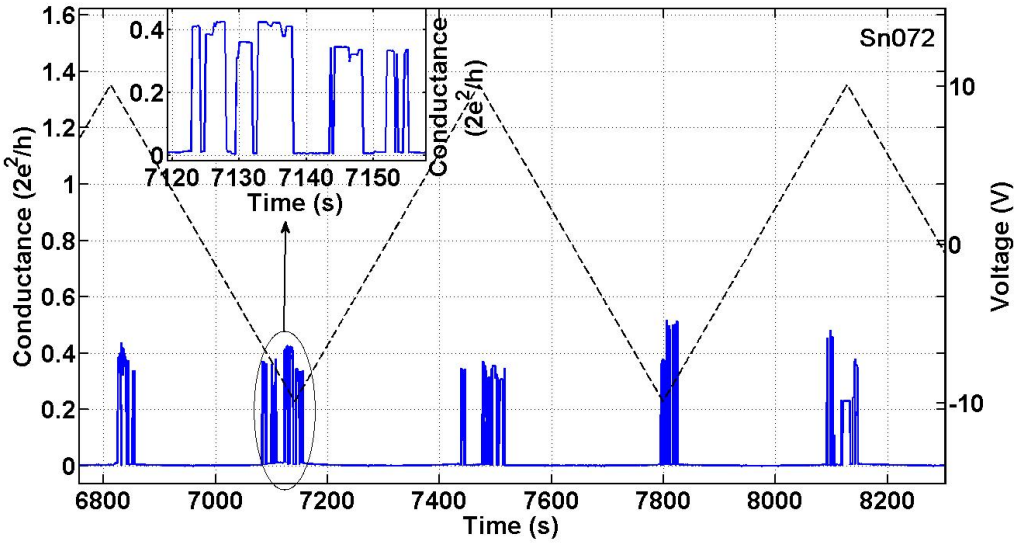

Figure 4.48: Voltage dependence of Stepping behaviour. This SS type shows conductance jumps from tunnelling to contact regime at the point when the applied voltage reaches its absolute maximum value irrespective of the polarity.

evaporation and electromigration. A conducting path could be formed between the nanogaps present in the percolating film due to field induced evaporation showing a step up in conductance. On the other hand, at these high voltages electromigration can break the conducting path due to high current densities, returning the film to a low conductance state.

In some samples the stepping behaviour is voltage-polarity dependent (see Figure 4.39). The polarity dependent stepping/switching could be explained by the formation and breakage of a conducting path due to ion transport caused by a solid state electrochemical reaction (see Section 4.2.7). Suppose that we have a configuration in our thin films similar to one shown in Figure 4.49. Such a situation could arise near the Au/NiCr contacts or between Sn clusters with oxide shells. Sn^{4+} ions can drift within the tin oxide layer on application of a positive bias to the cluster with oxide shell. These diffusing ions can gather on the oxide surface between the gap and form a conducting path. If a negative bias is applied to the cluster with oxide shell, the above mentioned process could be reversed, and the conducting bridge could be broken. A solid state electrochemical reaction, similar to the reaction reported for Ag_2S [167, 149] is proposed in Figure 4.49.

Polarity dependent switching could also be explained by the drift of oxygen

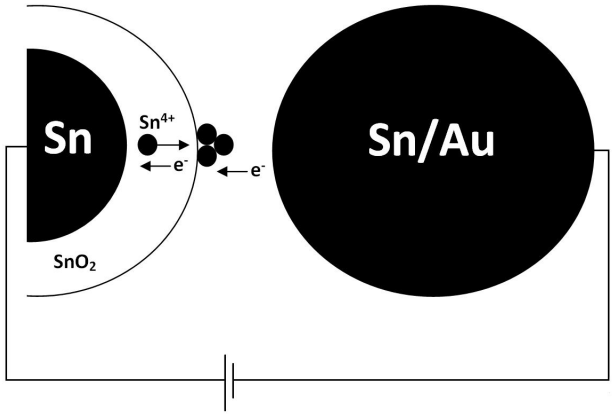

Figure 4.49: Purposed solid state electrochemical reaction creating a Sn conducting path in SnO_2 layer due to migration of Sn^4+ ions toward in the direction of applied electric field.

vacancies in SnO_2 barriers between Sn clusters. Oxygen vacancies in SnO_2 act as a dopant with charge 2+. Shift of these dopants to one side of the barrier due to an applied voltage can expand the depletion region exhibiting a decrease in conductance. By reversing the polarity the dopants can disperse back in whole barrier causing shrinkage of depletion region and hence increase in conductance. Similar switching behaviour has been reported for $Pt/TiO_2/Pt$ systems recently [88, 168].

Diffusivity of oxide vacancies in SnO_{2-x} has been reported to be of the order of 10^{-15} cm^2/s [169]. This value can be used to find the mobility of oxygen vacancies using Einstein's relation [170] as given below:

$$\mu = qD/k_BT \tag{4.19}$$

The above equation gives a value $\sim 4 \times 10^{-14}$ $cm^2/(Vs)$ for mobility. With this mobility a time span of ∼250 ms is required to fully deplete a barrier of SnO_{2-x} with an applied voltage of 1 V across it. This time span is comparable to the time resolution of our data acquisition system and the above mentioned model cannot be ruled out.

Another explanation for reversible steps could be Coulomb blockade (Section 4.2.4). Isolated metallic islands near a nanowire can act as a floating gate [171, 172, 173, 132, 174] in a Field Effect transistor (FET). The electric field produced by the charged island close to the nanowire like structure can cause depletion of the carriers in the wire and decrease its conductance. Once the island is discharged

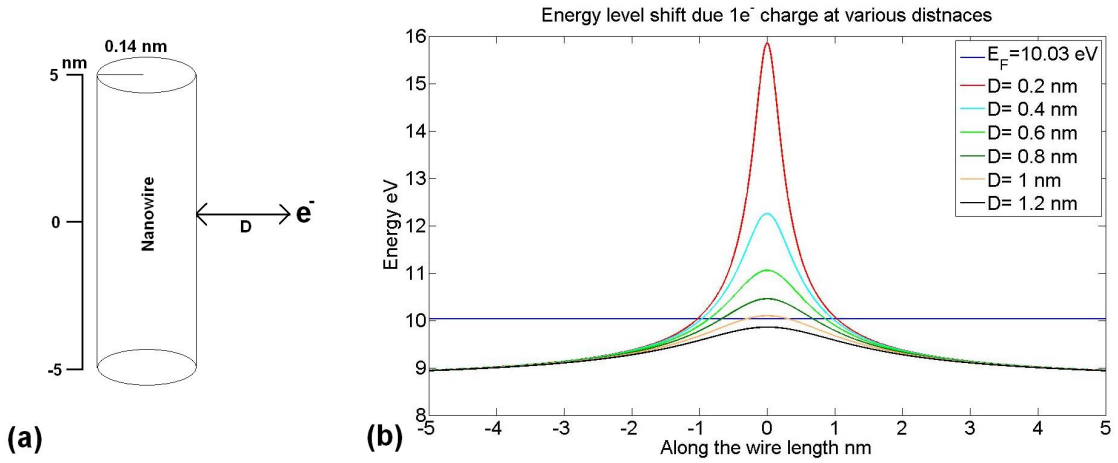

Figure 4.50: (a) A schematic of nanowire that can be depleted due to the electric field of a nearby charge island (not to scale). (b)Bending in minimum allowed energy band of a wire with diameter equal to atomic diameter of Sn due to external electric field. A charge of magnitude $1e^-$ at a distance $\leq$ 1 nm can bend the allowed energy band above the Fermi level (E_F = 10.03 eV for Sn) and deplete it.

the conductance should jump back to its previous higher value. A schematic of a structure showing such mechanism is shown in Figure 4.50(a). This example is just a model where nanowire like structures represent the necks between clusters in the vicinity of an isolated cluster island. Figure 4.50(b) shows that the minimum allowed energy band in an atomic wire is bent due to the external electric field produced by a nearby $1e^-$ charge. A charge of $1e^-$ at a distance less than 1 nm can push the minimum allowed energy state above the Fermi level i.e. 10.03 eV for Sn and hence deplete carriers. Due to the depletion the conductance of wire will decrease dramatically. On removal of this external charge the conductance will increase again to the previous state, showing a switch-like behaviour similar to those visible in the Sn cluster films.

According to these calculations, the maximum distance between the wire and the charge island ought to be of the order of the Sn interplanar distance ($\sim$ 4Å) considering the mean dielectric constant for vacuum and Si_3N_4 to be 3[40]. Therefore, the above model does not seem provide a viable explanation of these data due to such a small wire island separation and could be discarded. However, a charge carrying defect in the oxide shell of a Sn nanowire could fit the above model. Such a model has been proposed as a way of explaining Random Telegraphic Noise (RTN) in the literature [175] but does not fit our conductance switching data.

4.8 Summary

In this chapter, the electrical characterization of Sn films was presented. Sn cluster films deposited under different source conditions show different amount of coalescence. These films were categorized according to their conduction onset behaviour. Generally, different onset behaviours indicate that the samples from different categories have different film morphologies.

The cluster films show interesting conductance steps both during and after the end of deposition. In many cases the steps were found to be quantized with values close to integral multiples of $2e^2/h$. It has been observed that the step behaviour can be initiated by applying an external voltage. Quantized steps during onset and after the end of deposition could be due to the formation of break junction-like structures in the percolating films. Single-atom junctions could readily be formed due to mechanisms like electromigration or field induced evaporation.

It was observed that during the onset, some cluster films jumped to conductance values $1G_0$, $2G_0$, $3G_0$ and so on. It was noted that the film conductance increased in steps during the deposition and stopped increasing at the point where the deposition was stopped. This suggests that incoming clusters were somehow transforming the conductance path causing an increase in conductance. To explain the quantization during the onsets, some plausible scenarios were discussed in Section 4.6.6. It is proposed that the applied voltage causes electric field assisted evaporation and electromigration, forming a single atom contact showing quantized conductance. Though the origins of these quantized steps are believed to be single atom junctions, the precise mechanism of formation of these junctions during the deposition is still an open question and needs further investigation.

After the end of deposition, both reversible and irreversible conductance steps were observed. The probability of occurrence of each type of step was found to be dependent on the source conditions and substrate electrode configuration. Lithographically defined samples with 10 μm electrode separation showed only irreversible steps. On the other hand, samples with 100 μm electrode separation showed both reversible and irreversible steps.

The irreversible steps were also found to occur at conductance values very close to the quantum conductance which suggests that these steps could be due to break-junction-like structures in the cluster films. A critical neck in the film dominating the overall conductance could get thinner due to process like electromigration,

coalescence or Joule heating and ultimately form single atom contacts showing quantized conductance.

Some samples showed reversible steps where the conductance jumps between two or more well defined levels. It was observed that the reversible steps exhibit a dependence on both absolute magnitude and polarity of the applied voltage. These reversible steps can be explained as the formation and breakage of a critical conduction path. Nanogaps are either inherently present in percolating films or formed due to an earlier breakage by electromigration process. Atomic bridges could be formed between these nanogaps by the field evaporated atoms and could be broken by an applied current due to electromigration.

Electrical characterization of Sn cluster films continues in the following chapter. General transport properties and step behaviour are further explored via temperature dependent measurements. An overall conclusion for electrical properties of Sn cluster films is presented Chapter 6.

Chapter 5

Effect of Temperature on Sn Cluster Film Resistivity

In the previous chapter the conductance behaviour of Sn cluster films was investigated using various voltages and different types of substrates. In this chapter, the electrical characterization of Sn films continues. Characterizations were performed at various temperatures to shed more light on the conductivity mechanisms in the cluster films.

Initially, in Section 5.1 a brief introduction to temperature dependent resistivity is given for metals and semiconductors. In Section 5.2 experimental results and discussion are presented. Finally, the chapter concludes with a summary presented in Section 5.3.

5.1 Effect of Temperature on Resistivity

5.1.1 Temperature Dependence of Resistivity of Metals

Bulk Metals : The resistivity of metals varies with temperature primarily due to increase in the number of phonons. However, the minimum resistivity of any sample is temperature independent and that value is defined by the impurities and defects in the lattice.

The Bloch-Grüneisen function provides a good approximation of nonlinear temperature behaviour of resistivity below the Debye temperature and is as fol-

lows [176]:

$$\rho(T) = \rho(0) + A\left(\frac{T}{\Theta_R}\right)^n \int_0^{\frac{\Theta_R}{T}} \frac{x^n}{(e^x - 1)(1 - e^{-x})} dx \tag{5.1}$$

In the equation above the value of n is an integer with value 5 for electron-phonon scattering and 2 for electron-electron interaction. $\rho(0)$, T and Θ_R are residual resistivity, temperature and the Debye temperature respectively. The constant A is dependent on the electron velocities at Fermi surface. Equation 5.1 provides a good fit to our R(T) data obtained during the experiments (see Section 5.2.1).

Thin Films : In addition to the factors affecting the resistivity of bulk metals the resistivity of thin films depends upon factors such as surface scattering (ρ_{ss}), grain boundary scattering (ρ_{gb}) and surface roughness (ρ_{sr}). In percolating films the contact resistance between the interconnecting clusters also plays an important role and has already been discussed in Section 4.6.5. According to Mattheisen rule the resistivity of finite size structures can be expressed as:

$$\rho = \rho_0 + \rho_{ss} + \rho_{gb} + \rho_{sr} \tag{5.2}$$

In thin films where the ratio of thickness to mean free path is $\ll 1$ the resistivity due to surface scattering can be predicted by Fuchs-Sondheimer (F-S) theory [177] and is:

$$\rho_{ss} = \rho_0 \frac{4}{3} \frac{1 - P}{1 + P} \frac{l}{t_f log(l/t_f)} \tag{5.3}$$

where P, t_f and l are the reflection coefficient of film surface, film thickness and mean free path respectively. The resistivity of the thin films depends on temperature because the mean free path l is temperature dependent.

In the case of polycrystalline granular films the resistivity is also affected by the grain boundary scattering. The resistivity due to grain boundary can be estimated using Mayadas-Shatzkes (M-S) theory (see Equation 4.18). In this case the temperature dependence of the resistivity does not deviate much from that of bulk.

However in certain cases the granular films show a negative temperature coefficient of resistivity (TCR). This behaviour can be explained by the model presented by Reiss et al. [178] and is as follows:

$$\rho = (mv_F/ne^2 l_0) s^{-l_0/D} \tag{5.4}$$

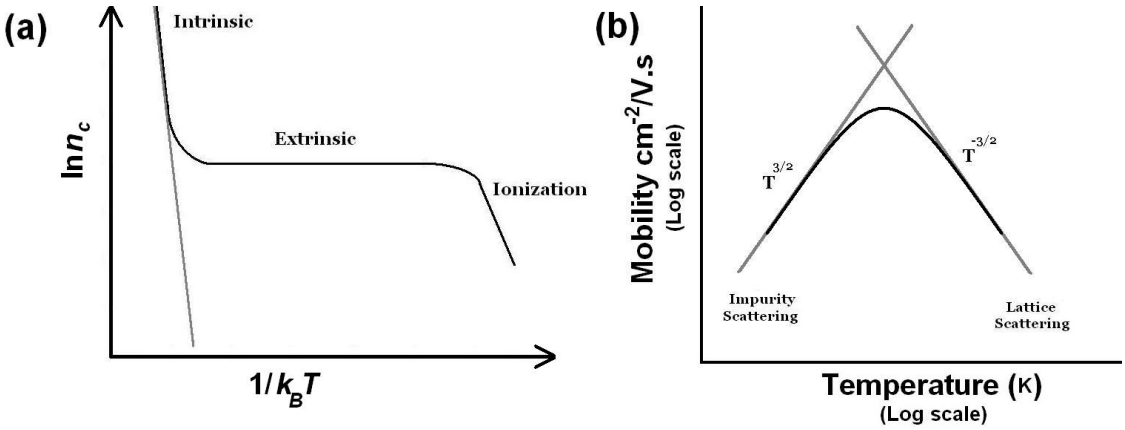

Figure 5.1: (a) Temperature dependence of carrier concentration in doped semiconductors [179]. (b)Temperature dependence of mobility in semiconductors [180].

where m, v_F, n and e represent mass, Fermi velocity, number density and charge of electron respectively. s and D represent the transmission coefficient of the grain boundary and grain size respectively. The above equation yields a negative TCR in a regime where $(l_0/D)ln(1/s)$ is greater than 1.

5.1.2 Resistivity of Semiconductors

The temperature dependence of the resistivity of a semiconductor is more complex than that of metals. The resistivity of semiconductors depends not only on relaxation time but also depends on two other temperature dependent variables i.e. carrier number density n and mobility μ. The diagram in Figure 5.1(a) shows the number density variation with temperature. Figure 5.1(b) shows the temperature dependence of the mobility of the charge carriers in semiconductors which plays an important role in defining resistivity of the material along with the carrier number density. The carrier mobility for non-polar semiconductors such as Silicon (Si) and Germanium (Ge) depends on acoustic phonon scattering at higher temperatures and is directly proportional to $T^{-3/2}$. Ionized impurity scattering is dominant at lower temperatures where the electron speed is much slower and μ is proportional to $T^{3/2}$.

For extrinsic semiconductors the conduction variation can be divided into three regimes. First of all, when the temperature is increased from absolute zero the resistivity of an extrinsic semiconductor decreases. This resistivity decrease is due to the charge carrier's detachment from the donor or acceptors, making them avail-

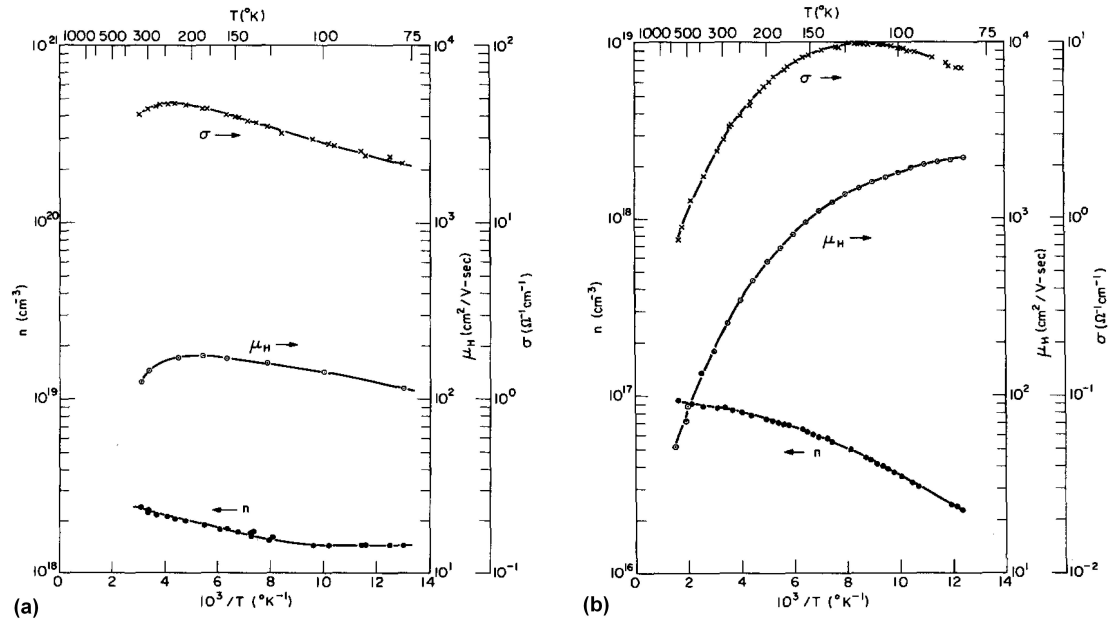

Figure 5.2: Temperature dependence of carrier concentration, mobility and conductivity of single crystal tin oxide sample with (a) low carrier concentration and (b) high carrier concentration [182].

able for conduction. On a further increase in temperature the resistivity increases slightly due to lattice vibrations just like a metal. Finally, due to increasing temperature even further the extrinsic semiconductors behave like intrinsic semiconductors as the carriers jump from the valance band to the conduction band due to temperature and outnumber the carriers present due to doping.

It is interesting to note here that SnO_2 is a semiconductor and there is a good possibility of its presence in our Sn cluster films. Single crystal SnO_2 is a wide band gap semiconductor with $E_g = 3.8$ eV [181]. Just like any other semiconductor the resistivity of tin oxide depends on temperature dependent factors like carrier concentration and mobility as discussed above. The dependence of these factors can be seen in Figure 5.2 which shows the comparison of the samples with high and low carrier concentrations.

5.2 Results and Discussions

Sn cluster films were deposited on SS, L1 and L2 type substrates (see Section 2.3) using the sputter source described in Section 2.1.3. Before analyzing the Sn cluster

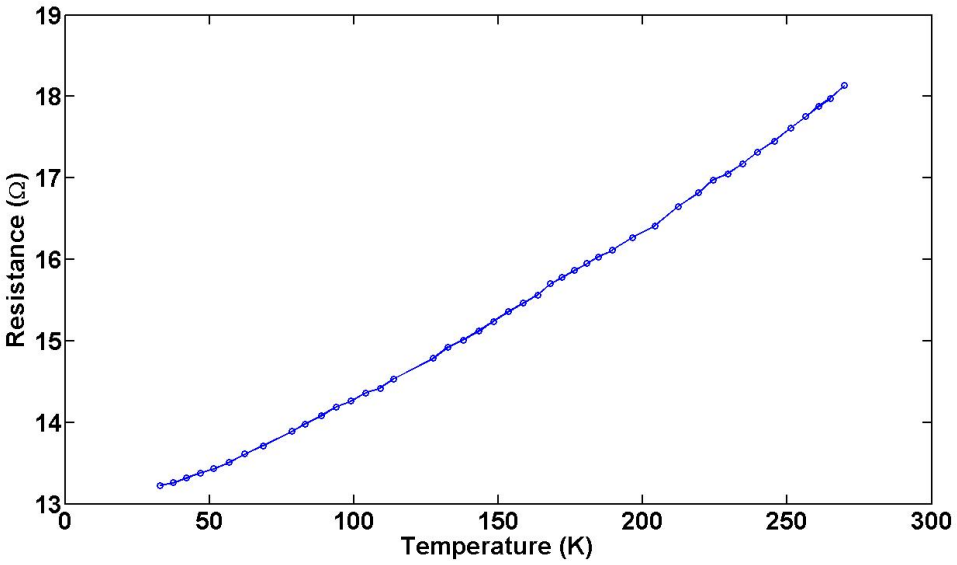

Figure 5.3: Temperature dependence of contact resistance cooled down using liquid helium

films, the resistance of the Au/NiCr contacts[1] was tested at different temperatures ranging from room temperature to LHe temperature. It is clear from Figure 5.3 that the resistance of the contacts is insignificantly low i.e. 13-18 Ω compared to that of Sn cluster films having typical resistances in the range of kΩ.

In the experiments, it was observed that the Sn cluster films show both positive and negative TCR. Moreover, some samples show anomalous temperature dependence of resistivity which cannot be explained by either metallic or semiconductor behaviour. Different source conditions seem to be the reason why some samples show certain types of behaviour. Source pressures are typically in the range of 560, 590 and 630 mTorr for positive, negative and anomalous behaviours respectively. However, exceptions are there and source pressure is merely an indication of other unknown factors in experimental conditions affecting sample behaviour. Table 5.1 summarises the number of sample showing each type of behaviour. Details of temperature behaviour are discussed in following sections.

[1]SS type having no gap between its electrodes was used for this purpose

Substrate type	Total Number of Samples	Positive TCR	Negative TCR	Anomalous Behaviour	RTN Behaviour
SS	10	6	1	3	5
L1	6	5	0	1	0
L2	10	6	2	2	0
Source Pressure mTorr		560	590	630	610

Table 5.1: Summary of number of samples showing various temperature dependent behaviours.

5.2.1 Positive TCR Behaviour

In general, it was observed that cluster films having highly coalesced structures show a positive TCR. Figure 5.4 shows a micrograph of a sample having highly coalesced cluster islands with grain size [2] of ∼100 nm separated by zigzag gaps of $\leq$ 10 nm. The cluster film shown in Figure 5.4 was deposited on a simple sample with an average thickness of 28 nm. It is clear from the resistance-temperature curve shown in Figure 5.5 that the film has a metallic behaviour.

The temperature dependent resistance data was fitted to the Bloch-Grünesein function (Equation 5.1). Figure 5.5 shows the experimental data along with the fitted curve using Equation 5.1. The best fitted curve yielded the following fitting parameters:
$\rho(0) = 70$ nΩm
$A = 320$ nΩm
here $\rho(0)$ is the residual resistivity which is independent of temperature and originates from lattice imperfections (e.g. grain boundaries) and impurities and A is a constant dependent on Debye radius, Fermi velocity and electron number density.

5.2.2 Negative TCR Behaviour

In contrast to the sample discussed in the previous section some cluster films which were deposited at high source pressures (>630 mTorr) showed an increase in resistance with a decreasing temperature. Figure 5.6 shows resistance variations with temperature for an L2 type sample. The resistance of this sample increased to 5 kΩ at 77 K from an initial value of 3 kΩ at room temperature. The sample

[2] Grain size for coalesced films were calculated using technique discussed in Section 2.7.

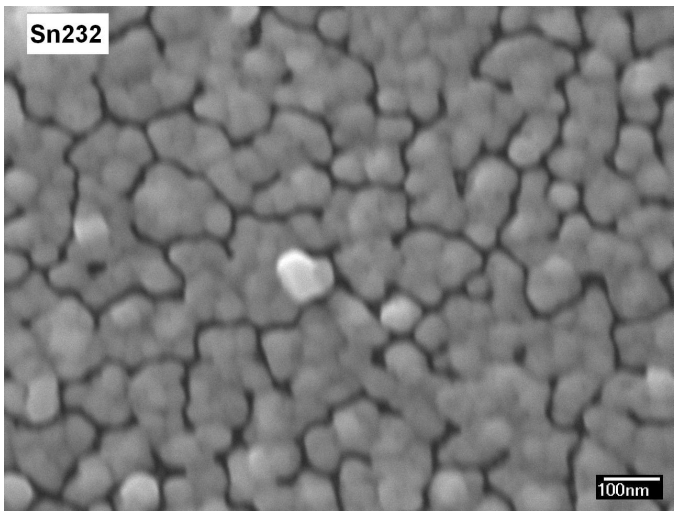

Figure 5.4: SEM micrograph for a sample showing metallic behaviour. The sample was deposited using 0.13 Å/s deposition rate and 566 mTorr Source pressure.

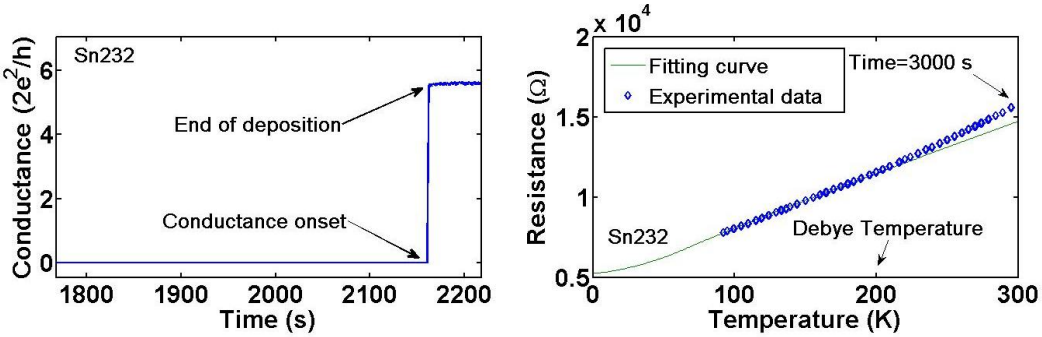

Figure 5.5: An SS type sample with Sn cluster film having 28nm thickness. (Left) Deposition and onset for the sample. (Right) Temperature effect on resistance. The sample shows metallic behaviour with residual resistivity = 69.9 nΩm and residual resistance = 5512 Ω. As expected the Bloch-Grüneisen formula fits for temperatures lower than Debye temperature pretty well.

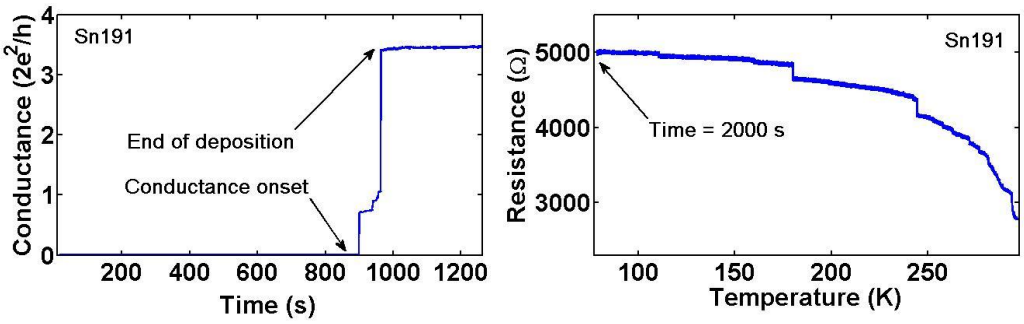

Figure 5.6: Negative TCR behaviour of Sn cluster film deposited on an L2 type sample. (Right) Temperature effect on resistance. (Left) Deposition and onset for the sample.

resistance was recorded for multiple cycles of cooling and warming (between room temperature and 77 K), and each time the sample behaved the same way.

As discussed in Section 5.1.1 the negative TCR could be explained as an effect due to grain boundaries present in the thin films. A less coalesced structure is visible in the SEM micrograph (Figure 5.7)also supports this explanation. Whereas the samples with the usual metallic behavior show coalesced islands with cracks of few nanometers separating those islands from each other (see Figure 4.26).

There are two other possible explanations to the non-metallic behaviour of the film which are worth mentioning here. Firstly, at low temperatures (< 286 K) metallic β-Sn (tetragonal structure) transforms into α-Sn, which is a semiconductor (with diamond structure) [183]. However, this possibility could be ruled out as the transformation of β-Sn into α-Sn in pure Sn is a very slow process. The time span of cooling experiments was of the order of only a few hours which is not enough time for the transformation [184].

Secondly, any presence of oxygen and/or water vapour in the deposition system can oxidize the Sn nanoclusters readily. SnO_2 is a semiconductor which could be the reason for the increase of resistance with decreasing temperatures.

5.2.3 Anomalous Temperature Dependence

As discussed above Sn cluster films show both positive and negative TCR behaviour. Interestingly some samples showed trends with temperature typical of neither metals nor semiconductors. The source pressure for these films was usually >630 mTorr which is high compared to the samples showing positive and negative TCR. The change in resistance of these films due to temperature variations is

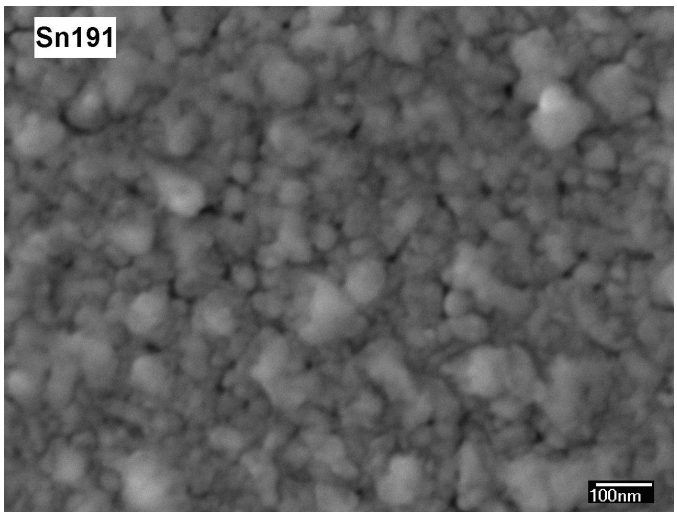

Figure 5.7: SEM micrograph of sample showing non-metallic behaviour with negative TCR. In contrast to the films showing metallic behavior this film does not have coalesced island structure with few nm cracks separating those islands.

also relatively small compared to the samples discussed in Section 5.2.1 and 5.2.2. Figure 5.8 shows the resistance variation for an L2 type sample. The resistance of the sample decreased with the decrease in temperature by only 7% of the original value. It can be seen from Figure 5.9 that the film morphology is different from that of the samples showing positive and negative TCR behaviour.

The resistance of break junction like structures is also independent of the temperature, as the final resistance is due to single-atom connections with perfect transmission. As discussed in Section 4.7.7, Sn cluster films show quantized conduction similar to that of break-junctions. The final resistance of the film under

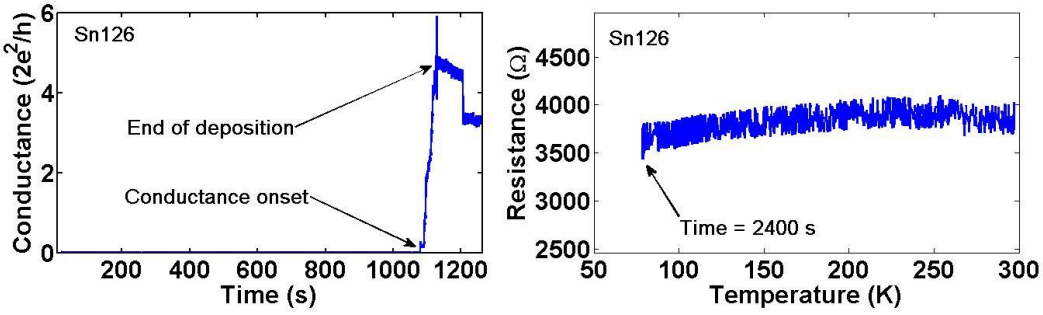

Figure 5.8: Anomalous behaviour of Sn cluster films showing $\leq$5% over all change in resistance over temperature ranging from 273K to 77K. (Right) Temperature effect on resistance. (Left) Deposition and onset for the sample.

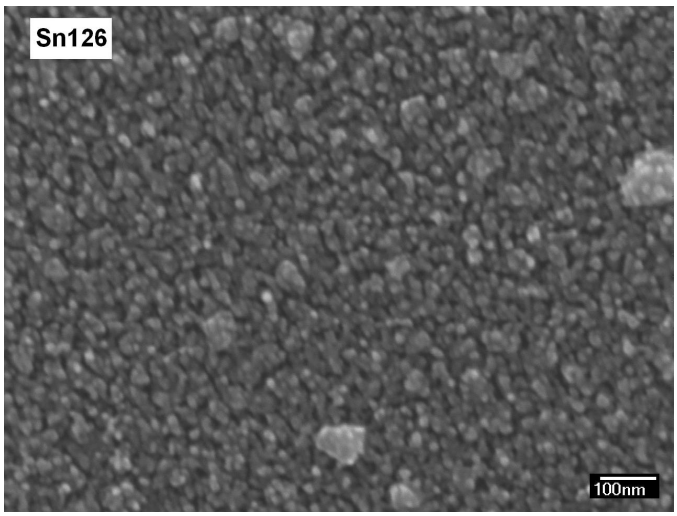

Figure 5.9: SEM micrograph for a sample showing anomalous behaviour.

discussion corresponds to $5G_0$ and could be an indication of ballistic conduction.

5.2.4 Effect of Temperature on Conductance Steps

As discussed in the previous chapter Sn cluster films show interesting steps in conductance. It was observed that this step-wise behaviour shows variations with change in temperature. Figure 5.10 shows the resistance of a simple sample switching between two well-defined levels. The higher level has a resistance of 2.7 MΩ whereas the lower level has a resistance of 37 kΩ. It was observed that the cluster films stopped exhibiting steps in conductance after they were cooled down using LN_2. Figure 5.10 shows data for an SS sample showing conductance steps at room temperature. The sample stops showing the steps when it was cooled down below room temperature and the resistance was locked in the lower resistance level until the sample was heated back to the room temperature. In general, there was no particular cut-off temperature below which the samples did not show steps. However, the probability of steps occurring decreases with a decrease in temperature. The history of the sample (Sn070) being discussed is shown in Figure 5.11.

Resistance variations due to temperature were recorded for both the high resistance level and the low resistance level of the sample discussed above. Interestingly the sample shows opposite trends in the resistance-temperature curves as shown in Figure 5.12. Figure 5.12(a) shows resistance variations for a cooling cycle when the sample was cooled down in the lower resistance state (35 kΩ). At this level

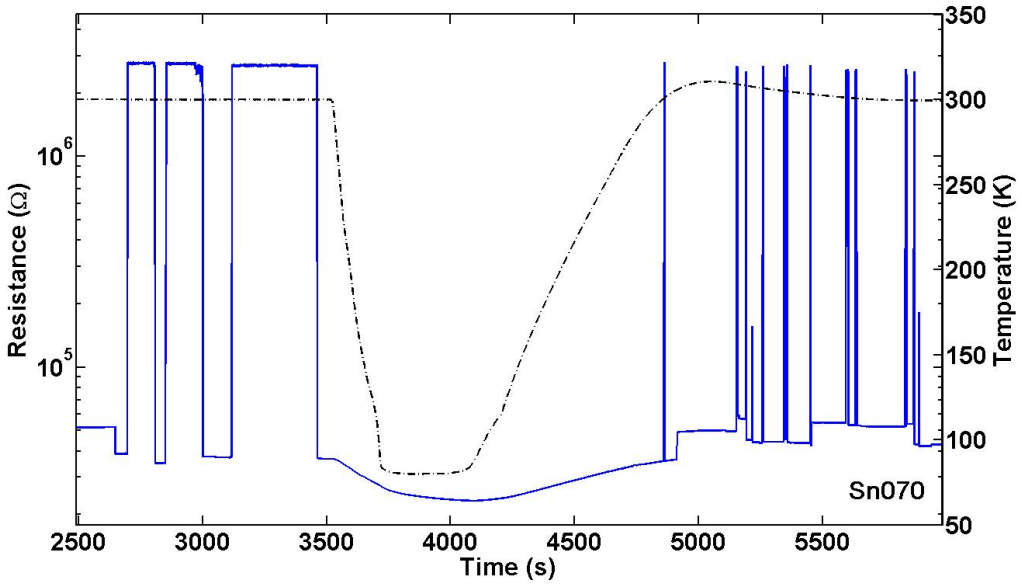

Figure 5.10: The temperature dependence of the resistance steps of a simple sample. The resistance of the sample jumps between various levels. The step behaviour stops once the sample is cooled down using liquid nitrogen.

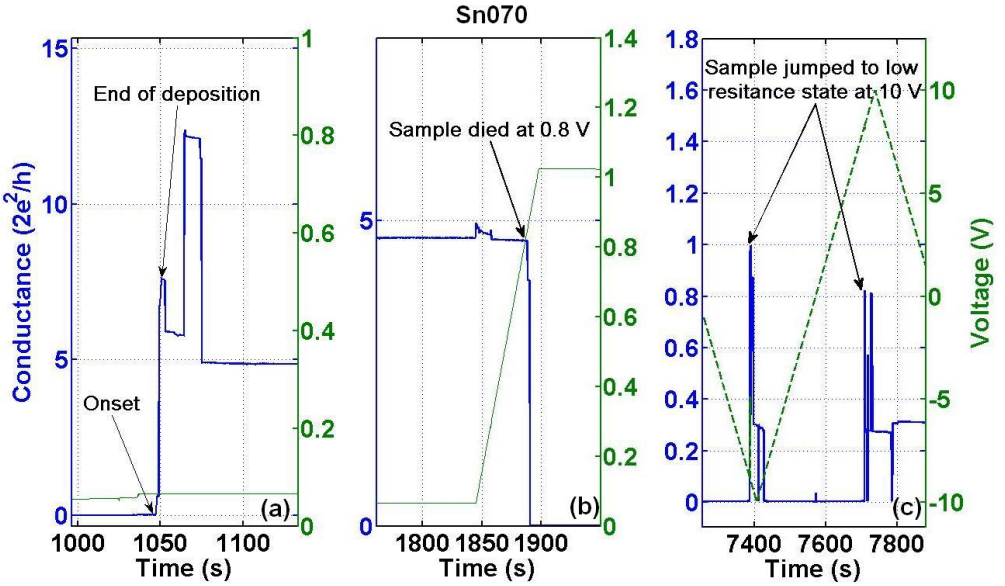

Figure 5.11: Conductance history of Sn070. (a) Onset and after end of deposition conductance behaviour at 50 mV. (b) After the voltage was increased to 0.8 V the sample died. (c) Sample jumped back to high conductance state once the voltage was increased to 10 V.

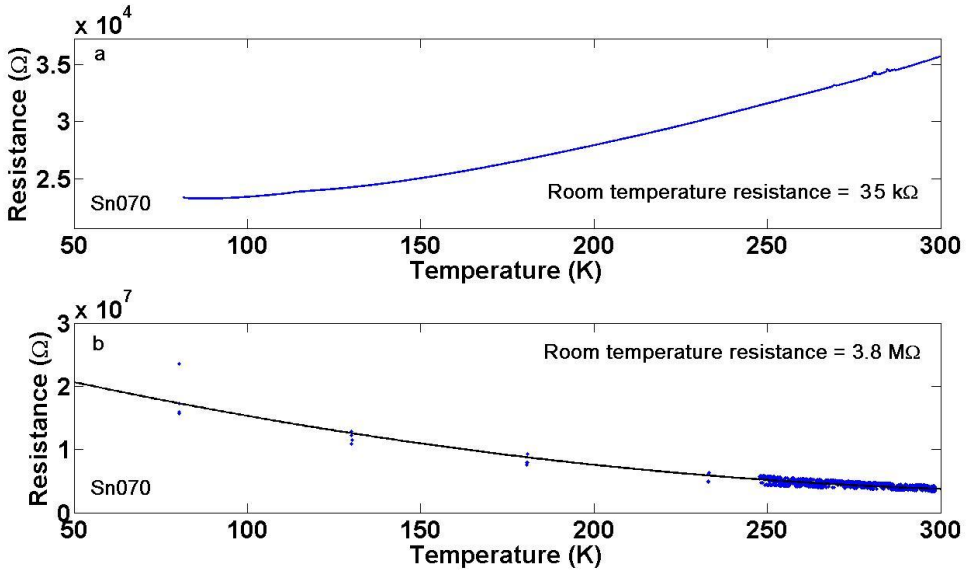

Figure 5.12: (a) Temperature dependence of resistance of sample Sn070 in lower resistance level showing metallic behaviour. (b) The temperature dependence of resistance of sample Sn070 in higher resistance level showing negative TCR behaviour.

the film showed a positive TCR. On the other hand, the same sample showed a negative TCR as the resistance decreased with the increase in temperature when it was in the higher resistance state (3.8 MΩ) as shown in Figure 5.12(b).

Above results indicate that the resistance of the percolating film is due to the switching between contact and tunnelling conductance regime showing positive and negative TCR respectively. This can be explained by the scenario where a physical connection is formed and broken. Furthermore, the higher resistance level shown in Figure 5.12(b) is different from the resistance level observed for the previous cooling cycles shown in Figure 5.10 which suggest that during the breaking process the nanogap formed is slightly different in each switching event.

5.2.5 Random Telegraphic Noise in Sn films

As discussed in Section 4.38 the Sn cluster films show bi-stable conductance steps. These steps can be further divided into clean steps with well defined levels and high frequency Random Telegraphic Noise (RTN) (further details can be found in [41]). The sources of RTN are not well understood. However, one of the sources of the RTN is the phenomenon of trap and release of a carrier at defect sites. Coulomb

blockade discussed in Section 4.2.4 and 4.7.8 could also be a source of RTN.

Figure 5.13(a) shows bi-stable oscillations similar to RTN in the SS type sample at room temperature. On the other hand, at lower temperatures the resistance jumps between well defined levels with much lower frequency compared to that at higher temperatures. A clear transition from one type of behaviour to the other type is visible around 160 K.

If we consider trap and release of carriers as the source of RTN, the probability of an electron being captured or emitted by this trap depends upon the energy barrier and the available energy kT, and can be written as [185]:

$$\frac{t_e}{t_c} = exp(\frac{E_F - E_d}{kT}) \tag{5.5}$$

or

$$ln(\frac{t_e}{t_c}) = \frac{\Delta E}{k}\frac{1}{T} \tag{5.6}$$

here t_e/t_c is the ratio of emission time to capture time. The ratio can be determined from the $R(t)$ plot by finding the ratio of times in the lower resistance state and higher resistance state. On the right hand side of the Equation 5.6 ΔE, k and T are energy barrier of the trap, Boltzmann's constant and temperature respectively.

Figure 5.13(b) shows a plot of $ln(\frac{t_e}{tc})$ versus $1/T$ and is fitted with a straight line. The slope of this line gives the value of ΔE, which in this case is 13 meV. Interestingly Figure 5.13(c) shows the dramatic increase in the frequency of oscillations at $T = 158$ K. This temperature corresponds to an energy of 13.6 meV which is almost same as the trap's energy barrier. The above discussion indicates that the RTN visible in the sample shown in figure 5.13 could be due to a trap with energy barrier with $\Delta E \sim 13$ meV. One of such trap could be an isolated cluster island with charging energy E_c. Considering these cluster islands as spherical capacitors the charging energy is:

$$E_c = \frac{e^2}{8\pi\epsilon_0 R} \tag{5.7}$$

here R is radius of the cluster and ϵ_0 is permittivity of free space. Using 13 meV energy of the trap (causing RTN) in Equation 5.7 the radius of the cluster is calculated which turned out to be $\sim$50 nm. This size is right within the size range of cluster islands constituting our Sn thin films and indicate that the charging and discharging could be the reason behind the RTN. These results also support the proposition of Coulomb blockade being the reason of the conduction step behaviour discussed in Section 4.7.8.

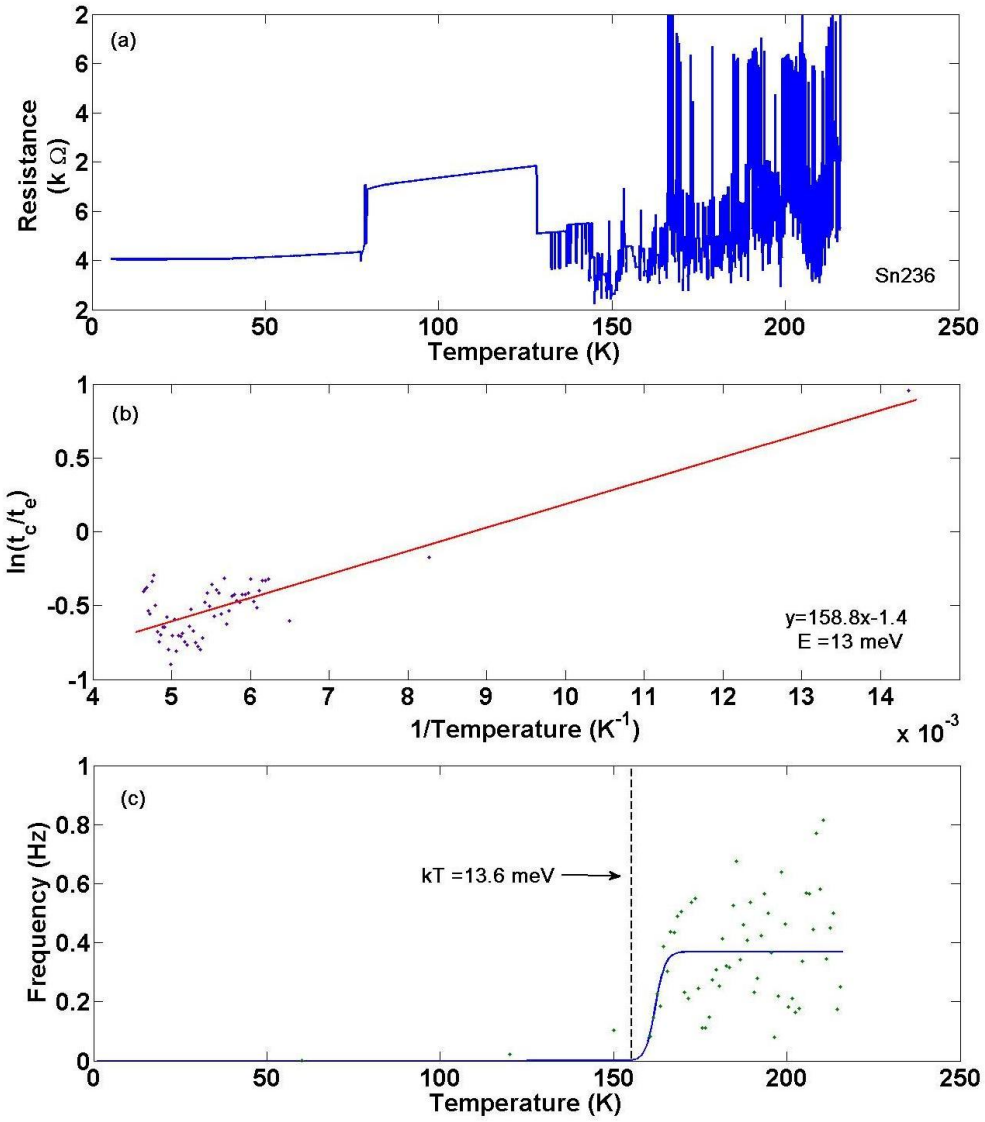

Figure 5.13: Random Telegraphic Noise analysis for Sn percolating sample. (a) Resistance oscillations for range of temperatures. (b) Frequency of oscillation. An exponential increase is triggered after the temperature crossed 158K which corresponds to 13.6 meV. (c) Plot of equation 5.6 showing slop of 158.8 which corresponds to 13meV.

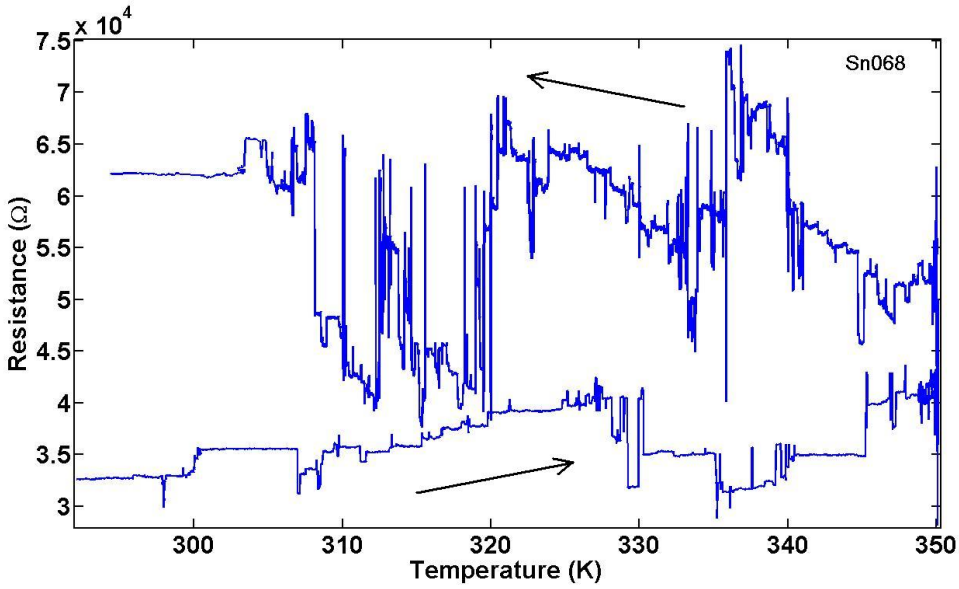

Figure 5.14: Effect of high temperatures on resistance of cluster film of SS type sample.

5.2.6 Resistance Variations at High Temperature

Figure 5.14 shows the effect of temperatures higher than room temperatures on an SS type sample. The temperature was increased from room temperature to 350 K (melting point of bulk Sn is 504 K) and then back to room temperature. The resistance of the film does not show a gradual change in resistance due to increase in temperature. Rather the resistance fluctuated in stepwise fashion as shown in Figure 5.14. Also the overall resistance of the sample increased over time during the heating cycle which could be an indication of structural changes in the film.

It can be seen in Figure 5.14 that the resistance kept on increasing even when the sample was being cooled to room temperature. The increase in resistance does not seem to be due to simple annealing process as annealing should decrease the resistance. The irreversible changes in resistance indicate that the increase in temperature seems to trigger structural changes in the cluster films due to enhanced coalesce/sintering process [44].

5.3 Summary

In this chapter, electrical properties of Sn cluster films were investigated under various temperatures. It was observed that percolating Sn films show a wide range of

temperature dependent electrical responses. Both positive and negative TCR was observed. Films with highly coalesced structures showed typical metallic behaviour which indicates that either there is no oxidation, or oxidation is only limited to the surface and films have a metallic core showing positive TCR. On the other hand, films with less coalesced structures showed a negative TCR indicating the presence of SnO_2 which is a semiconductor. Samples showing switching behaviours were also investigated under varying temperature conditions. The results indicate that the switching behaviour ceased near 77 K. It was also observed that in some samples during switching the higher resistance states was in a tunneling regime showing a negative slope in R vs T curves. R(T) curves showed a positive slope once the sample jumped back to lower resistance state. These observations consolidate the idea that the switching behaviour is due to the formation and breakage of a physical bridge rather than some other peculiar transport phenomenon. RTN was also observed in Sn percolating films showing an onset once the temperature exceeds Debye's Temperature.

Chapter 6

Conclusion and Future Work

The aim of this thesis was to explore the electrical properties of cluster devices. Firstly, the experimental setup was presented followed by the investigation of coalescence in percolating cluster films of Pb and Sn. Subsequently, it was shown that the coalescence in these films plays an important role in defining the electrical properties of the cluster films. The electrical properties being the core of this thesis were discussed in detail using various substrate configurations and applied voltages. Finally, the temperature dependence of the electrical properties was explored.

Coalescence

Sn and Pb cluster films showed a continuous increase in conductance after the end of deposition. This increase in conductance is believed to be due to the growth of the necks forming the percolating path. Several power laws with different numbers of parameters were fitted. Simulations showed that the change in overall conductance of a percolating film can be linked to the coalescence of individual necks between the clusters forming the film. It was shown that the conductance of a percolating film follows the same power law (exponent b) as that of the individual necks (exponent β) forming the film. The neck radius also follows a power law with exponent α which is directly related to β.

Using the power law mentioned above, β for coalescence of Sn and Pb clusters was found to be between 0.01 and 0.03 which corresponds to $0.01 \leq \alpha \leq 0.06$ for Sn and $0.005 \leq \alpha \leq 0.02$ for Pb. These values are similar to the values determined for Bi (i.e. $0.01 \leq \alpha \leq 0.04$). However, these values are much smaller compared

to those reported in the literature. It is believed that the smaller exponents are due to fact that the diffusing atoms are locked in the facets formed during the late stage of coalescence, as observed in previous KMC simulations at UC.

Electrical Characterizations of Sn films

The main focus of this thesis was to explore the electrical properties of Sn cluster films. Sn cluster films deposited under different source conditions show a different amount of coalesce in the final film structures. These films can be categorized according to their conduction onset behaviour. Generally, different onset behaviours indicate that samples from different categories have different film morphologies, and hence the onset curves can be used as a fingerprint for the film structure.

The cluster films show interesting conductance steps both during and after the end of deposition. In many cases, the steps were found to be quantized with values close to integral multiples of $2e^2/h$. It has been observed that after deposition the step behaviour can be initiated by applying an external voltage. Quantized steps during onset and after the end of deposition could be due to the formation of break junction-like structures in the percolating films. Single-atom junctions could readily be formed due to mechanisms like electromigration/field induced evaporation.

It was observed that during the onset some cluster films jumped to conductance values 1_0, 2_0, $3G_0$ and so on. The origin of the upwards steps could be the evolution of the same single atom contact (to two and three conductance channels). It is interesting that the film conductance increases in steps during the deposition and stops at the point where the deposition is stopped. This suggests that incoming clusters are somehow transforming the conductance path. To explain the quantization during the onsets some plausible scenarios were discussed in Section 4.6.6. The applied voltage could cause electric field assisted evaporation and electromigration, forming a single atom contact. Though the origins of these quantized steps are believed to be single atom junctions, the precise mechanism of formation of these junctions during the deposition is still an open question and needs further investigation.

After the end of deposition more conductance steps were observed, which could be divided into two groups i.e. reversible and irreversible steps. The probability of

occurrence of each type of step was found to be dependent on the source conditions and substrate electrode configuration. Lithographically defined samples with 10 μm electrode separation showed only irreversible steps. On the other hand, samples with 100 μm electrode separation showed both reversible and irreversible steps.

The irreversible steps were also found to occur at conductance values very close to the quantum conductance which suggests that these steps could be due to break-junction-like structures in the cluster films. A critical neck in the film dominating the overall conductance could get thinner due to processes like electromigration, coalescence or Joule heating and ultimately form single atom contacts showing quantized conductance.

In temperature dependent studies, both positive and negative TCR behaviour was observed. Some Sn cluster films showed anomalous transport behaviour, which is not obviously either metallic or semiconducting. A very small change in resistivity with temperature was observed for these films. This temperature independence of the resistivity could be an indication of single atom contacts where the electron transmission is perfect and does not depend on material properties. These results corroborate the observed conductance quantization in cluster films.

Some samples also showed reversible steps where the conductance jumps between two or more well defined levels. It was observed that the reversible steps exhibit a dependence on both absolute magnitude and polarity of the applied voltage. These reversible steps could occur either due to physical breakage and formation of conducting paths due to a field effect phenomenon or another mechanism such as Coulomb blockade, which changes the transport properties of the critical necks.

The reversible steps which only depend on the magnitude of the voltage and are independent of polarity can be explained as the formation and breakage of a critical conduction path. Nanogaps are either inherently present in percolating films or formed due to an earlier breakage by electromigration process. Atomic bridges could be formed between these nanogaps by the field evaporated atoms and could be broken by an applied current due to electromigration.

An explanation of the reversible step behaviour which is sensitive to the polarity of the applied voltage could be the formation of atomic protrusions due to the Sn ion migration in a gap separating two adjacent Sn cluster islands with SnO_2 layer around them. Protrusions formed due to ionic currents in solids are well known for materials like Ag_2S. Self diffusion metal ions within their oxides have gained a

lot of interest recently [186, 187, 188]. Self diffusion of Sn^{4+} in SnO2 has also been reported in literature [189]. Moreover, the self diffusion of Sn^{4+} has been reported to be higher than Ag^{+} ions (i.e. 10^{-11}[190] and 10^{-18}[191] at 500K). These facts indicate that a process due to ionic transport analogous to that of Ag_2S systems is also possible in SnO_2.

Another possible explanation for the polarity dependent reversible steps could be the movement of oxygen vacancies in SnO_{2-x} barriers between Sn clusters. These vacancies could act like a dopant with 2+ charge in the SnO_{2-x}. Due to applied voltage the vacancies could move and accumulate on one end of the SnO_2 barrier. This drift of vacancies could cause an in width of the depletion region exhibiting a decrease in conductance (see Figure 4.49). On reversal of polarity the oxygen vacancies could spread back in the SnO_{2-x} layer shrinking the depletion region and hence exhibiting an increase in conductance.

It was found that a time span of 250 ms is required for dopants to traverse a 1 nm wide SnO_{2-x} barrier in order to fully deplete it (based on mobilities of oxygen vacancies in SnO_{2-x} taken from literature). The conductivity in our devices switches from one state to another state showing no intermediate data points at 5 Hz data sampling rate. Hence the switching time in our devices should be <200 ms, which is comparable to the values calculated from oxygen mobilities given in literature. However, the mobilities of SnO_{2-x} are very sensitive to the concentration of oxygen vacancies and other impurities, and further investigation is required to find the exact mobilities in our percolation Sn films. To conclude, it could be said that the explanation for switching conductance based on oxygen drift in SnO_{2-x} seems plausible and cannot be ruled out. However, explanation of reversible steps based on electromigration and electric field evaporation conforms better with our data.

Quantized conductances are a clear indication of single atom bridges. The conductance of these wire-like bridges could be altered due to the electric field of a nearby charged island acting as a gate. Electrons could hop on and off the island due to the potential difference between the wire and the island. The allowed energy levels in such single atom wires are quantized. The bottom of the first allowed sub-band in a nano wire (with radius equals to Sn atomic radius) is 8.66 eV. The bottom of this allowed energy band could be lifted above the Fermi energy (10.03 eV) by the external applied field produced by the charged island, depleting

carriers and decreasing its conductance. The conductance of the wire would rise again once the island is discharged. However, the phenomenon discussed above is only possible if the wire-island distance is of the order of 4 Å, which is similar to inter atomic distance in Sn. The above-mentioned model cannot explain our switching data, however can be useful in explaining RTN.

In Chapter 5 the effect of temperature on the transport properties of Sn films was investigated. Sn cluster films showed both positive and negative TCR behaviour. For highly coalesced films, the resistance followed the Bloch-Grüneisen expression exhibiting metallic behaviour. Grain boundaries seem to be behind the negative TCR shown by some samples. Film structures for these samples are different from other samples showing positive TCR (see Figure 5.7). Sn nanoparticles get oxidized readily and the films showing negative TCR indicate the presence of SnO_2. The presence of SnO_2 in cluster films also supports the model presented in Section 4.7.8 where an ionic current was considered to be the reason of reversible steps by forming and breaking Sn nanowires within a SnO_2 layer. Negative TCR could also be due to the dependence of overall resistance on the tunnel gaps present in the percolating films.

Temperature variations also helped in exploring another aspect of the steps shown by Sn cluster films. Firstly, the probability of steps occurring is close to zero at temperatures below 77 K. It was observed that the samples remained at the conduction level at which they were cooled down. After warming up, the samples started showing step behaviour once again. Secondly, temperature dependent RTN was also observed for samples showing clean step behaviour.

RTN like high frequency reversible steps can be attributed to discrete charging and discharging of clusters or defects due to Coulomb blockade. If such clusters or defects are in the vicinity of a nanowire-like critical neck, they can induce a pinching effect and change the conduction of the whole film. Sn percolating films show a wide variety of structures, and formation of structures showing Coulomb blockade is not out of the question. A charged defect in an oxide shell of Sn nanowire could be a source of RTN. The electromechanical conditioning and relaxation mechanism proposed in Section 4.3 can be discarded because of the film structure observed by SEM. Sn cluster films consist of irregular islands separated by gaps of a few nanometers. In cluster films, no evidence has been found by direct imaging (i.e. SEM or TEM) for existence of the free moving filament like structures proposed

in Section 4.3.

During the experiments, the steps were not completely controllable by the applied voltage even for samples showing continuously reversible steps over many hours. If no steps are visible, an increasing applied voltage enhances the chance of the film beginning to exhibit the step behaviour again. Further investigations of step behaviour of cluster films are still underway. The next section provides some suggestions for future work required to clarify the step-wise conductance behaviour in cluster films.

Future Work

To observe reversible steps in percolating films, it is important to make and break conductance paths in a controllable fashion. Any abrupt or uncontrolled changes could cause a permanent damage to the film rendering it unable to show further steps in conductance. Therefore, the gap formed should be small enough that it could be reconnected using a process like electric field evaporation [146, 147]. Electromigration has been used to make re-connectable nanogaps in the literature (see Section 4.2.6).

An equivalent circuit for a percolating film with a critical neck is shown in Figure 6.1. R_s is the net resistance in series with the critical neck (due to the film itself and due to leads and contacts). R_p represents the parallel resistance due to any possible parallel pathways in the film or an externally applied resistor to control the current and voltage through the critical neck. Careful selection of R_s and R_p is required for controllable breaking of the neck (using an applied current to drive electromigration) and reconnection (by electric field induced evaporation). The following text provides a general outlook on the problem of designing a future experiment that would allow greater control over these processes.

To achieve a smooth breaking behaviour, a voltage source with minimum possible series resistance is ideal [135]. Considering $R_p = \infty$ and a constant voltage supply, the power dissipation across the gap $P(t)$ is

$$P(t) = P_c \left[\frac{1 + R_s/R_n(0)}{1 + R_s/R_n(t)} \right]^2 \tag{6.1}$$

where P_c is critical power needed to break the critical neck. $R_n(0)$ and $R_n(t)$ represent initial neck resistance and the neck resistance at any time t respectively.

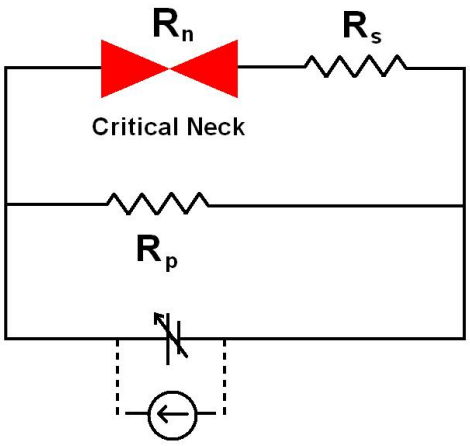

Figure 6.1: An equivalent circuit for a percolating film with a critical neck

According to Equation 6.1 if $R_s \gg R_n(0)$, with an increase in neck resistance the power dissipation across the neck will increase, leading to an unstable breakage. On the other hand, if $R_s \ll R_n(0)$ then P will remain constant leading to a smooth breakage.

Furthermore, active feedback controlled voltage supplies have proven helpful in controlled forming of nanogap [192, 193]. In those cases, the voltage was increased continuously until a critical voltage V^* is reached, and the conductance path became thinner. After reaching the V^*, which is indicated by a sudden decrease in conductance, the voltage was decreased instantaneously to prevent any further uncontrolled damage due to joule heating. V^* is defined as [192]:

$$V^* = \sqrt{\frac{P_n}{G(1 - GR_s)}} \tag{6.2}$$

Here G is the overall conductance of the neck and any series resistance. R_s is the series resistance and P_n is the critical power for the breaking process.

Forming a connection across a nanogap by applying an electric field is complicated due to possible uncontrolled electromigration and heating. If a constant voltage supply is used for inducing field evaporation, the contact formed is more likely to be broken due to high currents. A current source will maintain a constant current through the critical neck (initially due to tunnelling as the neck is open before the bridge is formed). However, in the beginning, due to high initial resistance a high voltage would be required to maintain even small current. This high voltage may be helpful in forming the bridge using field induced evaporation.

In the case of a current source, once a bridge is formed the voltage across the bridge will reduce automatically, and the breakage due to electromigration should be prevented.

Alternatively, a big series resistance (but smaller than that of the nanogap) could be used with a voltage source. In the beginning, all the voltage will drop across the nanogap due to its high resistance, which is useful in terms of field evaporation. After formation of a bridge across the nanogap, the overall resistance of the circuit will decrease, which will result in an increase of overall current. Therefore, in order to form a stable contact the voltage would need to be regulated using an active feedback system, in order to decrease the voltage when needed.

In summary, in the case of a voltage source, smaller series resistances are suitable for breaking of the neck using electromigration. On the other hand, higher resistances are more appropriate with a voltage source for the formation of a bridge across gaps using field induced emission. An active feedback control system seems useful for both cases.

Various explanations and plausible models were proposed in this thesis explaining different phenomenon occurring in the same sample. It will be useful to focus any future experiments on smaller system sizes (e.g L2 type samples) to find and analyse the active necks. Morphology analysis of the regions responsible for stepping, using techniques like SEM, TEM and AFM can help pinpointing the mechanism behind the switching behaviour shown by Sn films.

Bibliography

[1] G. E. Moore. Cramming more components onto integrated circuits. *Electronics*, 38:114, 1965.

[2] M. Ratner and D. Ratner. *Nanotechnology: A gentle introduction to the next big idea.* Prentice Hall, New Jersey, 2002.

[3] K. Mistry, C. Allen, C. Auth, B. Beattie, et al. A 45nm logic technology with high-k+metal gate transistors, strained silicon, 9 Cu interconnect layers, 193 nm dry patterning, and 100% Pb-free packaging. In *Int. El. Devices. Meet. 2007.*

[4] J. R. Powell. The quantum limit to moore's law. *Proc. IEEE*, 96:1247, 2008.

[5] K. Rupp and S. Selberherr. The economic limit to moore's law. *IEEE Trans. Semicond. Manuf.*, 24:1, 2011.

[6] M. Köhler and W. Fritzsche. *Nanotechnology: An Introduction to Nanostructuring Techniques.* Wiley, Germany, 2nd edition, 2007.

[7] G.E. Moore. Lithography and the future of Moore's law. In *Proceedings of SPIE*, volume 2438, page 2, 1995.

[8] S. Y. Chou, P. R. Krauss, and P. J. Renstrom. Nanoimprint lithography. *J. Vac. Sci. Technol. B*, 14:4129, 1996.

[9] W. Zhou and Z. L. Wang. *Scanning Microscopy for Nanotechnology: Techniques and Applications.* Springer, New York, 2007.

[10] S. Amelinckx. *Electron Microscopy: Principles and Fundamentals.* Wiley-VCH, 2008.

[11] D. M. Eigler and E. K. Schweizer. Positioning single atoms with a scanning tunnelling microscope. *Nature*, 344:524, 1990.

[12] D. Mijatovic, J. C. T. Eijkel, and A. van den Berg. Technologies for nanofluidic systems: top-down vs. bottom-up -a review. *Lab Chip*, 5:492, 2005.

[13] S. A. Scott. *Self-Assembly of Sb and Bi Nanostructures of Graphite*. PhD thesis, University of Canterbury, 2005.

[14] J. Y. Cheng, C. T. Rettner, D. P. Sanders, H. Kim, and W. D. Hinsberg. Dense self-assembly on sparse chemical patterns: Rectifying and multiplying lithographic patterns using block copolymers. *Adv. Mater.*, 20:3155, 2008.

[15] J. G. Partridge, S. A. Brown, A. D. F. Dunbar, R. Reichel, M. Kaufmann, C. Siegert, S. Scott, and R. J Blaikie. Templated-assembly of conducting antimony cluster wires. *Nanotechnology*, 15:1382, 2004.

[16] D. Mackenzie. *Bismuth and Germanium Nanoscale Cluster Devices*. PhD thesis, University of Canterbury, 2010.

[17] P. Jena and A.W. Castleman Jr. *Nanoclusters: A Bridge Across Disciplines*, volume 1. Elsevier, 2011.

[18] K. C. Tee, A. Lassesson, J. van Lith, S. A. Brown, J. G. Partridge, M. Schulze, and R. J. Blaikie. Selective filling and sintering of copper nanoclusters for interconnect. *IEEE T. Nanotechnol.*, 6:556, 2007.

[19] S. L. Lai, J. Y. Guo, V. Petrova, G. Ramanath, and L. H. Allen. Size-dependent melting properties of small tin particles: Nanocalorimetric measurements. *Phys. Rev. Lett.*, 77:99, 1996.

[20] W. H. Qi and M. P. Wang. Size effect on the cohesive energy of nanoparticle. *J. Mater. Sci. Lett.*, 21:1743, 2002.

[21] W. H. Qi. Size effect on melting temperature of nanosolids. *Physica B: Condensed Matter*, 368:46, 2005.

[22] M. Strongin, R. S. Thompson, O. F. Kammerer, and J. E. Crow. Destruction of superconductivity in disordered near-monolayer films. *Phys. Rev. B*, 1:1078, 1970.

[23] A. P. Tsai, N. Chandrasekhar, and K. Chattopadhyay. Size effect on the superconducting transition of embedded lead particles in an Al–Cu–V amorphous matrix. *Appl. Phys. Lett.*, 75:1527, 1999.

[24] W. H. Li, C. C. Yang, F. C. Tsao, and K. C. Lee. Quantum size effects on the superconducting parameters of zero-dimensional Pb nanoparticles. *Phys. Rev. B*, 68:184507, 2003.

[25] M. Ido. Fluctuation effect on the knight shift of superconducting Al fine particles. *J Phys. Soc. Jap.*, 41:412, 1976.

[26] M. Strongin, O. F. Kammerer, and A. Paskin. Superconducting transition temperature of thin films. *Phys. Rev. Lett.*, 14:949, 1965.

[27] R. Busnai, M. Folkers, and O. Cheshnovsky. Direct observation of band-gap closure in mercury clusters. *Phys. Rev. Lett.*, 81:3836, 1998.

[28] D. Astruc. *Nanoparticles and catalysis.* Wiley-VCH, Germany, 2008.

[29] F. E. Kruis, H. Fissan, and A. Peled. Synthesis of nanoparticles in the gas phase for electronic, optical and magnetic applications–a review. *J. Aerosol Sci.*, 29:511, 1998.

[30] R. Reichel, J. G. Partridge, A. D. F. Dunbar, S. A. Brown, O. Caughley, and A. Ayesh. Construction and application of a UHV compatible cluster deposition system,. *J. Nanopart. Res.*, 8:405, 2006.

[31] R. Reichel, J. G. Partridge, F. Natali, T. Matthewson, S. A. Brown, A. Lassesson, D. M. A. Mackenzie, A. I. Ayesh, K. C. Tee, A. Awasthi, and S. C. Hendy. From the adhesion of atomic clusters to the fabrication of nanodevices. *Appl. Phys. Lett.*, 89:213105, 2006.

[32] A. Lassesson, M. Schulze, J. van Lith, and S. A. Brown. Tin oxide nanocluster hydrogen and ammonia sensors. *Nanotechnology*, 18:15502, 2007.

[33] D. Stauffer and A. Aharony. *Introduction to Percolation Theory.* Taylor and Francis, London, 2nd edition, 1992.

[34] S. R. Broadbent and J. M. Hammersley. Percolation processes. *Math. Proc. Cambridge Phil. Soc.*, 53:629, 1957.

[35] S. Kirkpatrick. Percolation and conduction. *Rev. Mod. Phys.*, 45:574, 1973.

[36] H. Nanto, T. Minami, and S. Takata. Zinc-oxide thin-film ammonia gas sensors with high sensitivity and excellent selectivity. *J. Appl. Phys.*, 60:482, 1986.

[37] M. Kanamori, K. Suzuki, and T. Yamada. Time-dependent changes in resistivity of SnO_2 thin films in air with water vapor or reducing gas. *J. Ceram. Soc. Jpn.*, 103:1258, 1995.

[38] G. Korotcenkov. Gas response control through structural and chemical modification of metal oxide films: state of the art and approaches. *Sensor. Actuat. B Chem.*, 107:209, 2005.

[39] N. Barsan, D. Koziej, and U. Weimar. Metal oxide-based gas sensor research: How to? *Sensor. Actuat. B. Chem.*, 121:18, 2007.

[40] A. Lassesson, S. A. Brown, J. van Lith, and M. Schulze. Electrical characterization of gold island films: A route to control of nanoparticle deposition. *Appl. Phys. Lett.*, 93:203111, 2008.

[41] S. Gourley. Electronic properties of cluster deposited bismuth nanowires. Master's thesis, University of Canterbury, 2002.

[42] F. Natali. I-V measurements for V-groove self-assembled Bi nanowires. *To be published.*

[43] M. E. Toimil-Molares, A. G. Balogh, T. W. Cornelius, R. Neumann, and C. Trautmann. Fragmentation of nanowires driven by Rayleigh Instability. *Appl. Phys. Lett.*, 85:5337, 2004.

[44] D. N. McCarthy. *Nucleation and Equilibrium via Surface Diffusion: An Experimental Study.* PhD thesis, University of Canterbury, 2008.

[45] P. Y. Convers, D. N. McCarthy, A. Sattar, F. Natali, S. C. Hendy, and S. A. Brown. Electrical signature of nanoscale coalescence in a percolating Bi nanocluster film. *Phys. Rev. B*, 82:115409, 2010.

[46] A. I. Ayesh, A. Lassesson, S. A. Brown, A. D. F. Dunbar, M. Kaufmann, J. G. Partridge, R. Reichel, and J. van Lith. Experimental and simulational

study of the operation conditions for a high transmission mass filter. *Rev. Sci. Inst.*, 78:053906, 2007.

[47] K. Jousten. *Handbook of vacuum technology.* Wiley-VCH, Germany, 2006.

[48] J. F. O'Hanlon. *A user's guide to vacuum technology.* John Wiley & Sons, Canada, 2003.

[49] H. Haberland. *Clusters of atoms and molecules : theory, experiment, and clusters of atoms.* Springer-Verlag, New York, 1994.

[50] P. J. Kelly and R. D. Arnell. Magnetron sputtering: a review of recent developments and applications. *Vacuum*, 56:159, 2000.

[51] D. M. Mattox. *Handbook of Physical Vapour Deposition (PVD) Processing.* Elsevier Inc., USA, 2010.

[52] R. Behrisch and W. Eckstein. *Sputtering by particle bombardment.* Springer, Germany, 2007.

[53] A. Ayesh. *Device fabrication using Bi nanoclusters.* PhD thesis, University of Canterbury, 2007.

[54] B. von Issendorff and R. E. Palmer. A new high transmission infinite range mass selector for cluster and nanoparticle beams. *Rev. Sci. Inst.*, 70:4497, 1999.

[55] J. L. Corkill, A. Garca, and M. L. Cohen. Theoretical study of high-pressure phases of tin. *Phys. Rev. B*, 43:9251, 1991.

[56] H. L. Needleman and D. Bellinger. The health effects of low level exposure to lead. *Annu. Rev. Publ. Health*, 12:111, 1991.

[57] W. Hinsberg, F. A. Houle, and J. Hoffnagle. Deep-ultraviolet interferometric lithography as a tool for assessment of chemically amplified photoresist performance. *J. Vac. Sci. Technol. B*, 16:3689, 1998.

[58] J. Goldstein. *Scanning electron microscopy and X-ray microanalysis: a text for biologists, materials scientists, and geologists.* Plenum press, New York, 1981.

[59] J. Heydenreich. *High-Resolution Transmission Electron Microscopy and Associated Techniques*. Oxford, New York, 1990.

[60] A. Okazaki, K. Maruyama, K. Okumura, Y. Hasegawa, and S. Miyazima. Critical exponents of a two-dimensional continuum percolation system. *Phys. Rev. E*, 54:3389, 1996.

[61] ImageJ, http://imagej.nih.gov/ij.

[62] K. Hansen, S. K. Nielsen, E. Lægsgaard, I. Stensgaard, and F. Besenbacher. Fast and accurate current-voltage curves of metallic quantum point contacts. *Rev. Sci. Instrum.*, 71:1793, 2000.

[63] M. José-Yacamán, C. Gutierrez-Wing, M. Miki, D.Q. Yang, K. N. Piyakis, and E. Sacher. Surface diffusion and coalescence of mobile metal nanoparticles. *J. Phys. Chem. B*, 109:9703, 2005.

[64] G. C. Kuczynski. Study of the sintering of glass. *J. Appl. Phys.*, 20:1160, 1949.

[65] W.W. Mullins. Theory of thermal grooving. *J. Appl. Phys.*, 28(3):333, 1957.

[66] R. L. Coble. Sintering crystalline solids. II. experimental test of diffusion models in powder compacts. *J. Appl. Phys.*, 32:793–799, 1961.

[67] F. A. Nichols and W. W. Mullins. Morphological changes of a surface of revolution due to capillarity-induced surface diffusion. *J. Appl. Phys.*, 36:1826, 1965.

[68] F. A. Nichols. Coalescence of two spheres by surface diffusion. *J. Appl. Phys.*, 37:2805, 1966.

[69] J. R. Blachere, A. Sedehi, and Z. H. Meiksin. Sintering of sub-micron metallic particles. *J. Mater. Sci.*, 19:1202, 1984.

[70] J. Eggers. Coalescence of spheres by surface diffusion. *Phys. Rev. Lett.*, 80:2634, 1998.

[71] T. Hawaa and M.R. Zachariaha. Coalescence kinetics of unequal sized nanoparticles. *Aerosol Sci. B*, 37:1, 2006.

[72] G. Ehrlich and F. G. Hudda. Atomic view of surface self-diffusion: Tungsten on tungsten. *J. Chem. Phys.*, 44:1039, 1966.

[73] G. Ayrault and G. Ehrlich. Surface self-diffusion on an FCC crystal: An atomic view. *J. Chem. Phys.*, 60:281, 1974.

[74] M. Bott, M. Hohage, M. Morgenstern, T. Michely, and G. Comsa. New approach for determination of diffusion parameters of adatoms. *Phys. Rev. lett.*, 76:1304, 1996.

[75] R. Theissmann, M. Fendrich, R. Zinetullin, G. Guenther, G. Schierning, and D. E. Wolf. Crystallographic reorientation and nanoparticle coalescence. *Phys. Rev. B*, 78:205413, 2008.

[76] J. H. Dedrick and G. C. Kuczynski. Electrical conductivity method for measuring self-diffusion of metals. *J. Appl. Phys.*, 21:1224, 1950.

[77] M. Massachi. Contact resistance studies of sintering using ultra clean copper surfaces in ultrahigh vacuum. *J. Appl. Phys.*, 48:1408, 1977.

[78] D. L. Peng, T. J. Konno, K. Wakoh, T. Hihara, and K. Sumiyama. Co cluster coalescence behavior observed by electrical conduction and transmission electron microscopy. *Appl. Phys. Lett.*, 78:1535, 2001.

[79] R. Holm. *Electric Contacts Theory and Application*. Springer, New York, 4 edition, 1967.

[80] Y. V. Sharvin. A possible method for studying fermi surfaces. *Sov. Phys. JETP*, 21:655, 1965.

[81] L. J. Lewis, P. Jensen, and J. Barrat. Melting, freezing, and coalescence of gold nanoclusters. *Phys. Rev. B*, 56:2248, 1997.

[82] N. Lummen and T. Kraska. Molecular dynamics investigations of the coalescence of iron clusters embedded in an inert-gas heat bath. *Phys. Rev. B*, 71:205403, 2005.

[83] J. Schmelzer, S. A. Brown, A. Wurl, M. Hyslop, and R. J. Blaikie. Finite-size effects in the conductivity of cluster assembled nanostructures. *Physical Review Letters*, 88:226802, 2002.

[84] P. Y. Convers, A. Sattar, S. A. Brown, and S. C. Hendy. Power law fitting procedures: The electrical conductance of coalescing nanocluster films. *J. Appl. Phys.*, 109, 2011.

[85] L. J. Challis. Physics in less than three dimensions. *J. Contemp. Phys.*, 33:11, 1992.

[86] L. O. Chua. Memristor: The missing circuit element. *IEEE Trans. Circuit Theory*, 18:507, 1971.

[87] L. O. Chua and S. M Kang. Memristive devices and systems. *Proc. IEEE*, 64:209, 1976.

[88] D. B. Strukov, G. S. Snider, D. R. Stewart, and R. S. Williams. The missing memristor found. *Nature*, 453:80, 2008.

[89] B. Widrow. An adaptive "adaline" neuron using chemical "memristors". Technical report, Stanford Electronics Laboratories, 1960.

[90] J. G. Simmons and R. R. Verderber. New conduction and reversible memory phenomena in thin insulating films. *Proc. R. Soc. A*, 301:77, 1967.

[91] F. Argall. Switching phenomena in titanium oxide thin films. *Solid State Electron.*, 11:535, 1968.

[92] G. Dearnaley, A. M. Stoneham, and D. V. Morgan. A model for filament growth and switching in amorphous oxide films. *J. Non-Cryst. Solids*, 4:593, 1970.

[93] S. Thakoor, A. Moopenn, T. Daud, and A. P. Thakoor. Solid-state thin-film memistor for electronic neural networks. *J. Appl. Phys.*, 67:3132, 1990.

[94] R. Johnson and S. R. Ovhsinsky. Method for making, parallel reprogramming or field programming of electronic matrix arrays. *US Patent*, (4597162).

[95] Y. G. Kriger, N. F. Yudanov, I. K. Igumenov, and S. B. Vashchenko. Study of test structures of a molecular memory element. *J. Struct. Chem.*, 34:966, 1993.

[96] F. A. Buot and A. K. Rajagopal. Binary information storage at zero bias in quantum-well diodes. *J. Appl. Phys.*, 76:5552, 1994.

[97] J. J. Yang, M. D. Pickett, X. Li, D. A. A. Ohlberg, D. R. Stewart, and R. S. Williams. Memristive switching mechanism for metal//oxide//metal nanodevices. *Nat. Nano.*, 3:429, 2008.

[98] J. Borghetti, G. S. Snider, P. J. Kuekes, J. J. Yang, D. R. Stewart, and R. S. Williams. memristive switches enable stateful logic operations via material implication. *Nature*, 464:873, 2010.

[99] T. Prodromakis and C. Toumazou. A review on memristive devices and applications. In *ICECS*, page 934, 2010.

[100] K. Nichogi, A. Taomoto, S. Asakawa, and K. Yoshida. Artificial neural function circuit having organic thin film elements. *US Patent*, (5223750), 1993.

[101] M. N. Kozicki and W. C. West. Programmable metallization cell structure and method of making same. *US Patent*, (5914893), 1998.

[102] P. J. Kuekes, R. S. Williams, and J. R. Heath. Molecular wire crossbar memory. *US Patent*, (6128214), 2000.

[103] S. Genrikh, C. Cho, I. Yoo, E. Lee, S. Cho, and C. Moon. Electrode structure having at least two oxide layers and non-volatile memory device having the same. *US Patent*, (7417271).

[104] B. L. Mouttet. Programmable crossbar signal processor used as morphware. *US Patent*, (7447828), 2008.

[105] D. R. Stewart, P. A. Beck, and D. A. Ohlberg. Non-volatile programmable impedance nanoscale devices. *US Patent*, (7443711), 2008.

[106] G. Anthes. Memristor: Pass or fail? *Commun. ACM*, 54:22, 2010.

[107] J. K. Gimzewski and R. Möller. Transition from the tunneling regime to point contact studied using scanning tunneling microscopy. *Phys. Rev. B*, 36:1284, 1987.

[108] B. J. van Wees, H. van Houten, C. W. J. Beenakker, J. G. Williamson, L. P. Kouwenhoven, D. van der Marel, and C. T. Foxon. Quantized conductance

of point contacts in a two-dimensional electron gas. *Phys. Rev. Lett.*, 60:848, 1988.

[109] DA Wharam, TJ Thornton, R. Newbury, M. Pepper, Ahmed, et al. One-dimensional transport and the quantisation of the ballistic resistance. *J. Phys. C*, 21:209, 1988.

[110] J. L. Costa-Krämer, N. Garcia, P. Garcia-Mochales, and P. A. Serena. Nanowire formation in macroscopic metallic contacts: quantum mechanical conductance tapping a table top. *Surf. Sci.*, 342:1144, 1995.

[111] J. I. Pascual, J. Méndez, J. Gómez-Herrero, A. M. Baró, N. Garcia, and Vu Thien Binh. Quantum contact in gold nanostructures by scanning tunneling microscopy. *Phys. Rev. Lett.*, 71:1852, 1993.

[112] H. van Houten and C. Beenakker. Quantum point contacts. *Phys. Today*, 49:22, 1996.

[113] D. M. Kim. *Introductory quantum mechanics for semiconductor nanotechnology*. Wiley-VCH, Germany, 2010.

[114] N. Agrait, J. G. Rodrigo, and S. Vieira. Conductance steps and quantization in atomic-size contacts. *Phys. Rev. B*, 47:12345, 1993.

[115] A. M. Bratkovsky, A. P. Sutton, and T. N. Todorov. Conditions for conductance quantization in realistic models of atomic-scale metallic contacts. *Phys. Rev. B*, 52:5036, 1995.

[116] J. M. Krans, J. M. van Ruitenbeek, V. V. Fisun, I. K. Yanson, and L. J. de Jongh. The signature of conductance quantization in metallic point contacts. *Nature*, 375:767, 1995.

[117] C. J. Muller, J. M. Krans, T. N. Todorov, and M. A. Reed. Quantization effects in the conductance of metallic contacts at room temperature. *Phys. Rev. B*, 53:1022, 1996.

[118] G. Rubio, N. Agrait, and S. Vieira. Atomic-sized metallic contacts: Mechanical properties and electronic transport. *Phys. Rev. Lett.*, 76:2302, 1996.

[119] H. Yasuda and A. Sakai. Conductance of atomic-scale gold contacts under high-bias voltages. *Phys. Rev. B*, 56:1069, 1997.

[120] H. E. van den Brom, A. I. Yanson, and J. M. van Ruitenbeek. Characterization of individual conductance steps in metallic quantum point contacts. *Physica B*, 252:69, 1998.

[121] H. Ohnishi, Y. Kondo, and K. Takayanagi. Quantized conductance through individual rows of suspended gold atoms. *Nature*, 395:780, 1998.

[122] M. R. Sorensen, M. Brandbyge, and K. W. Jacobsen. Mechanical deformation of atomic-scale metallic contacts: structure and mechanisms. *Phys. Rev. B*, 57:3283, 1998.

[123] J. L. Costa-Krämer. Conductance quantization at room temperature in magnetic and nonmagnetic metallic nanowires. *Phys. Rev. B*, 55:4875, 1997.

[124] J. M. Krans, C. J. Muller, I. K. Yanson, Th. C. M. Govaert, R. Hesper, and J. M. van Ruitenbeek. One-atom point contacts. *Phys. Rev. B*, 48:14721, 1993.

[125] J. M. Krans and J. M. van Ruitenbeek. Subquantum conductance steps in atom-sized contacts of the semimetal Sb. *Phys. Rev. B*, 50:17659, 1994.

[126] C. J. Muller, J. M. van Ruitenbeek, and L. J. de Jongh. Conductance and supercurrent discontinuities in atomic-scale metallic constrictions of variable width. *Phys. Rev. Lett.*, 69:140, 1992.

[127] A. I. Yanson. *Atomic chains and electronic shells: quantum mechanism for the formation of nanowires.* PhD thesis, University of Leiden, 1975.

[128] T. A. Fulton and G. J. Dolan. Observation of single-electron charging effects in small junctions. *Phys. Rev. Lett.*, 59:109, 1987.

[129] M. A. Kastner. The single-electron transistor. *Rev. Mod. Phys.*, 64:849, 1992.

[130] A. Nakajima, T. Futatsugi, K. Kosemura, T. Fukano, and T. Yokoyama. Room temperature operation of Si single-electron memory with self-aligned floating dot gate. *Appl. Phys. Lett.*, 70:1742, 1997.

[131] C. Wasshuber, H. Kosina, and S. Selberherr. A comparative study of single-electron memories. *IEEE Trans. Electron Devices*, 45:2365, 1998.

[132] Ishii T. Sano T. Mine T. Murai F. Hashimoto T. Kobayashi T. Kure T. Yano, K. and K. Seki. Single-electron memory for giga-to-tera bit storage. *Proc. IEEE*, 87:633, 1999.

[133] C. Stampfer, E. Schurtenberger, F. Molitor, J. Guttinger, T. Ihn, and K. Ensslin. Tunable graphene single electron transistor. *Nano Lett.*, 8:2378, 2008.

[134] C. Y. Liu, C. Chen, and K. N. Tu. Electromigration in Sn-Pb solder strips as a function of alloy composition. *J. Appl. Phys.*, 88, 2000.

[135] M. L. Trouwborst, S. J. van der Molen, and B. J. van Wees. The role of joule heating in the formation of nanogaps by electromigration. *J. Appl. Phys.*, 99:114316, 2006.

[136] H. C. Yu, S. H. Liu, and C. Chen. Study of electromigration in thin tin film using edge displacement method. *J. Appl. Phys.*, 98:13540, 2005.

[137] H. Park, A. K. L. Lim, A. P. Alivisatos, J. Park, and P. L. McEuen. Fabrication of metallic electrodes with nanometer separation by electromigration. *Appl. Phys. Lett.*, 75:301, 1999.

[138] W. Liang, M. P. Shores, M. Bockrath, J. R. Long, and H. Park. Kondo resonance in a single-molecule transistor. *Nature*, 417, 2002.

[139] L. H. Yu and D. Natelson. The Kondo effect in C_60 single-molecule transistors. *Nano Lett.*, 4:79, 2004.

[140] M. Tsutsui, K. Shoji, M. Taniguchi, and T. Kawai. Formation and self-breaking mechanism of stable atom-sized junctions. *Nano lett.*, 8:345, 2008.

[141] T. Li, W. Hu, and D. Zhu. Nanogap electrodes. *Adv. Mater.*, 22:286, 2010.

[142] H. J. Mamin, P. H. Guethner, and D. Rugar. Atomic emission from a gold scanning-tunneling-microscope tip. *Phys. Rev. Lett.*, 65:2418, 1990.

[143] T. M. Mayer, J. E. Houston, G. E. Franklin, A. A. Erchak, and T. A. Michalske. Electric field induced surface modification of Au. *J. Appl. Phys.*, 85:8170, 1999.

[144] J. Schneir, R. Sonnenfeld, O. Marti, P. K. Hansma, J. E. Demuth, and R. J. Hamers. Tunneling microscopy, lithography, and surface diffusion on an easily prepared, atomically flat gold surface. *J. Appl. Phys.*, 63:717, 1988.

[145] H. J. Mamin, S. Chiang, H. Birk, P. H. Guethner, and D. Rugar. Gold deposition from a scanning tunneling microscope tip. *Appl. Phys. Lett.*, 9:1398, 1991.

[146] C. Xiang, J. Y. Kim, and R. M. Penner. Reconnectable sub-5 nm nanogaps in ultralong gold nanowires. *Nano Lett.*, 9:2133, 2009.

[147] A. Anaya, A. L. Korotkov, M. Bowman, J. Waddell, and D. Davidovic. Nanometer-scale metallic grains connected with atomic-scale conductors. *J. Appl. Phys.*, 93:3501, 2003.

[148] T. Kudo and K. Fueki. *Solid State Ionics*. VCH Publishers, 1990.

[149] K. Terabe, T. Nakayama, T. Hasegawa, and M. Aono. Formation and disappearance of a nanoscale silver cluster realized by solid electrochemical reaction. *J. Appl. Phys.*, 91:10110, 2002.

[150] K. Terabe, T. Hasegawa, T. Nakayama, and M. Aono. Quantized conductance atomic switch. *Nature*, 433:47, 2005.

[151] K. Terabe, T. Hasegawa, C. Liang, and M. Aono. Control of local ion transport to create unique functional nanodevices based on ionic conductors. *Sci. Tech. Adv. Mater.*, 8:536, 2007.

[152] T. E. Hartman. Electrical conduction in discontinuous thin metal films. *J. Appl. Phys.*, 34:943, 1963.

[153] J. E. Morris. Recent developments in discontinuous metal thin film devices. *Vacuum*, 50:107, 1998.

[154] P. Borziak, V. Dyukov, A. Kostenko, Yu. Kulyupin, and S. Nepijko. Electrical conductivity in structurally inhomogeneous discontinuous metal films. *Thin Solid Films*, 36:21, 1976.

[155] A. Kiesow, J. E. Morris, C. Radehaus, and A. Heilmann. Switching behavior of plasma polymer films containing silver nanoparticles. *J. Appl. Phys.*, 94:6988, 2003.

[156] M. Schulze, S. Gourley, S. A. Brown, A. Dunbar, J. Partridge, and R. J. Blaikie. Electrical measurements of nanoscale bismuth cluster films. *Eur. Phys. J. D*, 24:291, 2003.

[157] D. Corbett, M. Warner, S. Gourley, and S. Brown. Electromechanical conditioning and relaxation in nano wires,. *To be published*.

[158] T. F. Watson, D. Belić, P. Y. Convers, E. J. Boyd, and S. A. Brown. The morphology of tin cluster assembled films and the effect of nitrogen. *Eur. Phys. J. D*, 61:81, 2011.

[159] T. F. Watson. Tin oxide cluster assembled films: Morphology and gas sensors. Master's thesis, University of Canterbury, 2009.

[160] D. Belić. *Experimental studies of alloy nanocluster*. PhD thesis, University of Canterbury, 2011.

[161] E. H. Sondheimer. The mean free path of electrons in metals. *Adv. Phys.*, 1:1, 1952.

[162] Roland S. Timsit. Electrical contact resistance: Properties of stationary interfaces. *IEEE Trans. Compon. Packag. Technol.*, 22:85, 1999.

[163] A. F. Mayadas and M. Shatzkes. Electrical-resistivity model for polycrystalline films: the case of arbitrary reflection at external surfaces. *Phys. Rev. B*, 1:1382, 1970.

[164] S. Karim, M. E. Toimil-Molares, A. G. Balogh, W. Ensinger, T. W. Cornelius, E. U. Khan, and R. Neumann. Morphological evolution of au nanowires controlled by rayleigh instability. *Nanotechnology*, 17:5954, 2006.

[165] K. F. Gurski, G. B. McFadden, and M. J. Miksis. The effect of contact lines on the rayleigh instability with anisotropic surface energy. *SIAM J. Appl. Math.*, 66:1163, 2006.

[166] T. T. Tsong. Effects of an electric field in atomic manipulations. *Phys. Rev. B*, 44:13703, 1991.

[167] T. Sakamoto, H. Sunamura, H. Kawaura, T. Hasegawa, T. Nakayama, and M. Aono. Nanometer-scale switches using copper sulfide. *Appl. Phys. Lett.*, 82:3032, 2003.

[168] J. J. Yang, F. Miao, M. D. Pickett, D. A. A. Ohlberg, D. R. Stewart, C. N. Lau, and R. S. Williams. The mechanism of electroforming of metal oxide memristive switches. *Nanotechnology*, 20:215201, 2009.

[169] F. Hernandez-Ramirez, J. D. Prades, A. Tarancon, S. Barth, O. Casals, et al. Insight into the role of oxygen diffusion in the sensing mechanisms of SnO_2 nanowires. *Adv. Funct. Mater.*, 18:2990, 2008.

[170] C. Kittel. *Introduction to Solid State Physics*. Weiley, 7th edition, 1996.

[171] Ishii T. Hashimoto T. Kobayashi T. Murai F. Yano, K. and K. Seki. Room-temperature single-electron memory. *IEEE Trans. Electron Devices*, 41(9):1628, 1994.

[172] L. Guo, E. Leobandung, and Y. Chou, S. A room-temperature silicon single-electron metal-oxide-semiconductor memory with nanoscale floating-gate and ultranarrow channel. *Appl. Phys. Lett.*, 70:850, 1997.

[173] L. Guo, E. Leobandung, and S.Y. Chou. A silicon single-electron transistor memory operating at room temperature. *Science*, 275(5300):649, 1997.

[174] K.K. Likharev. Single-electron devices and their applications. *Proceedings of the IEEE*, 87(4):606, 1999.

[175] B.J. Gross. *1/f noise in MOSFETs with ultrathin gate dielectrics*. PhD thesis, Massachusetts Institute of Technology, 1992.

[176] J. M. Ziman. *Electron and Phonons*. Oxford, 2001.

[177] E. H. Sondheimer. The mean free path of electrons in metals. *Adv. Phys.*, 50:499, 2001.

[178] G. Reiss, J. Vancea, and H. Hoffmann. Grain-boundary resistance in polycrystalline metals. *Phys. Rev. Lett.*, 56:2100, 1986.

[179] N. W. Ashcroft and N. D. Mermin. *Solid State Physics*. Brooks, 1976.

[180] H. Ibach and H. Lüth. *Solid State Phys.* Springer, New York, 2010.

[181] M. Jayalakshmi and K. Balasubramanian. Hydrothermal synthesis of CuO-SnO_2 and CuO-SnO_2-Fe_2O_3 mixed oxides and their electrochemical characterization in neutral electrolyte. *Int. J. Electrochem. Sci.*, 4:571, 2009.

[182] C. G. Fonstad and R. H. Rediker. Electrical properties of high-quality stannic oxide crystals. *J. Appl. Phys.*, 42:2911, 1971.

[183] K. Nakahigashi and K. Higashimine. The electron density distribution in α-tin from powder X-Ray data by the maximum-entropy method. *J. Phys.: Condens. Matter*, 7:6961, 1995.

[184] B. D. Craig and D. S. Anderson. *Handbook of Corrosion Data*. ASM International, 2002.

[185] B. H. Hong, L. Choi, Y. C. Jung, and S. W. Hwang. Temperature dependent study of random telegraph noise in gate-all-around pMOS silicon nanowire field-effect transistors. *IEEE Trans. Nanotechnol.*, 9:754, 2010.

[186] Y. Yin, R.M. Rioux, C.K. Erdonmez, S. Hughes, G.A. Somorjai, and A.P. Alivisatos. Formation of hollow nanocrystals through the nanoscale kirkendall effect. *Science*, 304:711, 2004.

[187] C.M. Wang, D.R. Baer, L.E. Thomas, J.E. Amonette, J. Antony, Y. Qiang, and G. Duscher. Void formation during early stages of passivation: Initial oxidation of iron nanoparticles at room temperature. *J. Appl. Phys.*, 98:094308, 2005.

[188] R. Nakamura, D. Tokozakura, H. Nakajima, J.G. Lee, and H. Mori. Hollow oxide formation by oxidation of Al and Cu nanoparticles. *J. Aappl. Phys.*, 101:074303, 2007.

[189] P. I. Gaiduk, J. L. Hansen, and A. N. Larsen. Synthesis and analysis of hollow SnO nanoislands. *Appl. Phys. Lett.*, 92:193112, 2008.

[190] P.J. Fensham. Self-diffusion in tin crystals. *Aust. J. Chem.*, 3:91, 1950.

[191] N.Q. Lam, S.J. Rothman, H. Mehrer, and L.J. Nowicki. Self-diffusion in silver at low temperatures. *Phys. Status Solidi b*, 57:225, 1973.

[192] D. R. Strachan, D. E. Smith, D. E. Johnston, and T. H. Park. Controlled fabrication of nanogaps in ambient environment for molecular electronics. *Appl. Phys. Lett.*, 86:2950, 2005.

[193] T. Hayashi and T. Fujisawa. Voltage-pulse-induced electromigration. *Nanotechnology*, 19:145709, 2008.

Acknowledgement

First of all, I would like to thank Prof. Simon Brown for all his guidance and mentorship during the past four years. I appreciate from deepest of my heart all his support, which made it possible to focus my efforts to complete my PhD research. I am also extremely thankful to my co-supervisor Dr. Pierre Convers who helped me in the first year of my PhD to kick start my work here at Canterbury.

Many thanks to my group mates who have been involved with me in discussions and emotional support. I would like to mention Dr. David McCarthy, Dr. David Mackenzie, Dr. Domagoj Belic, Danial, Ojas Mahapatra, Dr. Pawel Kowalczyk, Amol Nande, Dr. Nadia Grillet, Dr. Shawn Fostner, Dr. Euan Boyd, Emily Delberg and Jack Grigg. I would like to thank Assoc. Prof Michael Reid for try to make environment a bit friendly during the oral exam. Furthermore, my friends have their part in this thesis as they were always been motivating and encouraging me to achieve my goals.

Nothing was possible without the help of workshop technicians and office staff. Graeme Kershaw, Stephen Hemmingsen and especially Bob Flygenring were a great help. Thanks to Orlon Petterson for providing IT support. Office staff Xuefeng Liu, Rosalie Reilly, Rhondda Sullivan and Marney Ainsworth have also been kind and helpful. I would like to thank Mohammad Zeidan for all his help. I would also like to thank the staff at NanoFab lab Helen Dervax and Gary Turner for their support.

Last but not the least, I am thankful to my mother, father, brothers, sister and my wife. Although they were 8,000 miles away still their emotional support was essential in achieving my goals.